Fully microscopic analysis of laser-driven finite plasmas

Dissertation zur Erlangung des akademischen Grades
doctor rerum naturalium
der Mathematisch-Naturwissenschaftlichen Fakultät
der Universität Rostock

vorgelegt von

Christian Peltz

aus Teterow

Rostock, 2015

urn:nbn:de:gbv:28-diss2016-0020-7

Gutachter: Prof. Dr. Th. Fennel (Universität Rostock)
Prof. Dr. Mikhail Ivanov (Max Born Institut Berlin)

Datum der Einreichung: 24. April 2015
Datum der Verteidigung: 02. Oktober 2015

List of own publications

[1] C. Peltz and T. Fennel. Resonant charging of Xe clusters in helium nanodroplets under intense laser fields. *Eur. Phys. J. D*, **63**:281–288, 2011.

[2] Sergey Zherebtsov, Thomas Fennel, Juergen Plenge, Egill Antonsson, Irina Znakovskaya, Adrian Wirth, Oliver Herrwerth, Frederik Suessmann, Christian Peltz, Izhar Ahmad, Sergei A. Trushin, Vladimir Pervak, Stefan Karsch, Marc J. J. Vrakking, Burkhard Langer, Christina Graf, Mark I. Stockman, Ferenc Krausz, Eckart Ruehl, and Matthias F. Kling. Controlled near-field enhanced electron acceleration from dielectric nanospheres with intense few-cycle laser fields. *Nat. Phys.*, **7**:656–662, 2011.

[3] S. Zherebtsov, F. Suessmann, C. Peltz, J. Plenge, K. J. Betsch, I. Znakovskaya, A. S. Alnaser, N. G. Johnson, M. Kuebel, A. Horn, V. Mondes, C. Graf, S. A. Trushin, A. Azzeer, M. J. J. Vrakking, G. G. Paulus, F. Krausz, E. Ruehl, T. Fennel, and M. F. Kling. Carrier-envelope phase-tagged imaging of the controlled electron acceleration from SiO2 nanospheres in intense few-cycle laser fields. *New J. Phys.*, 14:075010, 2012.

[4] Charles Varin, Christian Peltz, Thomas Brabec, and Thomas Fennel. Attosecond Plasma Wave Dynamics in Laser-Driven Cluster Nanoplasmas. *Phys. Rev. Lett.*, **108**:175007, 2012.

[5] S. R. Krishnan, Ch Peltz, L. Fechner, V. Sharma, M. Kremer, B. Fischer, N. Camus, T. Pfeifer, J. Jha, M. Krishnamurthy, C-D Schroeter, J. Ullrich, F. Stienkemeier, R. Moshammer, Th Fennel, and M. Mudrich. Evolution of dopant-induced helium nanoplasmas. *New J. Phys.*, **14**:075016, 2012.

[6] Christian Peltz, Charles Varin, Thomas Brabec, and Thomas Fennel. Fully microscopic analysis of laser-driven finite plasmas using the example of clusters. *New J. Phys.*, **14**:065011, 2012.

[7] Mathias Arbeiter, Christian Peltz, and Thomas Fennel. Electron-relocalization dynamics in xenon clusters in intense soft-x-ray fields. *Phys. Rev. A*, **89**:043428, 2014.

[8] Christian Peltz, Charles Varin, Thomas Brabec, and Thomas Fennel. Time-Resolved X-Ray Imaging of Anisotropic Nanoplasma Expansion. *Phys. Rev. Lett.*, **113**:133401, 2014.

[9] Charles Varin, Christian Peltz, Thomas Brabec, and Thomas Fennel. Light wave driven electron dynamics in clusters. *Ann. Phys.-Berlin*, **526**:135–156, 2014.

[10] Ingo Barke, Hannes Hartmann, Daniela Rupp, Leonie Flückiger, Mario Sauppe, Marcus Adolph, Sebastian Schorb, Christoph Bostedt, Rolf Treusch, Christian Peltz, Stephan Bartling, Thomas Fennel, Karl-Heinz Meiwes-Broer, and Möller Thomas. The 3D-architecture of individual free silver nanoparticles captured by X-ray scattering. *Nat. Commun.*, **6**:6187, 2015.

[11] Egill Antonsson, Christian Peltz, Jürgen Plenge, Burkhard Langer, Thomas Fennel, and Eckart Rühl. Signatures of Transient Resonance Heating in Photoemission from Free NaCl Nanoparticles in Intense Femtosecond Laser Pulses. *J. Electron. Spectrosc. Relat. Phenom.*, 2015, accepted.

[12] F. Suessmann, L. Seiffert, S. Zherebtsov, V. Mondes, J. Stierle, M. Arbeiter, J. Plenge, P. Rupp, C. Peltz, A. Kessel, S. A. Trushin, B. Ahn, D. Kim, C. Graf, E. Rhl, M. F. Kling, and T. Fennel. Field propagation induced directionality of carrier-envelope phase controlled photo-emission from nanospheres. *Nat. Commun.*, 2015, submitted.

List of presentations

Talks:

03.2009 DPG Spring Meeting (Sektion AMOP), Hamburg
„*Ionization dynamics of embedded Xenon clusters in strong laser fields*"

03.2010 DPG Spring Meeting (Sektion AMOP), Hannover
„*Ionization dynamics of NaCl-nanocrystals in strong laser fields*"

03.2011 DPG Spring Meeting (Sektion AMOP), Dresden
„*Resonant charging of Xe clusters in Helium nanodroplets under intense laser fields*"

09.2011 Clustertreffen, Würzburg
„*Resonant charging of Xe clusters in Helium nanodroplets under intense laser fields*"

03.2012 DPG Spring Meeting (Sektion AMOP), Stuttgart
„*Attosecond plasma wave dynamics in laser-driven cluster nanoplasmas*"

09.2012 Seminar, Ottawa (Canada)
„*Bridging the microscopic and macroscopic realms of laser-matter interaction*"

03.2013 DPG Spring Meeting (Sektion AMOP), Hannover
„*Clusters in intense femtosecond XUV pulses: Direct simulation of light scattering*"

03.2014 DPG Spring Meeting (Sektion AMOP), Berlin
„*Time-resolved x-ray imaging of laser-driven hydrogen nanoclusters: a microscopic particle-in-cell analysis*"

Posters:

05.2009 6^{th} Workshop on Quantum Fluid Clusters, Dresden
„*Ionization dynamics of embedded Xenon clusters in strong laser fields*"

10.2009 Clustertreffen, Herzogenhorn
„*Ionization dynamics of embedded Xenon clusters in strong laser fields*"

09.2011 2^{nd} International Conference on Correlation Effects in Radiations Fields (CERF) , Rostock
„*Resonant charging of Xe clusters in Helium nanodroplets under intense laser fields*"

09.2012 2^{nd} International Conference on Correlation Effects in Radiations Fields (CERF) , Rostock
„*Resonant charging of Xe clusters in Helium nanodroplets under intense laser fields*"

10.2014 Clustertreffen, Herzogenhorn
„*Time-Resolved Imaging of Cluster Expansion*"

11.2014 14^{th} International Workshop on Atomic Physics , Dresden
„*Time-Resolved X-Ray Imaging of Anisotropic Nanoplasma Expansion*"

03.2015 DPG Spring Meeting (Sektion AMOP), Heidelberg
„*Time-Resolved X-Ray Imaging of Anisotropic Nanoplasma Expansion*"

Contents

List of own publications I

List of presentations III

1. Introduction 1

2. Microscopic Particle-In-Cell Approach 9
2.1. Basic concept . . . 9
2.2. Numerical aspects of MicPIC . . . 13
2.2.1. Electromagnetic field propagation with the Finite-difference time-domain method . . . 13
2.2.2. Particle representation on the PIC-level . . . 23
2.2.3. Local Correction . . . 26
2.2.4. Particle propagation . . . 28
2.2.5. Implementation of ionization . . . 29
2.2.6. MicPIC parameters and scaling . . . 31
2.2.7. MicPIC system energy calculation . . . 33

3. Validating MicPIC 35
3.1. Nanoplasma formation in small rare-gas clusters . . . 36
3.2. Linear-response dynamics for small and large clusters . . . 38
3.2.1. Cluster dynamics in the linear response regime . . . 38
3.2.2. Radius-dependent absorption and scattering: comparison with continuum models . . . 40
3.3. Competition of bulk and surface collisional effects with radiation damping in resonant clusters . . . 44

4. Laser driven plasma wave dynamics 47
4.1. Generation and evolution of plasma waves . . . 48
4.2. Ionization in the vicinity of plasma waves . . . 50
4.3. Plasma waves in solid density matter . . . 52

5. Clusters exposed to intense short-wavelength radiation 57
5.1. The x-ray scattering simulation setup . . . 57
5.2. Time-resolved x-ray imaging of anisotropic nanoplasma expansion . . . 60
5.3. A dissipative oscillator model to describe atomic polarization and photoionization . . . 65
5.3.1. The harmonic oscillator model . . . 66
5.3.2. Adapting the harmonic oscillator model to hydrogen . . . 67

5.3.3. Photoionization 68
5.4. Inelastic x-ray scattering 70

6. The origin of highly charged atomic ions from x-ray laser-cluster interactions 73
6.1. Modeling the interaction of hard x-ray radiation with clusters via Molecular Dynamics simulations 76
6.2. Cluster excitation and expansion dynamics induced by intense x-ray excitation 78
6.3. Effect of a DC-extraction fields for ion detection on the re-localization dynamics 83
6.4. X-ray intensity dependence of the final charge state distribution 87

7. Conclusions and outlook 89

Appendix 94

A. Time dependence of expansion driven electron cooling in weakly and strongly coupled plasmas 94
A.1. Weakly coupled plasmas 94
A.2. Strongly coupled plasmas 94

B. Interactionpotential for two gaussian charge distributions 96
B.1. Gaussian charge distribution 96
B.2. Interaction energy of Gaussian charge distribution and a point charge . 97
B.3. Interaction energy of two Gaussian particles 98

Bibliography 101

Erklärung 111

List of Figures

1.1. Laser-cluster interaction stages 4
1.2. Resonant plasmon excitation in small Argon clusters 5
1.3. Single shot single cluster experiments at Flash 6

2.1. Yee staggering 16
2.2. Charge sampling error analysis 24
2.3. Inter-particle forces on the PIC level 25
2.4. MicPIC force decomposition 26
2.5. Sketch of the cell indexing procedure 27
2.6. Local correction scheme 33

3.1. Nanoplasma creation in small Argon clusters 37
3.2. Cluster dynamics in the linear response regime 39
3.3. Absorption and scattering efficiencies 43
3.4. Plasmon lifetime analysis 45

4.1. Snapshots of plasma wave dynamics in resonantly excited hydrogen-like cluster 49
4.2. Time evolution of charge density and electric field spatial distribution in hydrogen-like resonantly excited cluster 50
4.3. Snapshots of plasma wave dynamics in a resonantly excited Xenon cluster 51
4.4. Nonuniform ionization in a resonantly excited Xenon cluster 52
4.5. Snapshots of plasma wave dynamics in a Xenon cluster at solid density 53
4.6. Plasma wave dynamics in a Xenon cluster at solid density 54
4.7. Final charge state distributions in a Xenon cluster at solid density . . . 55

5.1. Sketch of the x-ray imaging simulation setup 58
5.2. Comparison of elastic scattering from MicPIC and Mie theory 59
5.3. Time resolved x-ray imaging scattering pattern 61
5.4. Direction resolved density profiles during cluster expansion 62
5.5. Time evolution of density profile parameters 63
5.6. Selective parameter analysis with Born method 64
5.7. Reconstruction of the anisotropic expansion dynamics 65
5.8. Absorption and scattering cross sections for hydrogen 68
5.9. Time evolution of photoionization 69
5.10. Scattered x-ray intensity spectrum for NIR pump/ x-ray probe excitation 71
5.11. Scattered x-ray intensity spectrum for x-ray only excitation with ionization 71

6.1. Schematics of the x-ray cluster interaction dynamics 74

6.2. Experimental single shot ion spectra 75
6.3. Photoionization cross sections for Argon 77
6.4. Hard x-ray excitation of a Xenon cluster 79
6.5. Time evolution of inner and outer ionization 80
6.6. Nanoplasma dynamics in terms of single-particle energy spectra 81
6.7. Time evolution of the electron temperature 82
6.8. Single-particle-energy distributions 83
6.9. Effect of an DC extraction field on the outer ionzation 84
6.10. Ion charge spectra with and without extraction field 85
6.11. Electron transverse kinetic energy spectrum 86
6.12. Intensity dependence of x-ray cluster ionization 88

List of Tables

2.1. Main simulation parameters 32

1. Introduction

The year 2015 has been proclaimed as the "International Year of Light and Light-based Technologies" by the United Nations, highlighting the importance of light and light matter interaction for all areas of life. A key motivation for choosing this specific year is the 150th anniversary of the publication of the famous Maxwell's equations [1]. This set of equations describes the propagation of light through matter and predicts the evolution of electric and magnetic fields based on the distribution and dynamics of charged particles, in principle down to the atomic scale. The consideration of each individual atom is, however, usually not practicable. Instead, if the relevant scales of the light field are much larger than the interatomic distances[1], continuum descriptions are applied where the microscopic light-matter interaction is approximated via material parameters, e.g. the index of refraction. This approach is justified for relatively weak excitations where the system is not significantly modified by the incoming light and the materials response is essentially linear. To some extent, even nonlinear effects like the self-focusing due to the optical Kerr effect can be included using nonlinear material parameters. However, at high intensity, the materials and their optical properties are often strongly altered by ultrafast excitation, ionization and heating, precluding a meaningful continuum description based on material parameters, at least in general. In particular, current and future experiments with femtosecond and attosecond laser pulses require the self-consistent and explicit description of these processes.

A widely used numerical method to study light-matter interaction in the high intensity regime is the electromagnetic particle-in-cell (PIC) approach [2–4]. Here Maxwell's equations are solved on a grid along with the relativistic equations of motion for all PIC particles. Typically, these PIC particles represent an average over many physical particles and are sampled on a coarse grid. As a result of this averaging all microscopic processes are lost and only the collective response is explicitly described. This, however, is only justified for very high intensities (in or close to the relativistic regime) and for dilute systems where collisions can be neglected. These collisionless PIC codes have revolutionized our understanding of relativistic laser-plasma interactions [5–7]. To take microscopic interactions into account at least on an effective level, collisional PIC codes reintroduce binary collisions of plasma particles via Monte-Carlo methods [8, 9] which is valid in the regime of weak coupling, where microfield fluctuations are negligible and microscopic interactions are restricted to small-angle binary collisions [10–13]. However, a broad spectrum of experiments and applications takes place in the realm of intense but non-relativistic light-matter interaction, ranging from industry driven applications like laser micro-machining [14] and laser modification of

[1] Properties like the wavelength of the incident light or the corresponding skin-depth of the material define the relevant scales.

metals and dielectric materials [15,16] to the development of devices based on ultrafast strongfield nanoplasmonics [17–20]. In particular for intensities close to the ionization threshold, the underlying dynamics proceeds far from equilibrium and is strongly coupled [21, 22]. Here even collisional PIC misses important effects: (i) scattering rates can not be defined unambiguously as conventional screening theories are not applicable; (ii) many-particle recombinations via three and more body collisions become important; (iii) plasma microfields enhance field and impact ionization [23, 24]; and (iv) the PIC particle size exceeds the surface length scale, prohibiting a quantitative description of surface phenomena.

To model non-degenerate[2] strongly coupled plasmas, the classical trajectories of all electrons and ions have to be propagated explicitly and microscopic processes such as collisions have to be fully resolved. For small systems, where the dipole approximation is justified and field propagation effects can be neglected, this can be done efficiently with electrostatic molecular dynamics (MD) calculations [25, 26]. However, to describe macroscopic plasma volumes an electromagnetic treatment is required that fully accounts for field propagation effects. In order to achieve that on the basis of standard PIC methods, PIC particle sizes and grid spacings on the order of 1 Å would be required. As the numerical effort for the solution of Maxwell's equations scales as ($\approx 1/\Delta x^4$) such a treatment is out of reach for macroscopic plasma volumes.

In the framework of this thesis a novel numerical code is developed for this task. It is based on an idea proposed by Thomas Fennel from the University of Rostock and Thomas Brabec from the University of Ottawa (Canada). The so-called Microscopic Particle-In-Cell (MicPIC) method is supposed to overcome the above limitations by connecting MD and PIC in a two-level approach. In MicPIC, long-range electromagnetic interactions are treated on a coarse numerical grid (PIC level). To also fully resolve microscopic processes, the short range interactions missing in the PIC part are reintroduced via local electrostatic MD. The main goal of this work is the numerical implementation of the Microscopic Particle-In-Cell approach, its validation, and its application to so far theoretically inaccessible physical scenarios. For the first applications presented in this work clusters have been used as model systems. Clusters range from the size of small molecules to that of small droplets of condensed matter. This scalability makes a them a valuable testing ground for the exploration of new many-particle physics. In the following, key aspects of laser-cluster interactions relevant for the understanding of this thesis are discussed and put into relation with selected experiments.

Selected key aspects of laser-cluster interaction

Subject to high intensity optical laser fields, clusters are quickly turned into localized, highly ionized finite plasmas and expand on a femtosecond to picosecond time scale [25, 26]. In the past decades, a multitude of experiments has been performed in this regime

[2] For thermal energies smaller or equal to the Fermi energy (degeneracy parameter $\Theta = k_B T/E_F \lesssim 1$) quantum effects (e.g. Pauli-blocking) become important and a classical description is not justified; the plasma is then called degenerate.

and revealed a large variety of features, e.g. the emission of high energy electrons [27–30] , highly charged energetic ions [31–33] and high energy radiation [34–37]. Many of these findings are directly or indirectly connected to the Mie plasmon, the collective dipole motion of the electron plasma. To estimate the conditions for resonant coupling of the laser to the plasma electrons, the system can be approximated as an ideal, homogenous, perfectly conducting sphere, which yields the Mie plasmon resonance frequency

$$\omega_{\mathrm{Mie}} = \sqrt{\frac{e^2 n_{\mathrm{i}} \langle Z \rangle}{3\varepsilon_0 m_{\mathrm{e}}}}, \tag{1.1}$$

where m_{e} is the electron mass, n_{i} is the ion number density and $\langle Z \rangle$ is the average ion charge state. In case of charge neutrality, the density of ionic background charges is equal to the number density of conduction electrons. While delocalized conduction electrons already exist in the ground state for metallic clusters, they have to be generated first in dielectric and rare gas systems. This plasma generation is typically the first step of the laser-cluster interaction dynamics as schematically shown in figure 1.1 for the example of dual pulse excitation. For laser wavelengths in the visible or near-visible frequency regime, plasma generation is typically triggered by tunnel ionization and followed by electron impact ionization avalanching. The removal of electrons from their host atom or ion is termed inner ionization. Due to the emerging space charge potential of the residual positively charged cluster, only a fraction of these electrons can escape (outer ionization) while most of the activated electrons remain bound to the cluster potential. Electrons that can move freely inside the system but not leave the cluster are referred to as quasi-free electrons, c.f. figure 1.1a.

In this first stage, the system is still at or close to solid density and the corresponding Mie resonance frequency is typically higher than the laser frequency. However, due to Coulomb repulsion of the ions and/or hydrodynamic forces the excited cluster begins to expand, resulting in an continuous lowering of the ionic background density (see figure 1.1b). Eventually, the cluster will reach the critical density that enables resonant laser-plasmon coupling. In this case, the resonant collective excitation leads to strongly enhanced energy absorption, producing energetic electrons and ions observed in experiments. This resonant coupling has been mainly studied by utilizing two different excitation scenarios. First experiments used single pulses with a variable pulse length but constant pulse energy. Optimal coupling is observed for pulses that are just long enough to reach critical density while the pulse is still on, such that the plasmon resonance is driven by the same pulse that created the nanoplasma [29,38,39]. A more flexible scheme to study the plasmon resonance is provided by dual pulse experiments [30, 40], as shown in figure 1.1, which allows one to analyze the intensity dependence of the expansion induced by the first pulse and the coupling efficiency of the second pulse separately. Subsequently, the cluster continues to expand and disintegrates into single atoms/ions irrespective of the nature of the initial ionization process and possible resonant coupling in stage (c). Note that the illustration given in figure 1.1 describes the general interaction dynamics of clusters with intense laser fields.

The trivial consequence of resonant plasmon excitation in clusters is a pronounced collective electron motion that leads to high absorption. The fact that this motion

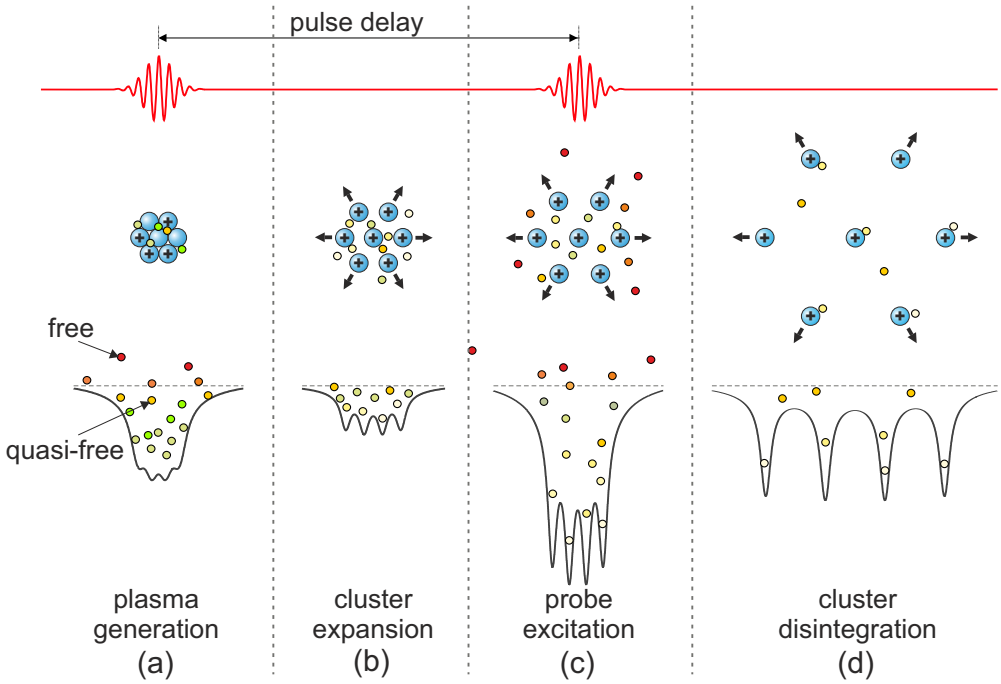

Figure 1.1.: Schematic illustration of the typical ionization and expansion dynamics of a rare gas cluster for a dual pulse excitation scheme. The dynamics can be divided into 4 main stages: (a) Plasma generation via atomic ionization. (b) Cluster expansion due to Coulomb repulsion of the ions and/or hydrodynamic forces. (c) Probing of the system state with a second pulse. (d) Disintegration of the cluster.

can result in nontrivial secondary effects is illustrated here on the basis of a dual pulse experiment [24], where enhanced electron emission along the laser polarization direction has been observed for resonant plasmon excitation in medium-sized silver clusters. Figure 1.2b shows the measured delay dependent electron yield, parallel ($E_{\parallel}$) and perpendicular ($E_{\perp}$) to the polarization axis, for different energy intervals. The data reveal a strongly increasing asymmetry with increasing electron energy, c.f. bottom to top panels in figure1.2b. The energy resolved electron spectra shown in figure 1.2c for single pulse- and resonant dual pulse excitaton further show that the observed asymmetry can be clearly attributed to the resonant plasmon excitation.

Semiclassical simulations revealed the following picture of the underlying electron acceleration mechanism: The laser driven collective electron oscillation generates a time dependent polarization potential that changes sign every laser half-cycle. The shape and temporal evolution of the potential is sketched in figure 1.2d. Part of the plasma electrons do not follow the collective motion and are instead located on the opposite side of the cluster. For specific initial conditions (position and momentum), these electrons can traverse the cluster, such that they are permanently accelerated by the evolving polarization potential. This highly selective acceleration mechanism, referred to as surface-plasmon-assisted rescattering in clusters (SPARC), leads to the ejection of energetic electron bursts along the laser polarization axis in every laser half cycle and is strongest for resonant plasmon excitation.

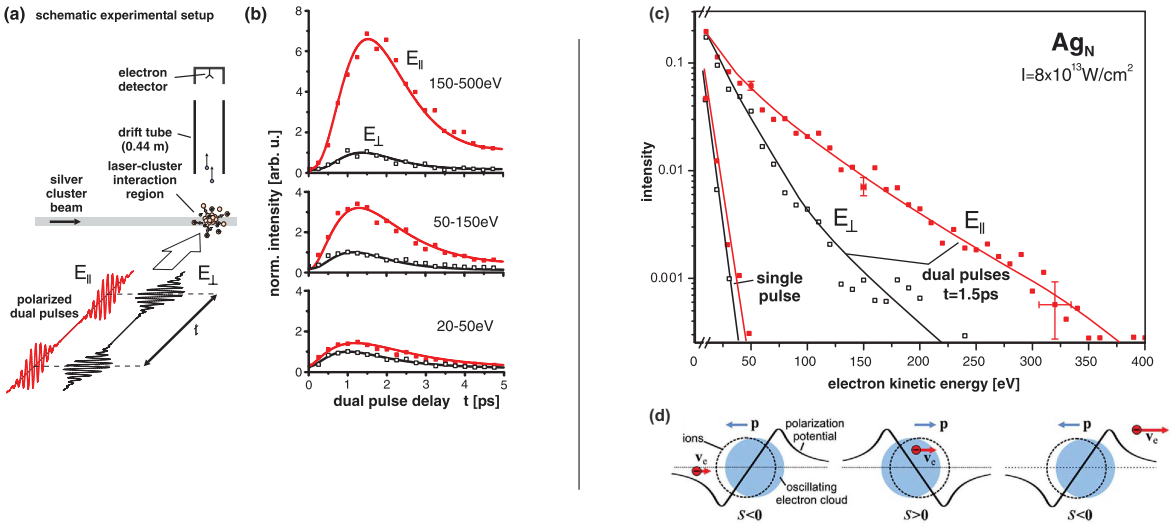

Figure 1.2.: (a) Schematic experimental setup. (b) Photoelectron spectra from Ag_N clusters (N=500-2000) upon excitation with dual 100 fs laser pulses at 8×10^{13} W/cm^2 for parallel ($E_{\parallel}$) and perpendicular ($E_{\perp}$) laser polarization for three different energy intervals (as indicated). (c) Angular resolved photoelectron spectra for single vs. resonant dual pulse excitation. (d) Schematics of the surface-plasmon-assisted rescattering in clusters (SPARC) process. From reference [24]

Key to the interpretation of the experiment described above and many others is the ability to model the laser-cluster interaction microscopically. So far, these kind of studies have been limited to small systems where the dipole approximation and the neglect of field propagation effects are justified. Corresponding calculations for large clusters with diameters on the order of the wavelength have just become possible with the development of MicPIC and are part of this thesis. The main open questions that will be addressed here concern (i) the potential influence of propagation effects like field retardation and radiation damping on the plasmon excitation dynamics and (ii) possible secondary effects on the plasma dynamics on a microscopic level.

A completely different application area for clusters emerges from the rapid development of new generation light sources, i.e. free-electron-lasers (FELs). Today, these facilities are able to generate pulses of coherent radiation with an extremely high number of photons with frequencies up to the hard x-ray regime [41, 42]. One key application of FELs is single-shot coherent diffractive imaging as it allows to analyze the structure of single nanoobjects [43] and biomolecules [44]. In combination with the short FEL pulse duration of only a few femtoseconds, even time- and space-resolved x-ray imaging seems to be feasible, with the ultimate goal of visualizing ultrafast dynamics in matter with atomic-scale resolution. However, the three dimensional reconstruction of complex structures from the scattering data remains a complex task. As only intensities can be recorded on the detectors, the phase of the scattered fields are missing. Further complications can arise from transient changes of the target or additional dynamics introduced by the probing x-ray pulse itself [45].

Due to their often relatively simple electronic and geometric structure atomic clusters

are the ideal model system to approach this emerging field[3]. In first proof-of-principle experiments with large Xenon clusters, the cluster size [47] and shape [48] have been measured, demonstrating the experimental feasibility of time-resolved x-ray imaging. The capabilities of such state-of-the-art experiments are now illustrated on the basis of an experiment performed by Bostedt *et al.* [49] at the FLASH free-electron-laser in Hamburg. In the experiment, a low density cluster beam has been crossed with the incoming FEL beam, such that only single clusters are hit by the x-ray pulses. The resulting scattering pattern are then recorded with an x-ray sensitive detector on a shot-to-shot basis, see figure 1.3. The scattering images carry information on the respective cluster size/shape and the x-ray intensity it has been exposed to. As Xenon mainly forms spherical droplets in this size regime, the cluster diameter can be directly calculated from the fringe spacing of the resulting Mie scattering pattern. Figure 1.3b-d shows full 2D scattering images and corresponding 1D cuts for 3 representative laser shots with clusters of similar size. The laser intensity can be estimated from the signal intensity on the screen. The brightest images correspond to shots where the cluster has been excited in the FEL focus. Given that the peak intensity of the x-ray pulse is known, the intensities for shots with similar cluster sizes but darker images can be estimated, c.f. boxes in figure 1.3b-d.

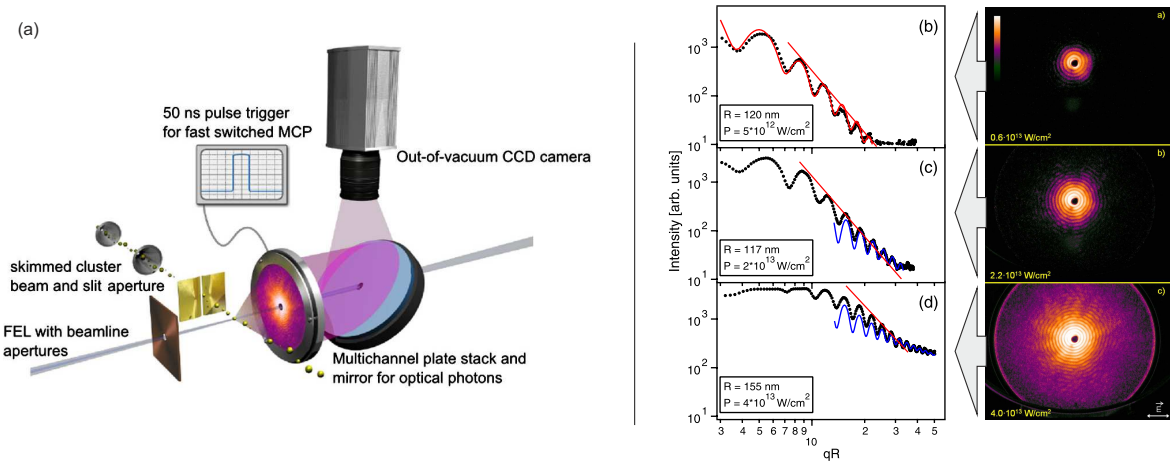

Figure 1.3.: (a) Experimental setup for single-shot nanoparticle imaging experiments at 90 eV photon energy. Nanoclusters are injected into the focused x-ray pulse (20 fs duration), and the scattered light is recorded with a high repetition rate detector. (b-d) Single-shot scattering profiles (dotted curves) for well defined cluster sizes and FEL intensities (as indicated) estimated from the corresponding full scattering patterns (to the right). From reference [49].

For spherical objects with homogeneous density and for given optical constants, the scattering pattern can be calculated exactly with Mie-theory. Vice versa, Mie-theory can be used to fit the measured scattering pattern and determine the optical constants. Doing this for the examples shown in figure 1.3b-d reveals that different optical parameters are necessary to describe the scattering at different laser intensities. As the cluster geometry does not change on the time scale of the pulse (20 fs), irrespective

[3]Recent imaging experiments by Barke *et al.* [46] revealed that large silver clusters can exhibit unexpected complex structures in the gas phase.

of the intensity, these variations have to be a result of transient electronic changes. Bostedt *et al.* interpreted this behavior in terms of enhanced absorption of a thin surface layer, induced by ionization.

The interpretation of the above experiment is solely based on the analysis of the elastically scattered light. Another important observable is provided by the inelastic contribution to the scattering. For example, coupling of the x-ray light to thermal density fluctuations results in Raman-type plasmon satellites in the scattering spectrum. In plasma x-ray Thomson scattering experiments these satellites provide a sensitive measure of the plasma electron density [50, 51].

The next logical step is to perform dynamic x-ray imaging experiments, where the imaging pulse is used to study the dynamics induced by a preceding pump pulse as a function of time. As this goes along with geometrical changes, Mie-theory will no longer be applicable and a more suitable theoretical model is needed for their interpretation. The fact that MicPIC is able to simultaneously and self-consistently describe the microscopic plasma dynamics and the evolution of the electromagnetic fields with high spatial resolution makes it the perfect tool for the theoretical description of such an experiment.

Structure of the thesis

In **chapter 2** the idea of MicPIC is discussed from a physical point of view and selected technical details of its numerical implementation are described. **Chapter 3** describes the validation of the approach by comparison to well established models. In **chapter 4** MicPIC is used to study the generation and evolution of nonlinear plasma waves for resonant and off-resonant cluster excitation. Special focus is put on the impact of plasma waves on the ionization dynamics. **Chapter 5** presents first MicPIC results for the interaction of soft x-ray radiation with large clusters. In these studies the elastic and inelastic contributions to the x-ray scattering are analyzed for single and dual pulse excitation with focus on the implications for corresponding experiments. **Chapter 6** provides a detailed molecular dynamics analysis of the formation of final ion charge states from intense laser-cluster interactions. A summary and critical discussion of the results is given in **chapter 7**.

2. Microscopic Particle-In-Cell Approach

This chapter contains a comprehensive description of the MicPIC method and is divided into two parts. The first section discusses the idea of MicPIC from a physical point of view. The second part focuses on technical details of its numerical implementation.

2.1. Basic concept

Physical problem

In a classical picture, the exact non-relativistic dynamics of a plasma particle in the presence of electromagnetic fields is determined by the Lorentz force

$$\mathbf{f}_i = \int \rho_i(\mathbf{r}) \left(\mathbf{E} + \dot{\mathbf{r}}_i \times \mathbf{B}\right) d^3r, \tag{2.1}$$

where $\rho_i(\mathbf{r})$ and $\dot{\mathbf{r}}_i$ are the charge density distribution and velocity of the i-th particle, and $\mathbf{E}$ and $\mathbf{B}$ are the microscopic electric and magnetic fields. Once these fields are known, the force on each particle can be calculated and the dynamics of the system follows from the self-consistent integration of the classical equations of motion. The self-consistent evolution of the corresponding classical electromagnetic fields is determined by Maxwell's curl equations according to

$$\nabla \times \mathbf{E} = -\dot{\mathbf{B}} \tag{2.2}$$

$$\nabla \times \mathbf{B} = \mu_0 \mathbf{j} + \mu_0 \varepsilon_0 \dot{\mathbf{E}}. \tag{2.3}$$

Here the charged particles couple to the electromagnetic fields via the current density $\mathbf{j} = \sum_i \dot{\mathbf{r}}_i \rho_i$. From a physical point of view, the classical plasma dynamics is completely specified by equations (2.1)-(2.3). However, the full numerical solution of this set of equations becomes very demanding for many particle systems. The reason for that is that the solution of the field equations on a grid scales with $1/\Delta x^4$, where Δx is the mesh size (grid resolution). In order to resolve microscopic processes properly, the mesh has to be of the order of one atomic unit or even less, such that the direct numerical solution becomes prohibitive in practice. The MicPIC approach offers a route to overcome this problem and is introduced in the following step by step.

Particle representation

In MicPIC, each plasma particle (electron or ion) is represented by a charge density distribution according to

$$\rho_i(\mathbf{r}) = q_i\, g(|\mathbf{r} - \mathbf{r}_i|, w_0), \tag{2.4}$$

where q_i is the charge and $\mathbf{r}_i$ is the position of the i-th particle and the shape function $g(r, w) = \exp(-r^2/w^2)/\pi^{3/2}w^3$ describes a normalized Gaussian distribution of width w.

The long range interaction between two of such particles is essentially determined by the particle charges, i.e. the monopole contributions of a multipole expansion. However, their short range interaction is strongly dependent on their exact shape and size. In general, larger particle widths yield smoother fields around their origin and therefore result in a softened short range interaction. These short range interactions primarily determine the collision dynamics of plasma particles. Therefore the width w_0 is a key parameter that should, within technical and physical limits (see Section 2.2.6), be chosen as small as possible[1]. On the other hand, the particle width also determines the spatial resolution that is necessary to sufficiently resolve the particle shape on a grid, i.e. a large particle width is key to an efficient solution of Maxwell's equations, as it allows the use of a coarse numerical grid and large time steps.

So far, there have been two major approaches to deal with these conflicting needs: (i) The regular particle-in-cell approach, which uses super-particles[2] with large particle widths to describe the collective plasma dynamics, but neglects particle collisions. The latter assumption is justified only in the relativistic regime at low density [52–54]. And (ii) the collisional particle-in-cell approach, which uses the same superparticles but reintroduces the underestimated collisions via Monte-Carlo methods using approximate binary collision rates [8, 10]. Both approaches have their merits and have revolutionized our understanding of strong field plasma physics. However, even the collisional particle-in-cell method is restricted to the regime of weak coupling, where microscopic fluctuations are negligible and microscopic interactions are limited to small angle binary collisions. MicPIC is intended to describe the nonrelativistic dynamics of laser-driven clusters and bulk materials, which proceeds far from equilibrium and is strongly coupled. Therefore the short range interactions have to be taken into account explicitly. Within MicPIC this is done in a consistent two level approach that combines the electromagnetic treatment of the collective plasma dynamics on a PIC level with a local electrostatic molecular dynamics to describe microscopic correlations (Mic).

Particle-in-cell approximation

On the PIC level, particles are represented by a particle width larger than the actual particle width ($w_{\mathrm{pic}} \gg w_0$), the corresponding smoothed particle charge density reads

$$\rho_i^{\mathrm{pic}}(\mathbf{r}) = q_i\, g(|\mathbf{r} - \mathbf{r}_i|, w_{\mathrm{pic}}). \tag{2.5}$$

[1] The Coulomb singularity at zero particle distance can only be observed when the width is reduced to point like particles.

[2] A super-particle represents multiple physical particles, up to millions of electrons or ions.

The super/subscripts "pic" indicate that the respective quantities belong to the particle-in-cell level. The corresponding PIC electric and magnetic field evolution is then given by

$$\nabla \times \mathbf{E}^{\mathrm{pic}} = -\dot{\mathbf{B}}^{\mathrm{pic}} \tag{2.6}$$

$$\nabla \times \mathbf{B}^{\mathrm{pic}} = \mu_0 \mathbf{j}^{\mathrm{pic}} + \mu_0 \varepsilon_0 \dot{\mathbf{E}}^{\mathrm{pic}} \tag{2.7}$$

with the smoothed current density $\mathbf{j}^{\mathrm{pic}} = \sum_i \dot{\mathbf{r}}_i \rho_i^{\mathrm{pic}}$. Note that in this description radiation fields are fully accounted for if w_{pic} is smaller than all relevant scales (wavelength, skin depth, etc.). However, the microscopic nature of the particles and therefore also all resulting correlation effects are lost due to the large PIC particle size. The PIC force on the i-th plasma particle is given by

$$\mathbf{f}_i^{\mathrm{pic}} = \int \rho_i^{\mathrm{pic}} (\mathbf{E}^{\mathrm{pic}} + \dot{\mathbf{r}}_i \times \mathbf{B}^{\mathrm{pic}}) d^3 r. \tag{2.8}$$

MicPIC force decomposition

To identify the missing short-range forces in the PIC-approximation, the actual force on plasma particle i can be formally split into a microscopic part $\mathbf{f}_i^{\mathrm{mic}}$ and a long range PIC part $\mathbf{f}_i^{\mathrm{pic}}$. This can be done by subtracting/adding the PIC forces from/to the full expression in (2.1) via

$$\begin{aligned} \mathbf{f}_i &= \underbrace{\int \left[\rho_i (\mathbf{E} + \dot{\mathbf{r}}_i \times \mathbf{B}) - \rho_i^{\mathrm{pic}} (\mathbf{E}^{\mathrm{pic}} + \dot{\mathbf{r}}_i \times \mathbf{B}^{\mathrm{pic}}) \right] d^3 r}_{\mathbf{f}_i^{\mathrm{mic}}} \\ &+ \underbrace{\int \rho_i^{\mathrm{pic}} (\mathbf{E}^{\mathrm{pic}} + \dot{\mathbf{r}}_i \times \mathbf{B}^{\mathrm{pic}}) d^3 r}_{\mathbf{f}_i^{\mathrm{pic}}} . \end{aligned} \tag{2.9}$$

Aside from the rearrangement of the terms, this expression is still identical to the force in (2.1). To show the short-range character of the microscopic contribution $\mathbf{f}_i^{\mathrm{mic}}$, PIC and actual electric and magnetic fields have to be decomposed into their individual particle contributions. The respective total fields are then given by the sum over the field contributions created by all (j) particles. This decomposition is justified because of the linearity of Maxwell's equations and leads to

$$\mathbf{f}_i^{\mathrm{mic}} = \sum_j \int [\rho_i (\mathbf{E}_j + \dot{\mathbf{r}}_i \times \mathbf{B}_j) - \rho_i^{\mathrm{pic}} (\mathbf{E}_j^{\mathrm{pic}} + \dot{\mathbf{r}}_i \times \mathbf{B}_j^{\mathrm{pic}})] d^3 r. \tag{2.10}$$

The above sum describes the force on the i-th particle, created by the fields of all other (j) particles[3]. For large distances between particles j and i ($r_{ij} \gg w_{\mathrm{pic}}$), the actual and PIC fields produced in the region $\mathbf{r} \approx \mathbf{r}_i$ are identical[4]. Therefore, remaining

[3] Self-force contributions cancel out automatically.

[4] Here it is assumed that w_{pic} is much smaller than all scales of the radiated fields.

contributions to $\mathbf{f}_i^{\mathrm{mic}}$ in the far field could only stem from the different actual and PIC particle densities.

The variation of the (actual and PIC) fields over the PIC particle extent can be approximated by a linear Taylor expansion around $\mathbf{r}_i$. The corresponding expansion for the actual electric field reads

$$\mathbf{E}_j(\mathbf{r}) = \mathbf{E}_j(\mathbf{r}_i) + \nabla \mathbf{E}_j(\mathbf{r}_i)(\mathbf{r} - \mathbf{r}_i) + \dots \tag{2.11}$$

Carrying out the corresponding integration

$$\int \rho_i(\mathbf{r})\, \mathbf{E}_j(\mathbf{r}) d^3r = \underbrace{\int \rho_i(\mathbf{r})\, \mathbf{E}_j(\mathbf{r}_i) d^3r}_{=\mathbf{E}_j(\mathbf{r}_i)\int \rho_i(\mathbf{r}) d^3r} + \underbrace{\int \rho_i(\mathbf{r})\, \nabla \mathbf{E}_j(\mathbf{r}_i)(\mathbf{r} - \mathbf{r}_i) d^3r}_{=0} + \dots, \tag{2.12}$$

gives zero for the linear field terms due to the even symmetry of the charge density. If higher order terms are negligible only the constant field terms remain and can be pulled out of the integral

$$\begin{aligned} \int \rho_i(\mathbf{r})\, \mathbf{E}_j(\mathbf{r}) d^3r &= \mathbf{E}_j(\mathbf{r}_i) \int \rho_i(\mathbf{r}) d^3r & (2.13)\\ &= q_i \mathbf{E}_j(\mathbf{r}_i). & (2.14) \end{aligned}$$

The remaining integral over the particle density yields the particle charge. As the total charges of actual and PIC particles are equal, their contributions cancel each other for each index j in (2.10), proving the short range nature of the microscopic correction for the electric field. Analogous steps show the short range nature of the magnetic field term. Note, that the interaction of the plasma particles is described exactly with the force from (2.9), independent of the width of the particles on the PIC level. The value of the PIC particle width only determines the softness of the force on the PIC level and, in turn, the radius within which the Mic forces contribute.

The MicPIC approximation

So far, the above force decomposition has only formal character as everything has been derived in full generality. However, in order to facilitate the numerical evaluation of the short range interaction; field retardation is neglected locally, i.e. within the microscopic correction. This is the only formal approximation in MicPIC. Taking the non-relativistic, electrostatic limit of (2.10) by dropping magnetic fields and expressing electric fields by the respective Coulomb interaction yields

$$\mathbf{f}_i^{\mathrm{mic}} = -\nabla_{\mathbf{r}_i} \sum_j \int\int \left[\frac{\rho_i(\mathbf{r})\rho_j(\mathbf{r}')}{4\pi\varepsilon_0|\mathbf{r} - \mathbf{r}'|} - \frac{\rho_i^{\mathrm{pic}}(\mathbf{r})\rho_j^{\mathrm{pic}}(\mathbf{r}')}{4\pi\varepsilon_0|\mathbf{r} - \mathbf{r}'|} \right] d^3r' d^3r. \tag{2.15}$$

For Gaussian shape functions the above double integral can be evaluated analytically and yields the difference of the particle interaction energies for actual and PIC particles

(for more details, see appendix B). The interaction energy of two Gaussian particles with width parameter w is given by

$$V_{ij}(r_{ij}, w) = \frac{q_i q_j}{4\pi\varepsilon_0 r_{ij}} \mathrm{erf}\left(\frac{r_{ij}}{\sqrt{2}w}\right). \tag{2.16}$$

Inserting this expression into (2.15) yields

$$\mathbf{f}_i^{\mathrm{mic}} = -\sum_j \nabla_{\mathbf{r}_i} V_{ij}^{\mathrm{mic}} \tag{2.17}$$

with

$$V_{ij}^{\mathrm{mic}} = V_{ij}(r_{ij}, w_0) - V_{ij}(r_{ij}, w_{\mathrm{pic}}) \tag{2.18}$$

and $r_{ij} = |\mathbf{r}_j - \mathbf{r}_i|$ the inter-particle distance. Combining the electrostatically approximated microscopic correction in (2.17) and the PIC force in (2.8) yields the total MicPIC force

$$\mathbf{f}_i = -\sum_j \nabla_{\mathbf{r}_i} V_{ij}^{\mathrm{mic}} + \int \rho_i^{\mathrm{pic}} (\mathbf{E}^{\mathrm{pic}} + \dot{\mathbf{r}}_i \times \mathbf{B}^{\mathrm{pic}}) d^3 r. \tag{2.19}$$

The complete MicPIC dynamics is now determined by the self-consistent integration of Newton's equations of motion with the force specified in (2.19), together with the propagation of the electromagnetic fields according to equations (2.6) and (2.7).

2.2. Numerical aspects of MicPIC

This section discusses the most important numerical aspects of the implementation of the MicPIC concept. In the first part (Sec. 2.2.1), the numerical propagation of the electromagnetic fields via the Finite-Difference-Time-Domain (FDTD) algorithm is described. Special focus is put on the derivation of the field propagation algorithm on a discretized staggered spatial grid as well as the implementation of appropriate absorbing boundary conditions to emulate an infinite simulation volume. In the second part (Sec. 2.2.2), the representation of the Gaussian particles on the numerical grid is discussed in more detail. This is of particular importance, as the particle shape and its representation on the grid determines major properties of the code, like charge conservation, force anisotropy, and numerical effort. After that, the implementation and efficient evaluation of the short range forces is discussed in section 2.2.3. Subsequently, the Boris scheme for particle propagation in the presence of electromagnetic fields is derived (Sec. 2.2.4), completing the basic part of the code. Finally the implementation of atomic ionization processes into MicPIC is described in section 2.2.5.321

2.2.1. Electromagnetic field propagation with the Finite-difference time-domain method

The foundation of the MicPIC approach is the numerical description of the time evolution of the electric- and magnetic fields on the PIC level according to equations (2.6)

and (2.7). In this work the Finite-Difference-Time-Domain method has been chosen for that purpose, as it solves Maxwell's equations in the time domain and is relatively simple to implement. In the following the FDTD idea and its implementation are discussed in detail. As a starting point the basic equations are repeated here for convenience

$$\boldsymbol{\nabla} \times \boldsymbol{E} = -\dot{\boldsymbol{B}} \tag{2.20a}$$

$$\boldsymbol{\nabla} \times \boldsymbol{B} = \mu_0 \left(\boldsymbol{j} + \varepsilon_0 \dot{\boldsymbol{E}} \right) \tag{2.20b}$$

with the electric field $\boldsymbol{E}$, the magnetic field $\boldsymbol{B}$, the vacuum permittivity ε_0 and permeability μ_0 as well as the electric current density $\boldsymbol{j}$. As fields and currents are exclusively discussed for the PIC level in this section, the superscript "pic" has been dropped. Writing out the vector components of equations (2.20a) and (2.20b) yields the following system of six coupled first order differential equations:

$$\frac{\partial E_x}{\partial t} = \frac{1}{\varepsilon_0 \mu_0} \left[\frac{\partial B_z}{\partial y} - \frac{\partial B_y}{\partial z} \right] - \frac{1}{\varepsilon_0} j_x \tag{2.21a}$$

$$\frac{\partial E_y}{\partial t} = \frac{1}{\varepsilon_0 \mu_0} \left[\frac{\partial B_x}{\partial z} - \frac{\partial B_z}{\partial x} \right] - \frac{1}{\varepsilon_0} j_y \tag{2.21b}$$

$$\frac{\partial E_z}{\partial t} = \frac{1}{\varepsilon_0 \mu_0} \left[\frac{\partial B_y}{\partial x} - \frac{\partial B_x}{\partial y} \right] - \frac{1}{\varepsilon_0} j_z \tag{2.21c}$$

$$\frac{\partial B_x}{\partial t} = \left[\frac{\partial E_y}{\partial z} - \frac{\partial E_z}{\partial y} \right] \tag{2.21d}$$

$$\frac{\partial B_y}{\partial t} = \left[\frac{\partial E_z}{\partial x} - \frac{\partial E_x}{\partial z} \right] \tag{2.21e}$$

$$\frac{\partial B_z}{\partial t} = \left[\frac{\partial E_x}{\partial y} - \frac{\partial E_y}{\partial x} \right] \tag{2.21f}$$

The basic idea for the solution of this problem in the framework of the FDTD algorithm has been proposed by Kane Yee already in 1966 [55]. It is based on a specific space and time staggering of the field components in conjunction with the centered finite difference scheme to discretize the space and time derivatives.

Centered finite difference

To derive a finite difference expression for the spatial derivative of a scalar function $u(x, t_n)$ it is convenient to consider its Taylor series expansion around space point x_i at a fixed time t_n. For positive displacements in space the expansion is given by

$$\begin{aligned} u(x_i + \Delta x) \,|_{t_n} = \; & u \,|_{x_i,t_n} + \Delta x \cdot \tfrac{\partial u}{\partial x} \,|_{x_i,t_n} + \tfrac{(\Delta x)^2}{2} \cdot \tfrac{\partial^2 u}{\partial x^2} \,|_{x_i,t_n} \\ & + \tfrac{(\Delta x)^3}{6} \cdot \tfrac{\partial^3 u}{\partial x^3} \,|_{x_i,t_n} + \tfrac{(\Delta x)^4}{24} \cdot \tfrac{\partial^4 u}{\partial x^4} \,|_{x_i,t_n} + \ldots \end{aligned} \tag{2.22}$$

and for negative displacements by

$$\begin{aligned} u(x_i - \Delta x) \,|_{t_n} = \; & u \,|_{x_i,t_n} - \Delta x \cdot \tfrac{\partial u}{\partial x} \,|_{x_i,t_n} + \tfrac{(\Delta x)^2}{2} \cdot \tfrac{\partial^2 u}{\partial x^2} \,|_{x_i,t_n} \\ & - \tfrac{(\Delta x)^3}{6} \cdot \tfrac{\partial^3 u}{\partial x^3} \,|_{x_i,t_n} + \tfrac{(\Delta x)^4}{24} \cdot \tfrac{\partial^4 u}{\partial x^4} \,|_{x_i,t_n} + \ldots \end{aligned} \tag{2.23}$$

Subtracting both equations leads to

$$u(x_i + \Delta x) \mid_{t_n} - u(x_i - \Delta x) \mid_{t_n} = 2\Delta x \cdot \frac{\partial u}{\partial x} \mid_{x_i,t_n} + \frac{(\Delta x)^3}{3} \cdot \frac{\partial^3 u}{\partial x^3} \mid_{x_i,t_n} + \dots \tag{2.24}$$

Now, rearranging the terms results in a centered finite difference expression for the derivative

$$\left.\frac{\partial u}{\partial x}\right|_{x_i,t_n} = \frac{u(x_i + \Delta x) \mid_{t_n} - u(x_i - \Delta x) \mid_{t_n}}{2\Delta x} + \mathcal{O}[(\Delta x)^2] \tag{2.25}$$

with second order accuracy. The actual field and current components are functions of three space and one time coordinate. For convenience the shorter notation

$$u(i\Delta x, j\Delta y, k\Delta z, n\Delta t) = u^n_{i,j,k} \tag{2.26}$$

is used from here on. Evaluating the Taylor expansions with half displacements $x_i \pm \frac{\Delta x}{2}$ leads to the final expressions for the space and time derivatives

$$\frac{\partial u}{\partial x}(i\Delta x, j\Delta y, k\Delta z, n\Delta t) = \frac{u^n_{i+\frac{1}{2},j,k} - u^n_{i-\frac{1}{2},j,k}}{\Delta x} + \mathcal{O}[(\Delta x)^2] \tag{2.27a}$$

$$\frac{\partial u}{\partial y}(i\Delta x, j\Delta y, k\Delta z, n\Delta t) = \frac{u^n_{i,j+\frac{1}{2},k} - u^n_{i,j-\frac{1}{2},k}}{\Delta y} + \mathcal{O}[(\Delta y)^2] \tag{2.27b}$$

$$\frac{\partial u}{\partial z}(i\Delta x, j\Delta y, k\Delta z, n\Delta t) = \frac{u^n_{i,j,k+\frac{1}{2}} - u^n_{i,j,k-\frac{1}{2}}}{\Delta z} + \mathcal{O}[(\Delta z)^2] \tag{2.27c}$$

$$\frac{\partial u}{\partial t}(i\Delta x, j\Delta y, k\Delta z, n\Delta t) = \frac{u^{n+\frac{1}{2}}_{i,j,k} - u^{n-\frac{1}{2}}_{i,j,k}}{\Delta t} + \mathcal{O}[(\Delta t)^2] \tag{2.27d}$$

which will be used in the following.

The Yee staggering

The positioning of the electric and magnetic field components on the numerical grid according to the work of Kane Yee [55] is shown in figure 2.1. The reason for this specific staggering becomes evident when the above finite difference expressions are applied to the field equations. Doing this exemplarily for equation (2.21a) yields

$$\begin{aligned} \frac{E_x \mid^{n+\frac{1}{2}}_{i+\frac{1}{2},j,k} - E_x \mid^{n-\frac{1}{2}}_{i+\frac{1}{2},j,k}}{\Delta t} &= \frac{1}{\varepsilon_0}\left[\frac{B_z \mid^n_{i+\frac{1}{2},j+\frac{1}{2},k} - B_z \mid^n_{i+\frac{1}{2},j-\frac{1}{2},k}}{\Delta y} - \frac{B_y \mid^n_{i+\frac{1}{2},j,k+\frac{1}{2}} - B_y \mid^n_{i+\frac{1}{2},j,k-\frac{1}{2}}}{\Delta z}\right] \\ &- \frac{1}{\varepsilon_0} j_x \mid^n_{i+\frac{1}{2},j,k} . \end{aligned} \tag{2.28}$$

Rearranging the terms leads to an explicit expression for the propagation of E_x

$$\begin{aligned} E_x \mid^{n+\frac{1}{2}}_{i+\frac{1}{2},j,k} &= E_x \mid^{n-\frac{1}{2}}_{i+\frac{1}{2},j,k} \\ &+ \frac{\Delta t}{\varepsilon_0}\left[\frac{B_z \mid^n_{i+\frac{1}{2},j+\frac{1}{2},k} - B_z \mid^n_{i+\frac{1}{2},j-\frac{1}{2},k}}{\Delta y} - \frac{B_y \mid^n_{i+\frac{1}{2},j,k+\frac{1}{2}} - B_y \mid^n_{i+\frac{1}{2},j,k-\frac{1}{2}}}{\Delta z}\right] \\ &- \frac{\Delta t}{\varepsilon_0} j_x \mid^n_{i+\frac{1}{2},j,k} \end{aligned} \tag{2.29}$$

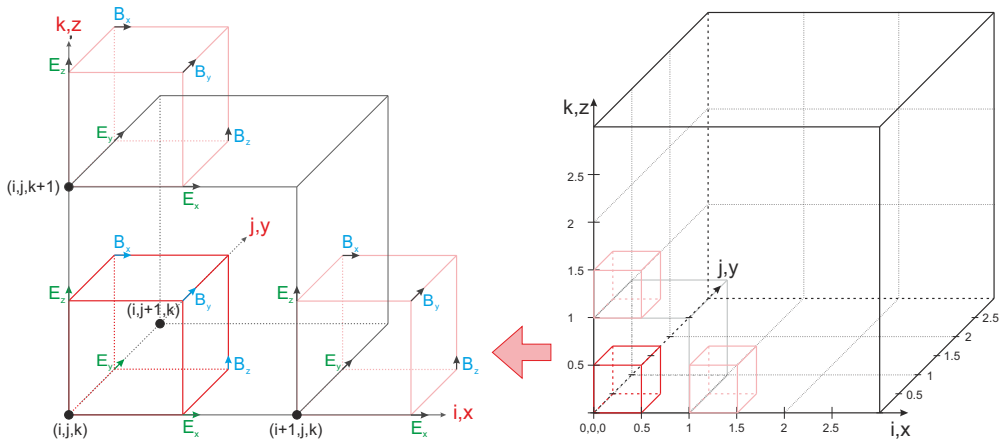

Figure 2.1.: Schematic illustration of the field staggering as proposed by Kane Yee [55]. Electric and magnetic field components are chosen such that the positions fit automatically to a centered finite differences solution to the curl equations.

that only relies on the knowledge of all field components in the past. Comparing the positions of the required field components in (2.29) with the positions in figure 2.1 shows that the Yee-staggering is perfectly matched to this propagation scheme. Similar expressions can be derived for the other field components, completing the basic numerical recipe for the numerical solution to Maxwell's equations. Note that the electric and magnetic field components are also staggered in time, which results in alternating field updates for electric and magnetic fields.

Absorbing boundary conditions

The FDTD-scheme introduced above represents a very efficient way to solve the microscopic Maxwell's equations on a numerical grid. As such a grid consumes memory it will always be limited in size, such that some sort of boundary conditions have to be applied. In principle, there are three main types of boundary conditions, suitable for different physical problems. The **P**erfect-**E**lectric-**C**onductor boundary condition mimics a perfect metal surface to truncate the computational grid, reflecting all impinging electromagnetic waves. **P**eriodic **B**oundary **C**onditions emulate a periodic continuation of the computational domain. This can be very useful for the simulation of effective lower-dimensional problems like planar surfaces. The third and for this work most important type of boundary condition is the **A**bsorbing-**B**oundary-**C**ondition. It simulates the extension of the lattice to infinity.

The basic idea: An obvious approach to achieve ABC's is to enclose the computational box with a highly absorbing medium layer. The main goal of such an electromagnetic absorbtion layer is to obtain dissipation within the layer without reflection from the interface back into the main simulation volume. From a numerical point of view, this can be achieved by using Maxwell's curl equations for a dissipative medium.

The corresponding equations read

$$\nabla \times \boldsymbol{H} = \frac{\partial \boldsymbol{D}}{\partial t} + \sigma \boldsymbol{E} \tag{2.30a}$$

$$\nabla \times \boldsymbol{E} = -\frac{\partial \boldsymbol{B}}{\partial t} - \sigma^* \boldsymbol{H} \tag{2.30b}$$

with the electric conductivity σ and the equivalent magnetic loss σ^* determining the dissipative properties of the medium . For linear, isotropic and nondispersive materials $\boldsymbol{D}$ and $\boldsymbol{E}$ as well as $\boldsymbol{B}$ and $\boldsymbol{H}$ can be related by simple proportions

$$\boldsymbol{D} = \varepsilon_0 \varepsilon_r \boldsymbol{E} = \varepsilon \boldsymbol{E} \tag{2.31a}$$

$$\boldsymbol{B} = \mu_0 \mu_r \boldsymbol{H} = \mu \boldsymbol{H}. \tag{2.31b}$$

Inserting these expressions into (2.30) eliminates $\boldsymbol{D}$ and $\boldsymbol{B}$ and leads to

$$\nabla \times \boldsymbol{H} = \varepsilon \frac{\partial \boldsymbol{E}}{\partial t} + \sigma \boldsymbol{E} \tag{2.32a}$$

$$\nabla \times \boldsymbol{E} = -\mu \frac{\partial \boldsymbol{H}}{\partial t} - \sigma^* \boldsymbol{H}. \tag{2.32b}$$

For the following derivation, it is convenient to translate these equations into the frequency domain, which yields a very compact notation

$$\nabla \times \breve{\boldsymbol{H}} = i\omega\varepsilon \breve{\boldsymbol{E}} + \sigma \breve{\boldsymbol{E}} = i\omega\varepsilon \left(1 + \frac{\sigma}{i\omega\varepsilon}\right) \breve{\boldsymbol{E}} = i\omega\varepsilon\lambda_\varepsilon \breve{\boldsymbol{E}} \tag{2.33a}$$

$$\nabla \times \breve{\boldsymbol{E}} = -i\omega\mu \breve{\boldsymbol{H}} - \sigma^* \breve{\boldsymbol{H}} = -i\omega\mu \left(1 + \frac{\sigma^*}{i\omega\mu}\right) \breve{\boldsymbol{H}} = -i\omega\mu\lambda_\mu \breve{\boldsymbol{H}} \tag{2.33b}$$

with the new material parameters λ_ε and λ_μ. Note that quantities in the frequency domain are flagged with a breve from here on.

Plane wave incident on a lossy have space: Eventually the main simulation volume should be completely surrounded by an absorbing medium layer. However, as a first step, the reflection properties of the interface between absorbing and non-absorbing regions have to be evaluated. To this end, the incidence of a plane wave upon such an interface between a lossless (region 1, $x < 0$) and a lossy half-space (region 2, $x > 0$) is studied in more detail. Consider an incident wave defined by

$$\breve{\boldsymbol{H}}^{\text{inc}} = \boldsymbol{e}_z H_0 \, e^{-i\beta_{1x}x - i\beta_{1y}y} \tag{2.34a}$$

$$\breve{\boldsymbol{E}}^{\text{inc}} = \left[-\boldsymbol{e}_x \frac{\beta_{1y}}{\omega\varepsilon} + \boldsymbol{e}_y \frac{\beta_{1x}}{\omega\varepsilon}\right] \, H_0 e^{-i\beta_{1x}x - i\beta_{1y}y} \tag{2.34b}$$

with the wave vector

$$\boldsymbol{\beta}_1 = \beta_{1x}\boldsymbol{e}_x + \beta_{1y}\boldsymbol{e}_y; \quad \beta_{1x} = k_1 \cos\Theta; \quad \beta_{1y} = k_1 \sin\Theta \tag{2.35}$$

and the angle of incidence Θ. Then, according to equation (2.33), the total fields in Region 1 ($\sigma = \sigma^* = 0$) are given by

$$\breve{\boldsymbol{H}}_1 = \boldsymbol{e}_z H_0 \left(1 + \Gamma e^{2i\beta_{1x}x}\right)\ e^{-i\beta_{1x}x - i\beta_{1y}y} \tag{2.36a}$$

$$\breve{\boldsymbol{E}}_1 = \left[-\boldsymbol{e}_x \frac{\beta_{1y}}{\omega\varepsilon}\left(1 + \Gamma e^{2i\beta_{1x}x}\right) + \boldsymbol{e}_y \frac{\beta_{1x}}{\omega\varepsilon}\left(1 - \Gamma e^{2i\beta_{1x}x}\right)\right] H_0 e^{-i\beta_{1x}x - i\beta_{1y}y}, \tag{2.36b}$$

where Γ is the reflection coefficient. The total fields in region 2 are given by

$$\breve{\boldsymbol{H}}_2 = \boldsymbol{e}_z H_0 \tau\ e^{-i\beta_{2x}x - i\beta_{2y}y} \tag{2.37a}$$

$$\breve{\boldsymbol{E}}_2 = \left[-\boldsymbol{e}_x \frac{\beta_{2y}}{\omega\varepsilon\lambda_\varepsilon} + \boldsymbol{e}_y \frac{\beta_{2x}}{\omega\varepsilon\lambda_\varepsilon}\right] H_0 \tau e^{-i\beta_{2x}x - i\beta_{2y}y} \tag{2.37b}$$

with the transmission coefficient τ. Enforcing continuity of the tangential fields across the region 1 / region 2 interface at x=0 yields expressions for the reflection and transmission coefficients

$$\Gamma = \frac{\frac{\beta_{1x}}{\omega\varepsilon} - \frac{\beta_{2x}}{\omega\varepsilon\lambda_\varepsilon}}{\frac{\beta_{1x}}{\omega\varepsilon} + \frac{\beta_{2x}}{\omega\varepsilon\lambda_\varepsilon}}; \quad \tau = 1 + \Gamma. \tag{2.38}$$

For arbitrary angles of incidence Θ the reflection coefficient is in general nonzero. However, it can be shown that for normal incidence ($\Theta = 0$) and an appropriate choice of the parameters, i.e. $\lambda_\varepsilon = \lambda_\mu \Rightarrow \sigma^* = \sigma\mu/\varepsilon$, plane electromagnetic waves can enter the lossy half-space without reflection, irrespective of their frequency. Then, the transmitted fields given by

$$\breve{\boldsymbol{H}}_2 = \breve{\boldsymbol{H}}^{\mathrm{inc}} e^{-\sigma\sqrt{\mu/\varepsilon}\,x} \tag{2.39a}$$

$$\breve{\boldsymbol{E}}_2 = \breve{\boldsymbol{E}}^{\mathrm{inc}} e^{-\sigma\sqrt{\mu/\varepsilon}\,x} \tag{2.39b}$$

resemble the incident fields, but exhibit additional exponential damping in region 2. In this case, region 2 is called perfectly matched to region 1 for normal incident waves [56]. However, to be of practical use the observed behavior is needed for arbitrary angles of incidence.

The uniaxial perfectly matched layer: A first solution to this problem has been presented by Berenger in 1994 in terms of the so called **P**erfectly **M**atched **L**ayer [57]. Berenger used a split-field formulation of Maxwell's equations, which leads to a set of 12 coupled first-order differential equations. With an appropriate choice of the loss parameters a perfectly matched interface for arbitrary wave incidence, polarization and frequency can be derived.

In MicPIC an alternative but equivalent formulation is utilized, the so called **U**niaxial-**P**erfectly-**M**atched-**L**ayer (UPML) introduced by Stephen Gedney in 1996 [58]. The main idea behind the UPML concept is to achieve perfect matching at the interface via an uniaxial anisotropic absorbtion layer. Therefore, the isotropic material parameters λ_ε and λ_μ in equations (2.33) are replaced by uniaxial tensors. Considering an interface perpendicular to the x-axis, similar to the isotropic case discussed above, the

tensor parameters exhibit a form that is rotationally symmetric about the x-axis

$$\bar{\bar{\lambda}}_\varepsilon = \begin{pmatrix} a & 0 & 0 \\ 0 & b & 0 \\ 0 & 0 & b \end{pmatrix} \quad \bar{\bar{\lambda}}_\mu = \begin{pmatrix} c & 0 & 0 \\ 0 & d & 0 \\ 0 & 0 & d \end{pmatrix}. \tag{2.40}$$

Maxwell's curl equations in the frequency domain than read

$$\nabla \times \breve{\boldsymbol{H}} = i\omega\varepsilon \bar{\bar{\lambda}}_\varepsilon \breve{\boldsymbol{E}} \tag{2.41a}$$

$$\nabla \times \breve{\boldsymbol{E}} = -i\omega\mu \bar{\bar{\lambda}}_\mu \breve{\boldsymbol{H}}. \tag{2.41b}$$

The examination of an incident plane wave onto the region interface (analogous to the case discussed above) shows that reflectionless transmission of plane waves from the main simulation volume into the UPML region can be achieved for

$$\bar{\bar{\lambda}}_\varepsilon = \bar{\bar{\lambda}}_\mu = \bar{\bar{s}} = \begin{pmatrix} s_x^{-1} & 0 & 0 \\ 0 & s_x & 0 \\ 0 & 0 & s_x \end{pmatrix}, \tag{2.42}$$

irrespective of the angle of incidence, polarization and frequency of the incident wave (for more details see [58–60]). The reflectionless property of the interface holds for any s_x. Defining it similar to the isotropic absorbing layer case discussed above

$$s_x = \left(1 + \frac{\sigma_x}{i\omega\varepsilon}\right) \tag{2.43}$$

creates a reflectionless absorbing layer as intended. Considering a plane wave incident on an interface at $x = 0$ analogous to the isotropic case discussed above

$$\breve{\boldsymbol{H}}^{\text{inc}} = \boldsymbol{e}_z H_0 \, e^{-i\beta_{1x}x - i\beta_{1y}y} \tag{2.44a}$$

$$\breve{\boldsymbol{E}}^{\text{inc}} = \left[-\boldsymbol{e}_x \frac{\beta_{1y}}{\omega\varepsilon} + \boldsymbol{e}_y \frac{\beta_{1x}}{\omega\varepsilon}\right] H_0 e^{-i\beta_{1x}x - i\beta_{1y}y} \tag{2.44b}$$

leads to the following transmitted fields

$$\breve{\boldsymbol{H}}^{\text{UPML}} = \boldsymbol{e}_z H_0 \, e^{-i\beta_{1x}x - i\beta_{1y}y} e^{-\sigma_x \sqrt{\mu/\varepsilon}\cos\Theta\, x} \tag{2.45a}$$

$$\breve{\boldsymbol{E}}^{\text{UPML}} = \left[-\boldsymbol{e}_x s_x \frac{\beta_{1y}}{\omega\varepsilon} + \boldsymbol{e}_y \frac{\beta_{1x}}{\omega\varepsilon}\right] H_0 e^{-i\beta_{1x}x - i\beta_{1y}y} e^{-\sigma_x \sqrt{\mu/\varepsilon}\cos\Theta\, x}. \tag{2.45b}$$

The transmitted waves propagate with the same phase velocity as the incident wave but undergo exponential decay along the axis normal to the region interface. The magnitude of the decay depends on the angle of incidence Θ and can be additionally adjusted by an appropriate choice of the UPML parameter σ_x.

So far only the construction of a reflectionless planar interface between two half-spaces has been discussed. To truncate a finite three dimensional simulation volume,

absorption layers adjacent to all outer lattice boundaries are needed. To this end a general material tensor can be defined

$$\begin{aligned}\bar{\bar{s}} &= \begin{pmatrix} s_x^{-1} & 0 & 0 \\ 0 & s_x & 0 \\ 0 & 0 & s_x \end{pmatrix} \begin{pmatrix} s_y & 0 & 0 \\ 0 & s_y^{-1} & 0 \\ 0 & 0 & s_y \end{pmatrix} \begin{pmatrix} s_z & 0 & 0 \\ 0 & s_z & 0 \\ 0 & 0 & s_z^{-1} \end{pmatrix} \\ &= \begin{pmatrix} s_x^{-1} s_y s_z & 0 & 0 \\ 0 & s_x s_y^{-1} s_z & 0 \\ 0 & 0 & s_x s_y s_z^{-1} \end{pmatrix} \end{aligned} \tag{2.46}$$

where

$$s_x = 1 + \frac{\sigma_x}{i\omega\varepsilon}; \quad s_y = 1 + \frac{\sigma_y}{i\omega\varepsilon}; \quad s_z = 1 + \frac{\sigma_z}{i\omega\varepsilon}. \tag{2.47}$$

This tensor is sufficient to describe the anisotropic PML medium in the entire FDTD simulation volume. By properly choosing the spatial dependence of σ_x, σ_y and σ_z

$$\sigma_x(x) = \begin{cases} \sigma_x'(x) & x \le x_{min}, \ge x_{max} \\ 0 & x_{min} < x < x_{max} \end{cases} \tag{2.48a}$$

$$\sigma_y(y) = \begin{cases} \sigma_y'(y) & y \le y_{min}, \ge y_{max} \\ 0 & y_{min} < y < y_{max} \end{cases} \tag{2.48b}$$

$$\sigma_z(z) = \begin{cases} \sigma_z'(z) & z \le z_{min}, \ge z_{max} \\ 0 & z_{min} < z < z_{max} \end{cases} \tag{2.48c}$$

the tensor becomes the unit dyad in the main simulation volume, while it is still properly expressed in the PML regions. The final equations to solve read now

$$\begin{bmatrix} \frac{\partial \breve{H}_z}{\partial y} - \frac{\partial \breve{H}_y}{\partial z} \\ \frac{\partial \breve{H}_x}{\partial z} - \frac{\partial \breve{H}_z}{\partial x} \\ \frac{\partial \breve{H}_y}{\partial x} - \frac{\partial \breve{H}_x}{\partial y} \end{bmatrix} = i\omega\varepsilon \begin{bmatrix} \frac{s_y s_z}{s_x} & 0 & 0 \\ 0 & \frac{s_x s_z}{s_y} & 0 \\ 0 & 0 & \frac{s_x s_y}{s_z} \end{bmatrix} \begin{bmatrix} \breve{E}_x \\ \breve{E}_y \\ \breve{E}_z \end{bmatrix} \tag{2.49}$$

and

$$\begin{bmatrix} \frac{\partial \breve{E}_z}{\partial y} - \frac{\partial \breve{E}_y}{\partial z} \\ \frac{\partial \breve{E}_x}{\partial z} - \frac{\partial \breve{E}_z}{\partial x} \\ \frac{\partial \breve{E}_y}{\partial x} - \frac{\partial \breve{E}_x}{\partial y} \end{bmatrix} = -i\omega\mu \begin{bmatrix} \frac{s_y s_z}{s_x} & 0 & 0 \\ 0 & \frac{s_x s_z}{s_y} & 0 \\ 0 & 0 & \frac{s_x s_y}{s_z} \end{bmatrix} \begin{bmatrix} \breve{H}_x \\ \breve{H}_y \\ \breve{H}_z \end{bmatrix}. \tag{2.50}$$

However, the direct transformation of these equations back into the time domain would lead to a convolution of the tensor coefficients and the magnetic and electric fields, respectively. This would be computationally very expensive, but can be circumvented by the definition of the following relationships [58]

$$\breve{D}_x = \varepsilon \frac{s_z}{s_x} \breve{E}_x \quad , \quad \breve{D}_y = \varepsilon \frac{s_x}{s_y} \breve{E}_y \quad , \quad \breve{D}_z = \varepsilon \frac{s_y}{s_z} \breve{E}_z. \tag{2.51}$$

Inserting equations (2.51) into (2.49) leads to a decoupling of the frequency dependent terms [58, 59]. Subsequent backtransformation into the time domain yields

$$\begin{bmatrix} \frac{\partial \breve{H}_z}{\partial y} - \frac{\partial \breve{H}_y}{\partial z} \\ \frac{\partial \breve{H}_x}{\partial z} - \frac{\partial \breve{H}_z}{\partial x} \\ \frac{\partial \breve{H}_y}{\partial x} - \frac{\partial \breve{H}_x}{\partial y} \end{bmatrix} = \frac{\partial}{\partial t} \begin{bmatrix} \breve{D}_x \\ \breve{D}_y \\ \breve{D}_z \end{bmatrix} + \frac{1}{\varepsilon} \begin{bmatrix} \sigma_y & 0 & 0 \\ 0 & \sigma_z & 0 \\ 0 & 0 & \sigma_x \end{bmatrix} \begin{bmatrix} \breve{D}_x \\ \breve{D}_y \\ \breve{D}_z \end{bmatrix}. \tag{2.52}$$

Analogous definitions for the magnetic fields

$$\breve{B}_x = \mu \frac{s_z}{s_x} \breve{H}_x \quad , \quad \breve{B}_y = \mu \frac{s_x}{s_y} \breve{H}_y \quad , \quad \breve{B}_z = \mu \frac{s_y}{s_z} \breve{H}_z \tag{2.53}$$

yield

$$\begin{bmatrix} \frac{\partial \breve{E}_z}{\partial y} - \frac{\partial \breve{E}_y}{\partial z} \\ \frac{\partial \breve{E}_x}{\partial z} - \frac{\partial \breve{E}_z}{\partial x} \\ \frac{\partial \breve{E}_y}{\partial x} - \frac{\partial \breve{E}_x}{\partial y} \end{bmatrix} = -\frac{\partial}{\partial t} \begin{bmatrix} \breve{B}_x \\ \breve{B}_y \\ \breve{B}_z \end{bmatrix} - \frac{1}{\varepsilon} \begin{bmatrix} \sigma_y & 0 & 0 \\ 0 & \sigma_z & 0 \\ 0 & 0 & \sigma_x \end{bmatrix} \begin{bmatrix} \breve{B}_x \\ \breve{B}_y \\ \breve{B}_z \end{bmatrix} . \tag{2.54}$$

As a last step the definitions (2.51) and (2.53) need to be transformed to the time domain as well. In the following the equation for $\breve{D}_x$ is considered exemplarily. Multiplying both sides with s_x and transforming them back leads to

$$s_x \breve{D}_x = \varepsilon s_z \breve{E}_x \tag{2.55a}$$

$$\left(1 + \frac{\sigma_x}{i\omega\varepsilon}\right) \breve{D}_x = \varepsilon \left(1 + \frac{\sigma_z}{i\omega\varepsilon}\right) \breve{E}_x \tag{2.55b}$$

$$\left(i\omega + \frac{\sigma_x}{\varepsilon}\right) \breve{D}_x = \varepsilon \left(i\omega + \frac{\sigma_z}{\varepsilon}\right) \breve{E}_x \tag{2.55c}$$

$$\frac{\partial}{\partial t}(D_x) + \frac{\sigma_x}{\varepsilon} D_x = \varepsilon \left[\frac{\partial}{\partial t}(E_x) + \frac{\sigma_z}{\varepsilon} E_x\right] . \tag{2.55d}$$

Repeating this procedure for the other 5 relations finally yields the 12 equations that need to be discritized and solved on a numerical grid:

$$\frac{\partial\ D_x}{\partial t} = \left[\frac{\partial H_z}{\partial y} - \frac{\partial H_y}{\partial z} - \frac{\sigma_y}{\varepsilon} D_x\right] \quad , \frac{\partial}{\partial t} D_x + \frac{\sigma_x}{\varepsilon} D_x = \varepsilon \left[\frac{\partial}{\partial t} E_x + \frac{\sigma_z}{\varepsilon} E_x\right] \tag{2.56a}$$

$$\frac{\partial\ D_y}{\partial t} = \left[\frac{\partial H_x}{\partial z} - \frac{\partial H_z}{\partial x} - \frac{\sigma_z}{\varepsilon} D_y\right] \quad , \frac{\partial}{\partial t} D_y + \frac{\sigma_y}{\varepsilon} D_y = \varepsilon \left[\frac{\partial}{\partial t} E_y + \frac{\sigma_x}{\varepsilon} E_y\right] \tag{2.56b}$$

$$\frac{\partial\ D_z}{\partial t} = \left[\frac{\partial H_y}{\partial x} - \frac{\partial H_x}{\partial y} - \frac{\sigma_x}{\varepsilon} D_z\right] \quad , \frac{\partial}{\partial t} D_z + \frac{\sigma_z}{\varepsilon} D_z = \varepsilon \left[\frac{\partial}{\partial t} E_z + \frac{\sigma_y}{\varepsilon} E_z\right] \tag{2.56c}$$

$$\frac{\partial\ B_x}{\partial t} = \left[\frac{\partial E_y}{\partial z} - \frac{\partial E_z}{\partial y} - \frac{\sigma_y}{\varepsilon} B_x\right] \quad , \frac{\partial}{\partial t} B_x + \frac{\sigma_x}{\varepsilon} B_x = \mu \left[\frac{\partial}{\partial t} H_x + \frac{\sigma_z}{\varepsilon} H_x\right] \tag{2.56d}$$

$$\frac{\partial\ B_y}{\partial t} = \left[\frac{\partial E_z}{\partial x} - \frac{\partial E_x}{\partial z} - \frac{\sigma_z}{\varepsilon} B_y\right] \quad , \frac{\partial}{\partial t} B_y + \frac{\sigma_y}{\varepsilon} B_y = \mu \left[\frac{\partial}{\partial t} H_y + \frac{\sigma_x}{\varepsilon} H_y\right] \tag{2.56e}$$

$$\frac{\partial\ B_z}{\partial t} = \left[\frac{\partial E_x}{\partial y} - \frac{\partial E_y}{\partial x} - \frac{\sigma_x}{\varepsilon} B_z\right] \quad , \frac{\partial}{\partial t} B_z + \frac{\sigma_z}{\varepsilon} B_z = \mu \left[\frac{\partial}{\partial t} H_z + \frac{\sigma_y}{\varepsilon} H_z\right] \tag{2.56f}$$

Note that in regions with $\sigma_x = \sigma_y = \sigma_x = 0$ equations (2.56) reduce to the equations for the main simulation volume (2.21) without currents. Therefore this scheme (2.56) is used throughout the whole simulation volume, while currents are only assigned within the main region.

The final discritized expressions: Utilizing the finite difference expressions, the set of final equations (2.56) can be discretized on the computational grid. For the sake of

brevity the resulting expressions are given here only for the propagation of E_x, they read

$$\begin{aligned} D_x\,|^{n+\frac{1}{2}}_{i+\frac{1}{2},j,k} &= C^{1,E_x}_{i+\frac{1}{2},j,k}\, D_x\,|^{n-\frac{1}{2}}_{i+\frac{1}{2},j,k} \\ &+ C^{2,E_x}_{i+\frac{1}{2},j,k}\left[\frac{H_z\,|^{n}_{i+\frac{1}{2},j+\frac{1}{2},k} - H_z\,|^{n}_{i+\frac{1}{2},j-\frac{1}{2},k}}{\Delta y} - \frac{H_y\,|^{n}_{i+\frac{1}{2},j,k+\frac{1}{2}} - H_y\,|^{n}_{i+\frac{1}{2},j,k-\frac{1}{2}}}{\Delta z}\right] \end{aligned}$$

and

$$E_x\,|^{n+\frac{1}{2}}_{i+\frac{1}{2},j,k} = C^{3,E_x}_{i+\frac{1}{2},j,k}\, E_x\,|^{n-\frac{1}{2}}_{i+\frac{1}{2},j,k} + C^{4,E_x}_{i+\frac{1}{2},j,k}\, C^{5,E_x}_{i+\frac{1}{2},j,k}\, D_x\,|^{n+\frac{1}{2}}_{i+\frac{1}{2},j,k} - C^{4,E_x}_{i+\frac{1}{2},j,k}\, C^{6,E_x}_{i+\frac{1}{2},j,k}\, D_x\,|^{n-\frac{1}{2}}_{i+\frac{1}{2},j,k}$$

with the position dependent coefficients defined by:

$$C^{1,E_x}_{i+\frac{1}{2},j,k} = \frac{2\varepsilon_0 - \Delta t\sigma_{y,i+\frac{1}{2},j,k}}{2\varepsilon_0 + \Delta t\sigma_{y,i+\frac{1}{2},j,k}} \tag{2.57}$$

$$C^{2,E_x}_{i+\frac{1}{2},j,k} = \frac{2\varepsilon_0\Delta t}{2\varepsilon_0 + \Delta t\sigma_{y,i+\frac{1}{2},j,k}} \tag{2.58}$$

$$C^{3,E_x}_{i+\frac{1}{2},j,k} = \frac{2\varepsilon_0 - \Delta t\sigma_{z,i+\frac{1}{2},j,k}}{2\varepsilon_0 + \Delta t\sigma_{z,i+\frac{1}{2},j,k}} \tag{2.59}$$

$$C^{4,E_x}_{i+\frac{1}{2},j,k} = \frac{1}{2\varepsilon_0\varepsilon + \Delta t\varepsilon\sigma_{z,i+\frac{1}{2},j,k}} \tag{2.60}$$

$$C^{5,E_x}_{i+\frac{1}{2},j,k} = 2\varepsilon_0 + \Delta t\sigma_{x,i+\frac{1}{2},j,k} \tag{2.61}$$

$$C^{6,E_x}_{i+\frac{1}{2},j,k} = 2\varepsilon_0 - \Delta t\sigma_{x,i+\frac{1}{2},j,k}. \tag{2.62}$$

$$\tag{2.63}$$

Note that the material parameters σ_x, σ_y and σ_z have a so far not further discussed spatial dependence. The perfectly reflectionless character of the interface between the main simulation volume and the UPML-layer only applies to the analytic description. When the discretized expressions are evaluated, every discontinuity in the material parameters causes some reflection. In order to reduce these reflections to a minimum these parameters are gradually increased towards the outer boundary of the UPML layer starting with a value of zero directly at the interface. In MicPIC a polynomial ramping is used, according to [57,60]. The UPML-layer itself is than terminated with a periodic boundary condition. The fields that reach this outer boundary are already strongly damped, are than mapped onto the opposite side of the numerical grid and further damped on their way through the second UPML layer.

Treatment of external fields: the total field - scattered field scheme

In MicPIC the external laser field is not explicitly propagated on the main grid. Instead, the total-field-scattered-field scheme is utilized. Because of the linearity of Maxwell's equations, the total electric and magnetic fields can be decomposed into

$$\boldsymbol{E}_{\text{total}} = \boldsymbol{E}_{\text{inc}} + \boldsymbol{E}_{\text{scatt}} \tag{2.64a}$$

$$\boldsymbol{B}_{\text{total}} = \boldsymbol{B}_{\text{inc}} + \boldsymbol{B}_{\text{scatt}} \tag{2.64b}$$

where $\boldsymbol{E}_{\text{inc}}$ and $\boldsymbol{B}_{\text{inc}}$ are the incident electric and magnetic wave fields. These are the fields that would exist in vacuum and are therefore assumed to be known at all lattice points and all time steps. They satisfy

$$\boldsymbol{\nabla} \times \boldsymbol{E}_{\text{inc}} = -\dot{\boldsymbol{B}}_{\text{inc}} \tag{2.65a}$$

$$\boldsymbol{\nabla} \times \boldsymbol{B}_{\text{inc}} = \mu_0 \varepsilon_0 \dot{\boldsymbol{E}}_{\text{inc}}. \tag{2.65b}$$

From equations (2.64) and (2.21) it follows directly that $\boldsymbol{E}_{\text{scatt}}$ and $\boldsymbol{B}_{\text{scatt}}$, the scattered fields, have to satisfy

$$\boldsymbol{\nabla} \times \boldsymbol{E}_{\text{scatt}} = -\dot{\boldsymbol{B}}_{\text{scatt}} \tag{2.66a}$$

$$\boldsymbol{\nabla} \times \boldsymbol{B}_{\text{scatt}} = \mu_0 \left(\boldsymbol{j} + \varepsilon_0 \dot{\boldsymbol{E}}_{\text{scatt}} \right). \tag{2.66b}$$

These are the microscopic Maxwell equations with scattered instead of total fields. The incident waves do not have to be explicitly propagated on the numerical grid, as long as they satisfy Maxwell's equations in vacuum. Instead, they can be calculated analytically or numerically on lower dimensional auxiliary grids.

2.2.2. Particle representation on the PIC-level

Within the MicPIC framework, the field equations discussed above are coupled to the dynamics of the charged plasma particles via the electric current density **j**. The currents itself are determined by the plasma particle velocities, which are in turn driven by the electromagnetic fields, closing the self-consistent description. In order to establish this connection numerically, the particle shape needs to be linked to the discrete FDTD mesh. Typically, this is done via relatively simple weighting schemes, like the cloud-in-cell(CIC) scheme where particles are represented by a top-hat charge distribution [3]. This allows their mapping to the grid with relatively small numerical effort. However, these low order schemes suffer from strong force anisotropies, which precludes their use in MicPIC. The application of a gridless correction of the short range forces (the "Mic" force) requires a well defined, isotropic and low noise interparticle force on the PIC level.

In MicPIC this is achieved by utilizing a Gaussian shape function as originally proposed by Eastwood and Hockney [61] for an electrostatic description

$$S(x) = \left(\frac{1}{w_{\text{pic}} \sqrt{\pi}} \right) \exp\left(-\frac{x^2}{w_{\text{pic}}^2} \right), \tag{2.67}$$

satisfying the following normalization

$$\int_{-\infty}^{\infty} S(x) dx = 1. \tag{2.68}$$

The corresponding three dimensional representation then reads

$$S(x, y, z) = S(x) S(y) S(z). \tag{2.69}$$

Usually, the shape function is sampled onto the discrete numerical grid by calculating the amount of charge within or the amount of charge that travels into/out of the cells touched by the particle, respectively. For the low order weighting schemes mentioned above, the number of cells that are touched by the particle is well defined by the finite size of the particle distribution. However, the Gaussian shape function in principle extends to infinity, which means that a crucial property of the model, the charge conservation, strongly depends on the number of sampling points as well as the width of the Gaussian distribution. The charge conservation properties for Gaussian shape functions are shown in Figure 2.2 in terms of the relative charge error as a function of the particle width with respect to the grid spacing Δx. The curves shown in the figure have been obtained for 7 sampling points per space dimension[5], as this turned out to be sufficient for our calculations.

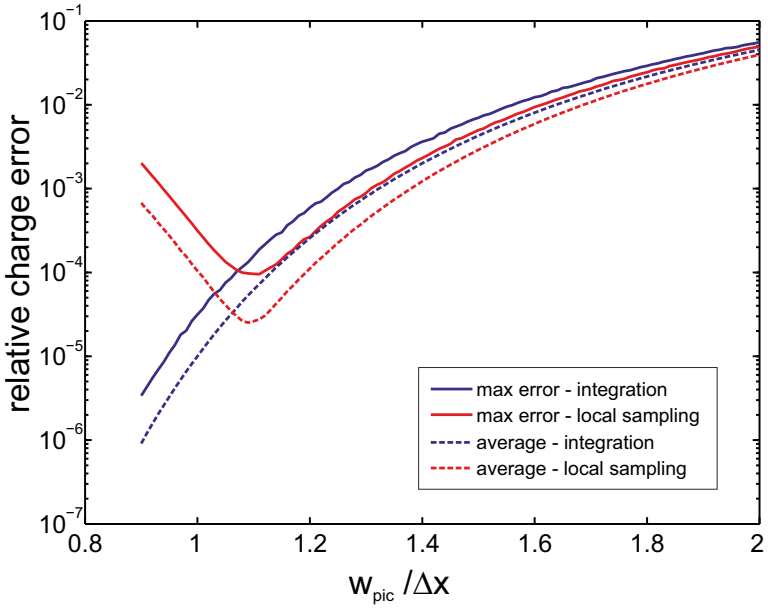

Figure 2.2.: Relative charge error for integral (blue) and local (red) sampling of the charge density onto the grid as a function of the relative Gaussian width $w_{pic}^{rel} = w_{pic}/\Delta x$. The maximal and average charge errors have been determined by evaluating a statistical ensemble of 10000 random positions of the particle center within a grid cell. Using 7 grid points per dimension for the local sampling yields an optimal Gauss width of $w_{pic}^{rel} = 1.12$ that on average conserves 99.9999% of the particle charge.

The different colors correspond to two different ways of sampling the Gaussians: (i) The blue curves show results, where the charge in every cell is calculated analytically and then summed up over all touched cells. Here, a decreasing particle size results in better charge conservation. Asymptotically, for infinitely small particle width all charge is contained in the center cell and the error vanishes. (ii) The red curves correspond to a much simpler method, where the charge density is sampled locally at each cell center and summed up afterwards. Surprisingly, this method results in even better charge conservation for particle sizes larger than roughly one cell, and shows

[5]Starting from the nearest cell center, the shape is sampled onto all grid points within ± 3 cells in each direction, resulting in a total number $7^3 = 343$ involved cells.

an optimal particle size of about 1.1 grid cells. For smaller particle sizes, the charge error increases again as most of the charge is confined to one cell, such that the local sampling is no longer describing a Gaussian shape.

Following this scheme, the charge and current density contributions from particle i at grid point $\mathbf{r}_g$ can be obtained from

$$\rho_i(\mathbf{r}_g) = q_i S(\mathbf{r}_i - \mathbf{r}_g) \quad \text{and} \quad \mathbf{j}_i(\mathbf{r}_g) = q_i \mathbf{v}_i S(\mathbf{r}_i - \mathbf{r}_g). \tag{2.70}$$

To ensure a self-consistent description of the particle dynamics on the PIC level, the electromagnetic PIC-fields acting on particle i have to be obtained in the same way as the current densities. The resulting effective electric and magnetic PIC fields are then given by the weighted average over all touched grid points g, using the same shape function and the same sampling method,

$$\boldsymbol{E}_i = \sum_g \boldsymbol{E}(\boldsymbol{r}_g) S(\boldsymbol{r}_i - \boldsymbol{r}_g) \quad \text{and} \quad \boldsymbol{B}_i = \sum_g \boldsymbol{B}(\boldsymbol{r}_g) S(\boldsymbol{r}_i - \boldsymbol{r}_g). \tag{2.71}$$

Together with the field propagation algorithm described in section 2.2.1 these expressions allow the calculation of the particle-particle forces on the PIC-level. Figure 2.3 shows the resulting forces in the electrostatic limit, i.e. for particles at rest, as a function of the particle separation. The black dotted and solid lines show the in-

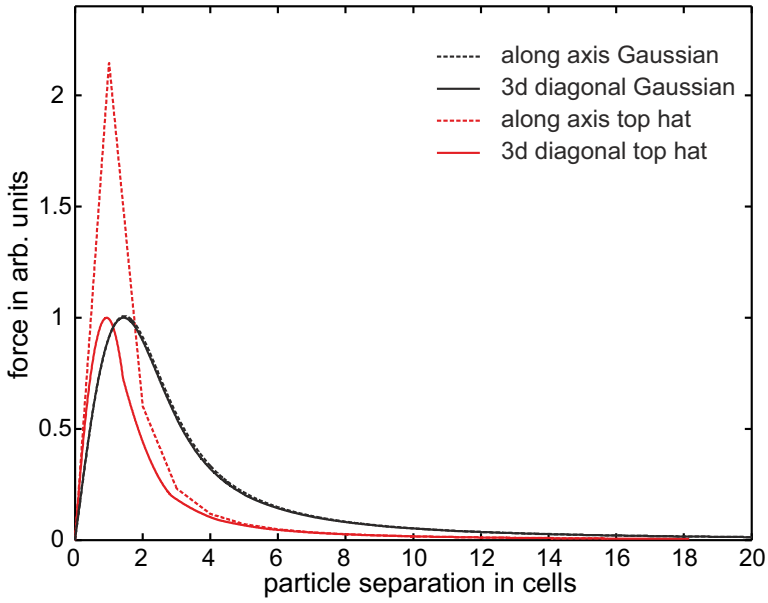

Figure 2.3.: Inter-particle forces on the PIC level, produced by Gaussian (black) and top-hat (red) distribution functions in the electrostatic limit (for particles at rest). The dotted lines correspond to particle trajectories along a natural grid axis and the solid lines to trajectories along the three dimensional grid diagonal. While the top-hat shape function result in strongly anisotropic forces, the Gaussian profiles show only negligible anisotropy. Note that, these data have been kindly provided by Charles Varin from the University of Ottawa (who did his own implementation of the MicPIC approach), since top-hat distributions are not considered in my implementation.

teraction forces for particle trajectories along a natural grid axis and along the three

dimensional grid diagonal, respectively. For comparison, also the corresponding forces for top-hat distributions are shown in red. The Gaussian shape functions result in negligible force anisotropy, which is essential for the application of the force decomposition scheme. In contrast to that, the top-hat distributions show strongly anisotropic forces, which proves that they are not suited for the MicPIC scheme.

2.2.3. Local Correction

Due to the short-range nature of the microscopic correction $\mathbf{f}_i^{\mathrm{mic}}$, the corresponding binary forces need to be evaluated only for a small subsets of the total particle ensemble. In MicPIC this local correction is done in a similar way as in a molecular dynamics code with short-range binary interactions. The binary correction forces given by equation (2.17) are evaluated for each plasma particle within a sphere with finite cut-off radius r_{cut} around its particle center $\mathbf{r}_i$.

Local correction and cut-off radius

The cutoff radius r_{cut} is one of the key parameters in MicPIC as it determines both, the accuracy as well as the numerical workload of the microscopic correction. In order to pick a reasonable value for r_{cut}, the corresponding force error introduced by the finite cutoff radius has to be estimated. Figure 2.4 shows the force composition (total, PIC and microscopic) for the idealized example of two point-like plasma particles ($w_0 \to 0$) at rest as a function of their separation in units of the pic particle size w_{pic}.

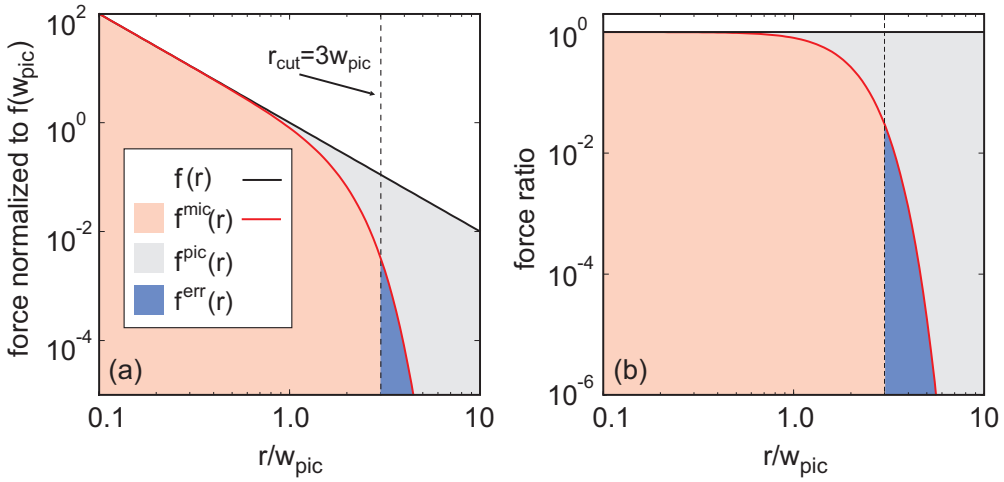

Figure 2.4.: MicPIC force decomposition for two interacting point charges vs. inter-particle distance. (a) Black curve: total force $f(r)$ normalized to the force at $f(r = w_{\mathrm{pic}})$; red line: Mic force f_{mic}; gray area: PIC force contribution f_{PIC}; red and blue shaded areas: microscopic force contribution for radii below and above a cutoff radius $r_{\mathrm{cut}} = 3w_{\mathrm{pic}}$, respectively. (b) Forces in (a) are normalized to $f(r)$, hence the total force becomes $f(r) = f(r) = 1$ (black curve); red curve: $f_{\mathrm{mic}}(r) = f(r)$. As f_{mic} is neglected for $r > rcut$, the red and blue shaded areas denote the parts of the relative microscopic force correction that are included and neglected, respectively. The grey area gives the relative PIC contribution. Published in [62].

The black and red curves in figure 2.4a correspond to the total and microscopic forces according to equation (2.19), normalized to the force at $f(r = w_{\mathrm{pic}})$. The gray area denotes the contribution from the PIC term, which has only an electrostatic component as the particles are at rest. The red and blue areas show the contributions from the microscopic force for distances below and above $r_{cut} = 3w_{\mathrm{pic}}$. The fact that Mic and PIC forces dominate for either $r < w_{\mathrm{pic}}$ or $r > w_{\mathrm{pic}}$ nicely illustrates the main idea behind the MicPIC force decomposition.

For easier evaluation of the respective contributions of Mic and PIC forces, they are normalized to the total force $f(r)$ in the right panel of figure 2.4. Considering a cutoff radius of $r_{cut} = 3w_{pic}$, the red and blue areas show the part of the microscopic correction that is taken into account or neglected. The relative error drops rapidly with increasing r_{cut}, e.g. more than one order of magnitude when increasing it from $3w_{\mathrm{pic}}$ to $4w_{\mathrm{pic}}$. However, this would also lead to approximately twice the numerical workload due to the higher number of particles in the correction sphere. The experience of operating MicPIC for the last years has shown that a cutoff radius of $r_{cut} = 3w_{pic}$ is sufficient for most calculations.

Cell-indexing

Theoretically, the numerical workload connected with the local correction scales linearly with the total number of plasma particles N, as the binary forces for every particle i have to be evaluated only for a subset of all other particles, namely the ones within its correction sphere (on average M particles). However, to identify these particles, their distance to each other particle has to be determined, which would, if directly evaluated for all N particles, result in a N^2 operation. To sustain the linear scaling, MicPIC makes use of the cell indexing scheme introduced by Allen *et al.* [63] in 1989. The key idea behind this scheme is to assign all particles to an auxiliary grid that allows to backtrack the number and indices of all particles in a specific cell. This way, only particles in the neighboring cells have to be touched. A sketch of the cell indexing procedure is given in figure 2.5.

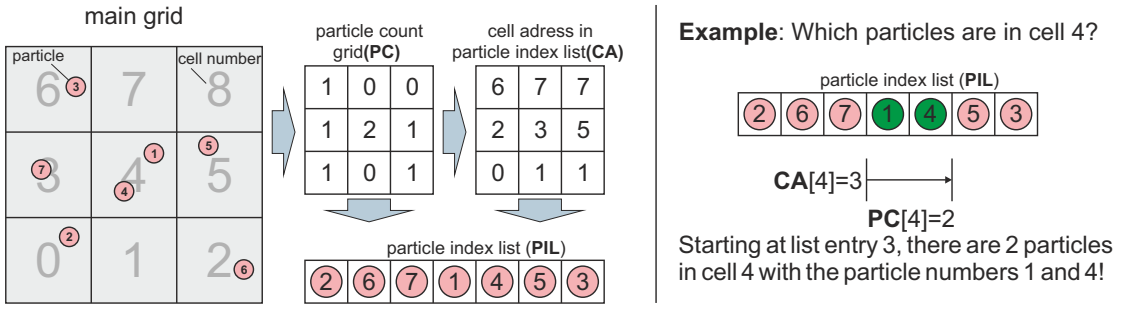

Figure 2.5.: Sketch of the cell indexing procedure. All particles are assigned to cells in the main computational grid with the help of auxiliary grids. A detailed description of the complete procedure can be found in the text. The right part shows how the indices of particles located in a specific cell can be retrieved with this method.

In a first step, an auxiliary grid **PC** (particle count) is created, where the total

number of particles in each cell is stored. This action requires a single loop through all particle positions. Next, a second auxiliary grid **CA** (cell address) is created, where each cell contains the number of particles in all previous cells[6]. Finally, a particle index list (**PIL**) is created, where every particle index (i.e. its position in the main particle list indicated by the numbers in red circles) is stored in the order of their position in the main grid. This requires a second loop through the particle list.

How the indices of all particles contained in a specific cell can be retrieved from these auxiliary grids is shown for an example in the right part of figure 2.5. First, one has to find the corresponding cell address in the auxiliary particle list (**PIL**) from the cell address grid **CA**. Next, the number of particles contained in this cell N_c is given by the corresponding entry in the particle count grid (**PC**). The wanted N_c particle indices can then be found in the auxiliary particle list **PIL**, starting with the position given by **CA**.

2.2.4. Particle propagation

In the final step of the MicPIC propagation scheme, the particles positions and velocities need to be advanced in time according to the electromagnetic fields acting on them. To propagate the particle positions, a simple finite difference expression according to

$$\mathbf{r}^n = \mathbf{r}^{n-1} + \dot{\mathbf{r}}^{n-\frac{1}{2}}\Delta t. \tag{2.72}$$

can be applied. Advancing the particle velocities on the basis of the Lorentz force is more complicated as it involves a rotation. A very efficient and accurate method to achieve this has been introduced by J.P. Boris in 1970 [64] and is now briefly discussed.

Boris-Scheme

The basis of the Boris scheme is a centered finite differences expression of the Lorentz force, which is given by

$$\frac{\dot{\mathbf{r}}^{n+\frac{1}{2}} - \dot{\mathbf{r}}^{n-\frac{1}{2}}}{\Delta t} = \frac{q}{m}(\mathbf{E}^n + \frac{\dot{\mathbf{r}}^{n+\frac{1}{2}} + \dot{\mathbf{r}}^{n-\frac{1}{2}}}{2} \times \mathbf{B}^n). \tag{2.73}$$

From this expression, the main challenge in the particle propagation with electric and magnetic fields becomes already evident. Equation (2.73) only gives an implicit expression for the new particle velocity $\dot{\mathbf{r}}^{n+\frac{1}{2}}$. Solving these implicit equations is not impossible but rather complicated and involves a significant amount of calculation [65], which is not convenient if millions of particles have to be propagated in each time step. However, J. P. Boris found an elegant way to derive explicit expressions for the velocities by separating the electric and magnetic forces. Substituting

$$\dot{\mathbf{r}}^{n-\frac{1}{2}} = \mathbf{v}_- - \alpha\mathbf{E}^n \tag{2.74}$$

$$\dot{\mathbf{r}}^{n+\frac{1}{2}} = \mathbf{v}_+ + \alpha\mathbf{E}^n \tag{2.75}$$

[6] This corresponds to the accumulative sum of **PC**.

into equation (2.73) yields an expression where $\mathbf{E}^n$ cancels out

$$\mathbf{v}_+ - \mathbf{v}_- = \alpha\,(\mathbf{v}_+ + \mathbf{v}_-) \times \mathbf{B}^n \tag{2.76}$$

with $\alpha = \frac{q}{m}\frac{\Delta t}{2}$. Further, substituting $\mathbf{t} = \alpha\mathbf{B}^n$ leaves a compact expression that describes a rotation

$$\mathbf{v}_+ = \mathbf{v}_- + (\mathbf{v}_+ + \mathbf{v}_-) \times \mathbf{t}^n. \tag{2.77}$$

Together, equations (2.74), (2.75) and (2.77) describe a three step process: First, half of the electric impulse is added to the old velocity, then the intermediate velocity is rotated and finally the second half of the electric impulse is added.

Yet, the expression for the rotation is still implicit. To retrieve an explicit expression, an additional vector $\mathbf{v}'$ is introduced that corresponds to only a partial rotation from that given in equation (2.77)

$$\mathbf{v}' = \mathbf{v}_- + \mathbf{v}_- \times \mathbf{t}. \tag{2.78}$$

Evaluation of the cross product with $\mathbf{t}$ yields the following two expressions

$$\begin{aligned} \left(\mathbf{v}' \times \mathbf{t}\right) &= (\mathbf{v}_- \times \mathbf{t}) - |\mathbf{t}|^2\,\mathbf{v}_- + (\mathbf{v}_- \cdot \mathbf{t}) \cdot \mathbf{t} && (2.79)\\ &= (\mathbf{v}_+ \times \mathbf{t}) + |\mathbf{t}|^2\,\mathbf{v}_+ - (\mathbf{v}_+ \cdot \mathbf{t}) \cdot \mathbf{t} && (2.80) \end{aligned}$$

Finally, subtracting these equations yields the desired explicit expression for the full rotation, which is then given by

$$\mathbf{v}_+ = \mathbf{v}_- + \left(\mathbf{v}' \times \mathbf{s}\right) \quad \text{with} \quad \mathbf{s} = \frac{2\mathbf{t}}{1+t^2}. \tag{2.81}$$

The complete explicit propagation scheme for the particle velocities is now given by the following set of equations:

$$\begin{aligned} \mathbf{v}_- &= \dot{\mathbf{r}}^{n-\frac{1}{2}} + \alpha\mathbf{E}^n && (2.82)\\ \mathbf{v}_+ &= \mathbf{v}_- + [(\mathbf{v}_- + (\mathbf{v}_- \times \mathbf{t})) \times \mathbf{s}] && (2.83)\\ \dot{\mathbf{r}}^{n+\frac{1}{2}} &= \mathbf{v}_+ + \alpha\mathbf{E}^n && (2.84) \end{aligned}$$

2.2.5. Implementation of ionization

The numerical details discussed so far complete the main part of MicPIC that is necessary to model the classical laser driven dynamics of a plasma. In order to enable MicPIC to also describe the plasma formation process, atomic ionization mechanisms have to be implemented. This section briefly reviews the corresponding atomic models and shows how they can be modified to be applicable to many particle systems.

Tunnel ionization

When exposed to strong electric fields, bound electrons have a nonzero probability to tunnel through the generated potential barrier. The corresponding tunnel rate for an atom can be calculated quantum-mechanically. In 1986 M.V. Ammosov, N.B. Delone

und V.P. Krainov published analytic expressions for atomic tunnel rates in varying electromagnetic fields, the so called ADK rates [66]. In atomic units the rates read

$$W_{\mathrm{ADK}}^{\mathrm{au}} = I_p^{\mathrm{au}} C_{n^*l^*}^2 A_{lm} \left(\frac{2\kappa^3}{\mathcal{E}^{\mathrm{au}}}\right)^{2n^*-|m|-1} \exp(-\frac{2\kappa^3}{3\mathcal{E}^{\mathrm{au}}}) \tag{2.85}$$

with

$$A_{lm} = \frac{(2l+1)(l+|m|)!}{2^{|m|}(|m|)!(l-|m|)!} \quad , \quad \kappa = \sqrt{2I_P^{\mathrm{au}}} \tag{2.86}$$

and

$$C_{n^*l^*}^2 = \frac{2^{2n^*}}{n^*\Gamma(n^*+l^*+1)\Gamma(n^*-l^*)} \quad , \quad n^* = Z/\kappa \quad , \quad l^* = n^* - 1 \,, \tag{2.87}$$

where I_P^{au} is the ionization potential[1] and $\mathcal{E}^{\mathrm{au}}$ is the electric field strength, Z the resulting charge state of the ion and m and l the magnetic and angular momentum quantum number, respectively. The auxiliary parameters l^* and m^* are referred to as effective quantum numbers. The resulting tunneling rates exhibit an extreme nonlinear intensity dependence, e.g. rising by almost 10 orders of magnitude when increasing the laser intensity from $I = 1 \times 10^{13}$ W/cm^2 to $I = 1 \times 10^{14}$ W/cm^2 in the case of initially neutral Xenon atoms.

In MicPIC, to take many particle effects into account, these rates are evaluated for the total electric fields on the PIC level, i.e. the sum of the laser field and the fields created by all other charged particles. The microscopic fields associated with the local correction are neglected to avoid double counting of electrons with trajectories close to atoms or ions, which is already accounted for in the electron-impact-ionization.

Electron-Impact-Ionization

In MicPIC the treatment of electron-impact ionization, i.e. the liberation of secondary electrons as a result of inelastic electron-atom/ion collisions, is restricted to sequential ionization

$$\mathrm{X}^{j+} + e \rightarrow \mathrm{X}^{(j+1)+} + 2\,e \tag{2.88}$$

while non-sequential ionization or ionization via excited intermediate states is so far neglected. In contrast to the typical treatment of impact ionization in PIC codes, these inelastic collisions are not evaluated via rates and Monte Carlo schemes. In MicPIC, the microscopic character of this ionization mechanism is effectively preserved, i.e. every electron-ion collision is checked for ionization using impact ionization cross sections.

Since there are no appropriate microscopic theories for the calculation of impact ionization cross sections available, the well known parameterized empiric formula introduced by Wolfgang Lotz [68] is utilized

$$\sigma_j(E) = \sum_i a_i q_i \frac{\ln(E/P_i)}{EP_i} \left\{1 - b_i \exp\left[-c_i(E/P_i - 1)\right]\right\} \quad , \quad E \geq P_i, \tag{2.89}$$

[1] I_P^{au} - The corresponding values used in MicPIC have been calculated with the relativistic Dirac-LDA code from [67]

where E is the kinetic energy of the impinging electron, P_i the ionization potential of the i-th electronic shell, q_i the number of electrons in the i-th shell and a_i, b_i and c_i are empiric parameters. With these parameters the calculated cross sections can be fitted to experimental data over a wide range of elements, charge states and projectile energies [69–73].

Here, many particle effects are accounted for in terms of effective ionization potentials. For an atomic ion within a plasma environment, neighboring ions and electronic screening by quasifree plasma electrons lead to an effective ionization threshold $E^*_{nl} = E_{nl} - \Delta_{env}$. The pure atomic value E_{nl} is lowered by an environmental shift Δ_{env}. While E_{nl} corresponds to the energy that is needed to completely remove an electron with principal and angular quantum numbers n and l from the atom, E^*_{nl} specifies the corresponding minimal energy that is required to lift the electron into the quasi-continuum within the plasma environment. The shift Δ_{env} is evaluated directly from the plasma fields in the simulation, following the scheme in [24].

However, using effective ionization potentials $P^*_i = P_i - \Delta_{env}$ leads to a continuous spectrum of ionization potentials, which makes an adaptation of the parameters a_i, b_i and c_i to specific charge states impractical. Therefore a simplified version of equation (2.89) is used

$$\sigma_j(E) = \sum_i a q_i \frac{\ln(E/P^*_i)}{E P^*_i}, \qquad E \geq P^*_i, \tag{2.90}$$

with the fixed parameter $a = 450 \times 10^{-16}$ cm^2(eV)^2, which satisfactorily reproduces experimental data [74].

Photoionization

Realizing a self-consistent treatment of the single photon ionization process in the PIC-framework is a non-trivial task, as the energy of the absorbed photon has to be removed from the incident laser field. At the moment of writing this thesis there exists no standard method to accomplish this goal. An approach that permits a consistent description of photoionization based on a dissipative harmonic oscillator model for bound electrons is discussed in Chapter 5 in detail.

2.2.6. MicPIC parameters and scaling

In the discussion of the numerical implementation of the MicPIC approach above, a number of simulation parameters has been introduced. A list of the main simulation parameters and their meaning is given in table 2.1 as a reminder. This section discusses how to choose the values of these parameters in an optimal way under existing physical and technical constraints. Additionally, also their influence on the performance of the code is discussed in terms of a general scaling analysis.

First, the cell width on the PIC level Δx determines the resolution of wave propagation phenomena on the numerical grid. It has to be chosen small enough to resolve all relevant scales of the radiated fields, i.e. the skin-depth and the wavelength of the laser as well as possibly generated higher harmonics. Typically, a grid spacing of $\Delta x \leq \lambda/20$

parameter	description
Δx	cell width on FDTD grid
Δt	time step
w_{pic}	particle width on PIC-level
r_{cut}	cutoff radius for local correction
w_0	actual particle width

Table 2.1.: List of the main simulation parameters.

is sufficient for that task, which leads to values of a few to a few ten nanometers in the optical excitation regime. To ensure convergence of the corresponding FDTD solution, the time step has to fulfill the Courant stability criterion, which imposes an upper limit onto the time step according to $\Delta t \leq \Delta x/(\sqrt{3}c)$ [60], with c being the vacuum speed of light.

Further, the particle width on the PIC level has to fulfill $w_{\mathrm{pic}} \approx 1.1\Delta x$ for optimal charge conservation properties (see section 2.2.2). Next, to ensure an accurate evaluation of the microscopic correction (Sec. 2.2.3) the cutoff radius r_{cut} has to be in the range of $r_{cut} \approx 3w_{pic}$. Finally, the actual particle width has to be chosen such, that classical electron recombination below quantum-mechanical energy levels is precluded, i.e. the classical binding energy resulting from equation (2.16) has to be smaller or equal to the quantum mechanical energy levels used for ionization.

In summary, choosing a grid resolution compatible with the upper limit given by the relevant scales of the radiated fields, determines every other major parameter, except for the actual particle width. As smaller values of Δx leave the physics unchanged, this freedom can be utilized to balance the numerical work load between the microscopic and PIC parts of the code.

To evaluate how this influences the performance of the code, a scaling analysis is performed under the assumption that the excitation of a system with the total particle number N by an external laser of wavelength λ has to be modeled in a simulation volume V. The workload associated with the microscopic correction is then determined by the total number of particles N times the number of particles within the correction sphere $M = (4\pi/3)\, r_{cut}^3 N/V$ (see figure 2.6). As a result, advancing the microscopic part one time step scales as $O_{\mathrm{step}}^{\mathrm{mic}} = \alpha N(N/V)r_{\mathrm{cut}}^3$. Advancing the PIC part one time step requires the calculation of the currents and forces for all particles, which scales with the particle number N, and the update of the electromagnetic fields, which scales with the number of grid points, $V/(\Delta x)^3$. Together this results in a scaling of the PIC part given by $O_{\mathrm{step}}^{\mathrm{pic}} = \beta N + \gamma V/(\Delta x)^3$. Putting both together yields the total workload scaling for one time step

$$O_{\mathrm{step}}^{\mathrm{MicPIC}} = \alpha N(N/V)r_{\mathrm{cut}}^3 + \beta N + \gamma V/(\Delta x)^3 \tag{2.91}$$

where the parameters α, β and γ are prefactors corresponding to the microscopic correction, current/force calculation, and the field update respectively. Exploiting the fact that $\Delta x \simeq w_{\mathrm{pic}} \propto r_{\mathrm{cut}}$ and assuming a constant particle density ($N/V = const.$)

allows to rewrite expression (2.91) in terms of the cutoff radius

$$O_{\text{step}}^{\text{MicPIC}} = \alpha' N r_{\text{cut}}^3 + \beta' N + \gamma' N / r_{\text{cut}}^3 \tag{2.92}$$

where the parameters α', β' and γ' are modified prefactors. Eventually, MicPIC will be used to model the plasma dynamics for certain time intervals, i.e. the quantity of interest is the workload per unit time. The corresponding translation of the above result can be done by dividing it by $\Delta t \propto r_{cut}$ and yields

$$O^{\text{MicPIC}}(N, r_{\text{cut}}) = N(\underbrace{\alpha' r_{\text{cut}}^2}_{\text{Mic}} + \underbrace{\beta'/r_{\text{cut}} + \gamma'/r_{\text{cut}}^4}_{\text{PIC}}). \tag{2.93}$$

This shows that MicPIC scales linearly with the total particle number N as desired. The workload distribution 6between Mic and PIC part can be balanced by choosing the cutoff radius (or equivalently the grid spacing Δx) within its physical constraints. For very small/large values of r_{cut} dominant load is produced on the PIC or Mic parts. In the limiting case where r_{cut} approaches the box length $V^{1/3}$ all particles need to be corrected, the time step is no longer bound to the grid spacing and equation (2.93) yields the well known $O(N) = N^2$ scaling associated with molecular dynamics codes.

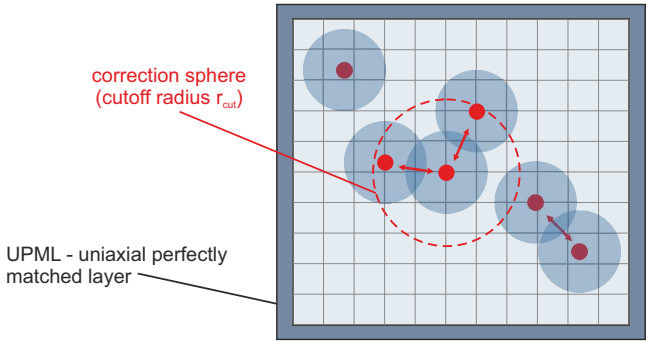

Figure 2.6: Illustration of the local correction scheme. Only interactions for particles within a finite cutoff radius have to be correctd.

2.2.7. MicPIC system energy calculation

An important observable for the evaluation of MicPIC calculations is the energy absorption by the system contained in the numerical box. It is given by the total energy difference before and after laser excitation. The total box energy reads

$$\begin{aligned} E_{\text{tot}} \;=\; & \underbrace{\sum_i \frac{m_i}{2}\dot{\mathbf{r}}_i^2}_{\text{kinetic}} + \underbrace{\frac{1}{2}\int \left[\varepsilon_0 (\mathbf{E}^{\text{pic}})^2 + \frac{1}{\mu_0}(\mathbf{B}^{\text{pic}})^2\right] d^3 r}_{\text{EM-energy on PIC grid}} \\ & + \underbrace{\sum_{i<j} V_{ij}^{\text{mic}}(r_{ij})}_{\text{micr. correction}} - \underbrace{\frac{1}{2}\sum_i V_{ii}(0, w_{\text{pic}})}_{\text{self energy on PIC grid}}, \end{aligned} \tag{2.94}$$

where the individual terms describe the kinetic energy, the electromagnetic energy on the PIC-level, the energy resulting from the microscopic correction, and the energy renormalization to remove the spurious self energy of the particles on the PIC grid (as indicated).

3. Validating MicPIC

From a theoretical point of view, MicPIC provides a self-consistent description of classical laser-plasma interactions with microscopic resolution and explicit electromagnetic field evolution. This opens up new capabilities like the numerical treatment of strongly coupled plasmas in a size regime where electromagnetic field propagation strongly affects its dynamics. However, before MicPIC's full potential can be utilized to enter so far numerically inaccessible terrain, it is necessary to validate the approach and its implementation. Ideally, such benchmarking should be done by comparison with well established models. As the MicPIC approach itself is new and our implementation is (to the best of my knowledge) the only currently existing one, there is no convenient single reference model available that can cover the whole range of applicability. As a result, MicPIC has to be validated in steps via appropriately chosen reference scenarios that are accessible with established models.

First, MicPIC's capability to describe strongly-coupled plasma dynamics including ionization is demonstrated in section 3.1 for small Argon clusters ($R = 5\,\mathrm{nm}$). In this size regime, the classical plasma dynamics is perfectly described by molecular dynamics simulations, which allows for direct comparison of MicPIC and MD results. The observed agreement validates the correct treatment of atomic scale collisions in MicPIC.

Second, the description of field propagation in MicPIC is tested in section 3.2. For this purpose, the absorption and scattering efficiencies of pre-ionized metal-like clusters, excited at the plasmon resonance, have been studied systematically as function of cluster radius. The employed low intensity of the excitation pulse ensures a linear response of the system, justifying the comparison with linear continuum models like Mie-theory, where the material properties are described in terms of a parametric dielectric function. The comparison of the radius-dependent absorption and scattering predicted by microscopic and continuum models validates MicPIC and reveals the breakdown of the electrostatic description for system sizes of $R \gtrsim 20\,\mathrm{nm}$ at $800\,\mathrm{nm}$ excitation wavelength.

Finally, the comparison of microscopic and macroscopic models in section 3.2 yields a set of material parameters that quantifies the effect of microscopic processes in continuum models. These parameters are usually hard to come by for nanosystems and are thus a major result in itself. In Sec. 3.3, these parameters are used to study the relative importance of surface and bulk effects as function of cluster size.

Note that the results presented in this section have been already published in [62] and [75], where the method has been officially introduced. The discussion given here follows closely the original publications, with a more detailed discussion when appropriate.

3.1. Nanoplasma formation in small rare-gas clusters

The purpose of the first benchmark calculations is the demonstration of MicPIC's capability to describe the full classical plasma dynamics including plasma formation via ionization. Therefore, the interaction of an initially neutral rare-gas cluster with an intense near-infrared (NIR) laser field is studied. A spherical Argon cluster with 5 nm radius, consisting of N=11100 atoms, with fcc-structure and atomic Wigner-Seitz radius $r_s = 2.21\,\text{Å}$ is considered as the model system. For cluster excitation a 25 fs laser pulse with a peak intensity of $1 \times 10^{15}\,\text{Wcm}^{-2}$ at a wavelength of $\lambda = 800\,\text{nm}$ is applied. Liberation of bound electrons is considered in terms of tunnel- and electron impact ionization, as these are the dominant ionization channels for the given laser parameters. According to equation (2.16) the numerical binding energy of electrons scales linearly with the charge state of the ion. To prevent classical recombination of liberated electrons below the quantum mechanical energy levels for all ion charge states, the width parameter w_0 of the Gaussian MicPIC particles is chosen to be $w_0 = 0.81\,\text{Å}$, which corresponds to a binding energy of $E_B = 14.2\,\text{eV}$ for singly charged ions. Since propagation effects are negligible for this cluster size, the MicPIC results can be directly compared to MD calculations[1]. Figure 3.1 shows the time evolution of selected observables as predicted by MicPIC and MD. The demonstrated excellent agreement validates the microscopic part of MicPIC and the implementation of the ionization dynamics.

When concentrating on the physics of this benchmark scenario, the following conclusions can be drawn. First, the plasma formation starts with tunnel ionization in the leading edge of the laser pulse (see Fig. 3.1.c). The observed distinct threshold behavior reflects the high non-linearity of the tunnel ionization rate as function of intensity (see Section 2.2.5). The ignition due to tunnel ionization, however, produces only a few electrons. The heating of these electrons in the laser field subsequently drives an impact ionization avalanche, which rapidly produces a highly overdense nanoplasma (about 60 times overcritical[2], see Fig.3.1.b,c). Eventually, electron impact ionization is by far the dominating ionization channel (about 90% of the ionization events). Because of the overcritical nature of the plasma, the external laser field is efficiently screened by the cluster electrons. Heating due to inverse Bremsstrahlung is therefore expected to proceed mainly at the cluster surface. During the pulse, the nanoplasma electrons are heated moderately, leading to an electron temperature of about 20 eV at the end of the pulse.

The high electron density combined with the moderate temperature results in a strongly coupled nanoplasma. The evolution of the coupling is indicated in figure 3.1.d in terms of the Debye number

$$N_\text{D} = \frac{4\pi}{3} n_e \lambda_d^3 \tag{3.1}$$

[1] In the MD code utilized here [24], plasma particles are represented by the same Gaussian charge distributions as in MicPIC. In contrast to MicPIC the electrostatic fields obtained from these distributions are used throughout the total simulation volume.

[2] The critical density is given by $n_\text{crit} = m_\text{e}\varepsilon_0{\omega_\text{las}}^2/e^2$ and determines the density where the corresponding plasma frequency is equal to the frequency of the exciting laser.

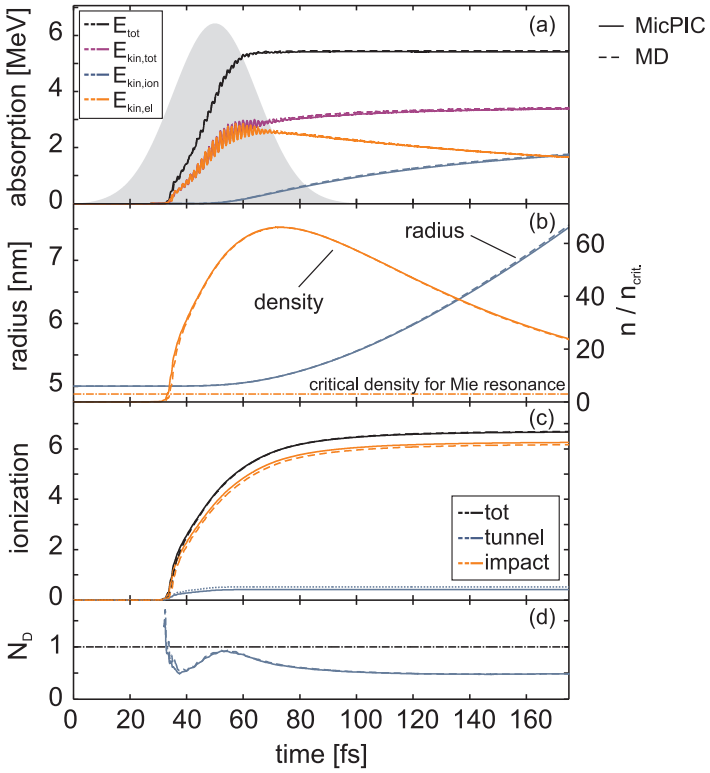

Figure 3.1.: Time evolution of Ar_N (N = 11100) under a 25 fs laser pulse (800 nm) at intensity of 10^{15} Wcm^{-2} including ionization and starting from the neutral cluster ground state as calculated with MicPIC (solid) and MD (dashed); (a) kinetic and absorbed energies, (b) cluster radius extracted from the ionic rms radius and charge density in units of the critical density, (c) inner ionization with contributions from tunnel and impact ionization and (d) Debye number. Note that MicPIC and MD results show excellent agreement with deviations of the order of the linewidth. In panel (a), E_{tot}, $E_{\mathrm{kin,tot}}$, $E_{\mathrm{kin,ion}}$ and $E_{\mathrm{kin,el}}$ denote the total absorption of the cluster, the total kinetic energy, the ion kinetic energy and the electron kinetic energy, respectively. Published in [75].

where n_e and λ_d are the electron density and the Debye screening length. The Debye number quantifies the average number of electrons within the Debye sphere and indicates strong coupling for $N_{\mathrm{D}} \lesssim 1$ [3]. The calculated evolution shows that a strongly coupled plasma is formed shortly after the initial ionization and persists for the rest of the dynamical evolution. This means that for a correct description of the observed plasma dynamics, a fully correlated treatment of the microscopic collisions is required.

Focusing on the ion dynamics, the following observations can be made. Cluster expansion begins near the pulse peak and is mainly driven by hydrodynamic expansion, i.e. the energy conversion of electron thermal energy into ion kinetic energy via adiabatic expansion cooling, cf. figures 3.1.a,b. However, the fact that the total kinetic energy (electrons and ions) is increasing even after energy absorption has essentially stopped shows that also Coulomb repulsion due to outer cluster ionization (Coulomb explosion) and charge spill-out at the surface contributes to the expansion. The cluster

[3]The concept of Debye screening as a linear screening theory breaks down for strong coupling and is used here for the identification of the coupling regime only.

expansion efficiently lowers the nanoplasma density, which is about 20 times overcritical at the end of the simulation.

The excellent overall agreement of the MicPIC calculations with MD results demonstrates that MicPIC correctly accounts for microscopic processes, e.g. ionization and collisions, and is capable to efficiently model strongly coupled nanoplasmas.

3.2. Linear-response dynamics for small and large clusters

In order to proof that MicPIC accounts correctly for field propagation effects, like radiation damping and field attenuation, the size of the considered model systems needs to be increased to a regime where these processes begin to play a role. To validate the corresponding MicPIC results in the regime of large clusters, they are compared to Mie-theory, as it fully accounts for field propagation effects in linear response. For small systems, where field propagation effects are negligible, the results can be compared to the respective electrostatic limits of MicPIC and Mie theory, i.e. MD and nanoplasma theory. To enable a meaningful comparison of the MicPIC results with continuum theory, the calculations are interpreted and compared in terms of the corresponding size dependent absorption and scattering cross sections.

As model systems homogeneous spherical droplets with one conduction electron per ion are considered. The electrons are initialized with an electron temperature of $T_\mathrm{e} = 5\,\mathrm{eV}$. Further ionization of bound atomic electrons is disregarded. The ions are positioned in a face-centered cubic (fcc) lattice structure with an ionic Wigner-Seitz radius of $r_\mathrm{s} = 3.6\,\text{Å}$. The resulting cluster has an electron density of $n_e = 5.1 \times 10^{21}\,\mathrm{cm}^{-3}$, with a corresponding skin depth of $73.5\,\mathrm{nm}$[4]. For laser excitation a $7\,\mathrm{fs}$ laser pulse with a near-infrared laser wavelength of $800\,\mathrm{nm}$ has been chosen that drives the Mie plasmon resonantly. To restrict the excitation to the linear response regime, a moderate laser intensity of $6 \times 10^{11}\,\mathrm{W/cm^2}$ is applied.

For clarity, the interpretation of the analysis is divided into two parts. In the first part, the calculated time evolution of the dynamics is discussed and compared to MD results for a small and a large cluster system. In the second part, a systematic analysis of the size dependent absorption and scattering efficiencies is provided.

3.2.1. Cluster dynamics in the linear response regime

The time evolution of selected observables, as predicted by MD and MicPIC simulations, is displayed in figure 3.2 for a small ($R = 10\,\mathrm{nm}$) and a larger ($R = 30\,\mathrm{nm}$) cluster. Both the small and large cluster results show the excitation of pronounced dipole oscillations of the cluster electrons. The resonant nature of the excitation is evident from the fact that the dipole amplitude increases even after the pulse peak. The

[4]The plasma skin depth determines the depth to which electromagnetic radiation can penetrate into the plasma. It is given by c/ω_pe, where c is the vacuum speed of light and ω_pe the electron plasma frequency.

eventual decay of the oscillations reflects the damping of the collective electron motion via electron-ion and electron-surface collisions as well as radiation damping. While collisional damping converts energy from the collective motion into thermal nanoplasma energy, part of the collective excitation energy is removed from the system via the re-emission of light. Signatures of both effects can be found in figure 3.2.

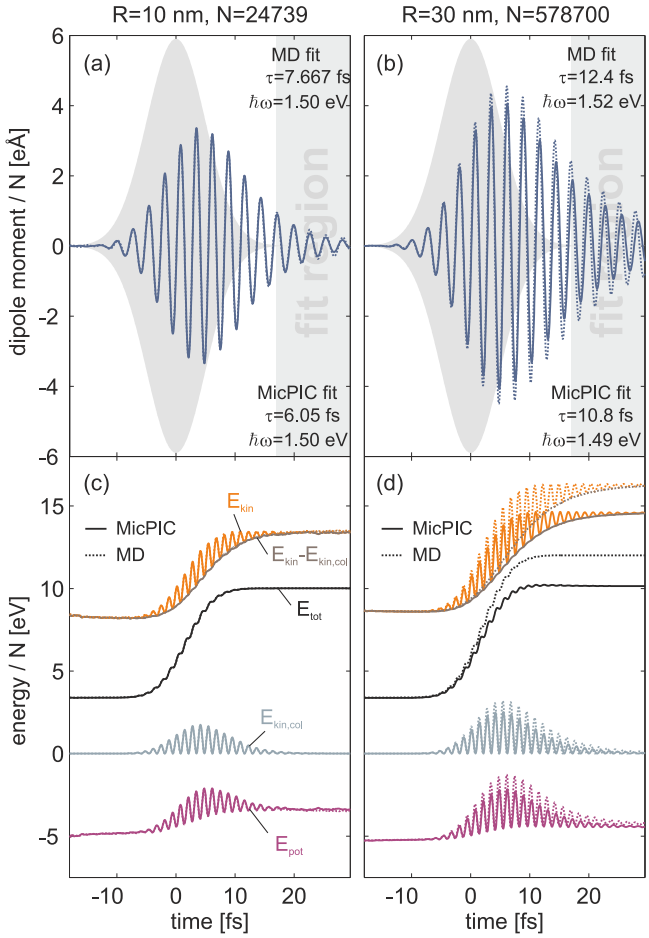

Figure 3.2.: Time evolution of dipole moments (a, b) and energies (c, d) for resonant excitation of 10 nm (left column) and 30 nm (right column) clusters in the linear response regime ($I = 6 \times 10^{11}\,\mathrm{W\,cm^{-2}}$) as calculated with MicPIC (solid lines) and MD (dashed lines). In the bottom panels, E_{kin}, E_{pot} and E_{tot} denote the total kinetic energy, the potential energy and the total energy of the cluster, respectively. $E_{\mathrm{kin,col}}$ shows the kinetic energy of the center of mass motion of the electron cloud. For better comparability all data are normalized to the number of electrons N. The given plasmon energies and lifetimes are the results from fitting a damped harmonic oscillator to the decaying dipole moments (fit regions as indicated). Published in [75].

The conversion of collective excitation energy into heat can be extracted directly from the decay of the periodic reciprocal transformation of potential and kinetic energies. The blue curves in figures 3.2c and d show the kinetic energy associated with the collective center-of-mass motion of the electron cloud which is periodically converted into potential energy and vice versa. As thermalization by collisions takes place, this process decays and the energy stored in the collective motion is converted to heat. Once

thermalization is completed, the collective directed motion dies out and the thermal electron kinetic energy (total kinetic energy reduced by the collective contributions, $E_{\mathrm{kin}} - E_{\mathrm{kin,col}}$) matches the total kinetic energy, cf. figures 3.2c and 3.2d.

The increasing importance of radiation effects with increasing system size is revealed by the comparison of the $R = 10\,\mathrm{nm}$ and 30 nm calculations. While the dipole signals and energies calculated by MD and MicPIC are in almost perfect agreement for the 10 nm system, they substantially differ for the larger 30 nm cluster. The total cluster energy after the laser pulse is higher for MD, which can be attributed to the fact that MD neglects field attenuation due to the skin effect. As the cluster diameter is comparable to the skin depth this is already important. The most obvious difference in the dipole amplitude is the faster decay of the signal. To better quantify the differences, the dipole signal has been fitted to a damped harmonic oscillator after the laser pulse

$$D = D_0\, cos(\omega t + \phi)\, e^{-t/\tau}, \tag{3.2}$$

to extract the oscillation frequency ω and the decay time τ (for completeness: D_0 is the dipole amplitude and ϕ an additional phase shift). The MicPIC simulations show a 15% smaller decay time and also a slightly lower oscillation frequency. While the smaller decay time is attributed to additional energy loss from the cluster by radiation, the lower oscillation frequency is a field retardation effect known as the polaritonic plasmon red shift [76].

The excellent agreement of MD and MicPIC for the smaller 10 nm cluster strongly supports the conclusion from section 3.1 that microscopic effects are correctly accounted for. Further, the difference in the total final energies for the larger 30 nm system, which are of the order of the total absorption, impressively demonstrates the large error introduced by a pure electrostatic treatment of large clusters.

3.2.2. Radius-dependent absorption and scattering: comparison with continuum models

In the next step, the onset and relevance of field propagation effects in the laser-cluster interaction are studied systematically as function of the system size in terms of light absorption and scattering. To compare the MicPIC results to predictions from continuum theory, it is convenient to represent the nanoplasma as a homogeneous metallic sphere of radius R. The dielectric response of such a nanoplasma is essentially determined by the conduction electrons and can therefore be described by a Drude-like relative dielectric function $\varepsilon(R, \omega)$. Here it is defined by

$$\varepsilon(R, \omega) = 1 + \chi_0 - \frac{{\omega_p}^2}{\omega^2 + i\omega\nu(R)}, \tag{3.3}$$

with χ_0 a real-valued background susceptibility, ν the collision frequency and $\omega_{\mathrm{pl}} = \sqrt{e^2 n_e / m_e \varepsilon_0}$ the plasma frequency.[5] To include both, electron-ion and electron-surface collisions in the cluster response, a cluster radius dependent collision frequency $\nu(R) =$

[5] The frequency of the Mie plasmon of a small, perfectly metallic sphere is $\omega_{\mathrm{Mie}} = \omega_{\mathrm{pl}}/\sqrt{3}$.

$\nu_0+\nu_1/R$ is used, with ν_0 the regular bulk collision frequency and an additional surface collision term ν_1/R [76]. In this representation, ν_1 corresponds to an effective electron velocity, determining the collision rate of electrons with the cluster surface. All relevant microscopic effects are encoded in this dielectric function by the collision frequency and susceptibility. Knowledge of these parameters is key to a meaningful description of laser absorption and scattering in clusters with macroscopic continuum theories like Mie theory.

The term Mie theory is typically used to describe the exact solution of Maxwell's equations for the scattering of plane waves by homogeneous spherical objects, as published first by Gustav Mie in 1908 [77]. This solution is based on a series expansion of the internal electromagnetic fields in terms of spherical vector wave harmonics. The expansion coefficients can be deduced by exploiting the boundary conditions at the particle surface. A detailed description of the method can be found in standard literature [78, 79]. However, the important fact for this work is that Mie theory provides an exact solution[6] for the frequency and radius dependent absorption

$$\sigma_{\mathrm{abs}}^{\mathrm{mie}}(\varepsilon(\omega),R)=\frac{2\pi c^2}{\omega^2}\sum_{n=1}^{\infty}(2n+1)(\Re\{a_n+b_n\}-|a_n|^2-|b_n|^2) \tag{3.4}$$

and scattering

$$\sigma_{\mathrm{sca}}^{\mathrm{mie}}(\varepsilon(\omega),R)=\frac{2\pi c^2}{\omega^2}\sum_{n=1}^{\infty}(2n+1)(|a_n|^2+|b_n|^2) \tag{3.5}$$

cross sections, where $a_n(\varepsilon(\omega),R)$ and $b_n(\varepsilon(\omega),R)$ are the Mie coefficients. In the small-sphere limit, the Mie solution reduces to the quasi-electrostatic Rayleigh solution, where propagation effects are neglected (for details see [79]). The corresponding absorption cross section becomes

$$\sigma_{\mathrm{abs}}^{\mathrm{stat}}(\varepsilon(\omega),R)=\frac{4\pi R^3}{c}\,\Im\left[\frac{\varepsilon-1}{\varepsilon-2}\right]. \tag{3.6}$$

This result is equivalent to the heating rate used in the well-known nanoplasma model introduced by Ditmire *et al.* [80]; therefore the small-sphere electrostatic limit is called nanoplasma theory from here on. The small-sphere expression for the scattering cross section is given by

$$\sigma_{\mathrm{sca}}^{\mathrm{stat}}(\varepsilon(\omega),R)=\frac{8\pi R^6\omega^4}{3c^4}\left|\frac{\varepsilon-1}{\varepsilon-2}\right|^2. \tag{3.7}$$

Note, that both small-sphere cross sections exhibit a pole for $\varepsilon\to-2$. These poles can be connected to the Mie plasmon resonance, i.e. the resonant collective dipole oscillation of the conduction electrons in a sphere.

Finally, to compare results from the Mie and nanoplasma models with numerical data from MicPIC and MD calculations for excitation scenarios with short laser pulses, the

[6] The validity of Mie theory is confined to the linear response regime and requires a local dielectric function (no k-dependencies).

cross-sections need to be averaged over the spectrum of the laser pulse[7]. The effective cross-sections then follow from

$$\tilde{\sigma}(R) = \int I(\omega)\sigma(\varepsilon(R,\omega),R)\mathrm{d}\omega, \tag{3.8}$$

with the normalized intensity spectrum $I(\omega)$ of the laser pulse. Normalizing the cross sections to the geometrical cross sections of the sphere yields the single frequency

$$Q_{\mathrm{abs/scat}}^{Mie/NP}(R) = \frac{\sigma_{\mathrm{abs/scat}}^{Mie/NP}(R)}{\pi R^2} \tag{3.9}$$

and spectrally averaged efficiency factors

$$\tilde{Q}_{\mathrm{abs/scat}}^{Mie/NP}(R) = \frac{\tilde{\sigma}_{\mathrm{abs/scat}}^{Mie/NP}(R)}{\pi R^2} \tag{3.10}$$

for absorption and scattering.

To obtain corresponding efficiencies from numerical MicPIC and MD calculations, the absorbed and scattered energies have to be determined. The total absorbed energy E_{abs} is given by the difference in the total energy before and after the laser excitation. The total scattered radiation energy is measured using the Larmor formula (see [78,81])

$$E_{\mathrm{scat}} = \frac{1}{6\pi\varepsilon_0 c^3}\int_{-\infty}^{\infty}\left|\partial_t^2\mathbf{p}(t)\right|^2\mathrm{d}t, \tag{3.11}$$

where $\mathbf{p}(t)$ denotes the dipole moment of the cluster. The efficiencies then follow from normalization to the laser energy propagating through the geometric particle cross section

$$\tilde{Q}_{\mathrm{abs/scat}}^{\mathrm{MD/MicPIC}}(R) = \frac{E_{\mathrm{abs/scat}}(R)}{\pi R^2\int I(t)\mathrm{d}t}. \tag{3.12}$$

Absorption and scattering efficiencies obtained from MicPIC and MD calculations are shown as symbols in Figure 3.3. The agreement for small cluster radii, where propagation effects are negligible and MD describes the classical cluster dynamics exactly, reflects that MicPIC correctly accounts for collisions. For larger clusters MD and MicPIC results start to deviate significantly. The smaller MicPIC absorption indicates the growing influence of field propagation effects like radiation damping. In this size regime, MD is no longer applicable and MicPIC data have to be validated by comparison to Mie theory. In order to make this comparison possible, the parameters in the dielectric function (eq. 3.3) have to be determined from the MicPIC and MD results.

Under the assumption that the excitation takes place in the linear response regime, MicPIC results can be compared to Mie theory for any cluster size. MD analysis and nanoplasma model on the other hand do not account for propagation effects and are

[7] Gaussian laser pulses with carrier frequency ω_0, duration τ, field envelope $\exp(-t^2/\tau^2)$ and corresponding normalized intensity spectrum $I(\omega) = \tau\exp(-[\omega-\omega_0]\tau^2/2)/\sqrt{2\pi}$ are considered.

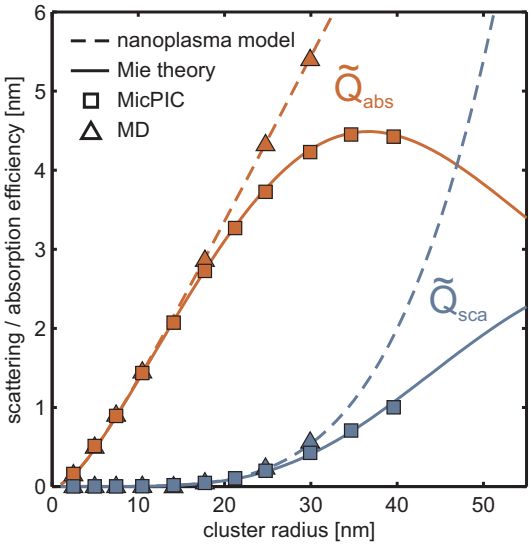

Figure 3.3.: Absorption (Q_{abs}) and scattering (Q_{sca}) efficiencies of metallic clusters excited at resonance (800 nm) by 7 fs laser pulses with a peak intensity of $6 \times 10^{11}\mathrm{W\,cm^{-2}}$. The efficiency is defined as the absorbed and scattered energies normalized by the pulse fluence and geometrical cluster cross-section. Published in [75].

only applicable to the small cluster limit. However, since they use the same approximations, they describe the same physical scenario and must fit to each other even outside their region of applicability. Matching the nanoplasma model to the MD results yields the coefficients for the real-valued background susceptibility $\chi_0 = 0.15$, the bulk collision frequency $\nu_0 = 0.102\,\mathrm{fs}^{-1}$ and the effective electron velocity $\nu_1 = 2.4\,\mathrm{nm\,fs}^{-1}$ as a measure of the surface collision contribution to the optical response. As the nanoplasma model is derived as a limiting case of Mie theory, the dielectric function for both continuum approaches has to be same. Using the same parameters in the Mie model yields excellent agreement with MicPIC for the entire size range, compare solid lines and squares in figure 3.3. The agreement of both microscopic simulations (MD and MicPIC) with the respective continuum model (based on the same dielectric function) clearly demonstrates the validity and consistency of the MicPIC approach up to large cluster radii, where field propagation plays an important role.

The physics described in figure 3.3 reveals the following picture. In the size regime $R \gtrsim 20\,\mathrm{nm}$, the increasing influence of field attenuation and radiation damping leads to substantially reduced MicPIC absorption when compared to the MD results. Eventually, these effects start to dominate the interaction and the MicPIC absorption efficiency decreases for even larger clusters. As a result, $\tilde{Q}_{\mathrm{abs}}$ shows a pronounced maximum at $R \approx 37.5\,\mathrm{nm}$ that indicates the existence of an optimal cluster size for resonance-enhanced absorption. Note that, though the absorption efficiency stays finite in the MicPIC calculation it still reaches values beyond unity for $R \geq 8\,\mathrm{nm}$, which implies absorption cross sections higher than the geometric cross section of the sphere. In analogy to the extinction paradox [82] this phenomenon is referred to as the absorption paradox. Similar to an antenna, the absorption cross section is not limited to the geometric cross section.

3.3. Competition of bulk and surface collisional effects with radiation damping in resonant clusters

So far, the main purpose of the radius dependent comparison was the validation of MicPIC. Regarding the physics, the main result obtained by this comparison is the set of material parameters in the dielectric function. These parameters quantify the effect of microscopic processes in the continuum models. Without knowledge of their magnitude, continuum models are confined to qualitative predictions. The determination of such optical material parameters by experimental measurements or theoretical calculations has been proven to be difficult. Especially when two or more different processes contribute to a single parameter, such as bulk and surface collisions in a cluster or nanoparticle, it is very difficult to unravel the contributions of the various processes. However, the parametric dielectric function used for the Mie theory calculations, allows to selectively turn specific contributions on and off. In this section this freedom is utilized to study the relative importance of surface and bulk effects as a function of cluster size, by either taken into account or neglecting surface collisions ($\nu_1 = 0$).

Figure 3.4 shows the radius-dependent spectral profiles of the absorption efficiencies with (a) and without the surface collision term (b). To highlight the spectral region of interest, the intensity spectrum of the laser pulse used for the calculation of the spectrally averaged efficiencies is indicated. Inspection of the absorption efficiencies in figures 3.4a and 3.4b reveals a pronounced polaritonic red shift of the peak efficiency (solid line) with increasing particle size, irrespective of the surface damping term. Further, both the peak value and width of the absorption efficiency profiles show a clear sensitivity to surface effects up to a radius of about 80 nm. Neglecting surface effects ($\nu_1 = 0$), the efficiency profiles increase more rapidly for small cluster sizes, are narrower, and reach a substantially higher peak value around 40 nm when compared to the prediction including the surface contribution, compare figures 3.4a and 3.4b. These obvious deviations clearly show the strong influence of surface collisions even for relatively large cluster sizes.

A closer analysis of the exact shape of the absorption profiles allows to determine an experimentally relevant and accessible parameter, i.e. the Mie plasmon linewidth $\Delta E(R)$. To extract its size dependence for both versions of the dielectric function, the absorption profiles in figure 3.4a and 3.4b are fitted with a Lorentzian curve. The results are displayed in figure 3.4c in terms of the plasmon lifetime, which is directly connected to the linewidth by the uncertainty relation $\tau(R) = \Delta E(R)/\hbar$.

From the comparison of the results for both versions, the following conclusion can be drawn. Neglecting the surface collisions leads to maximal plasmon lifetimes for small particles that decrease monotonically with increasing cluster radius, due to the increasing impact of radiation damping. On the other hand, a qualitatively different behavior can be observed when surface collisions are taken into account. The plasmon lifetime now shows a distinct maximum for cluster radii in the range of a few ten nanometers. The additional decrease in lifetime for small particles directly reflects the surface damping, which becomes increasingly important for small clusters as the

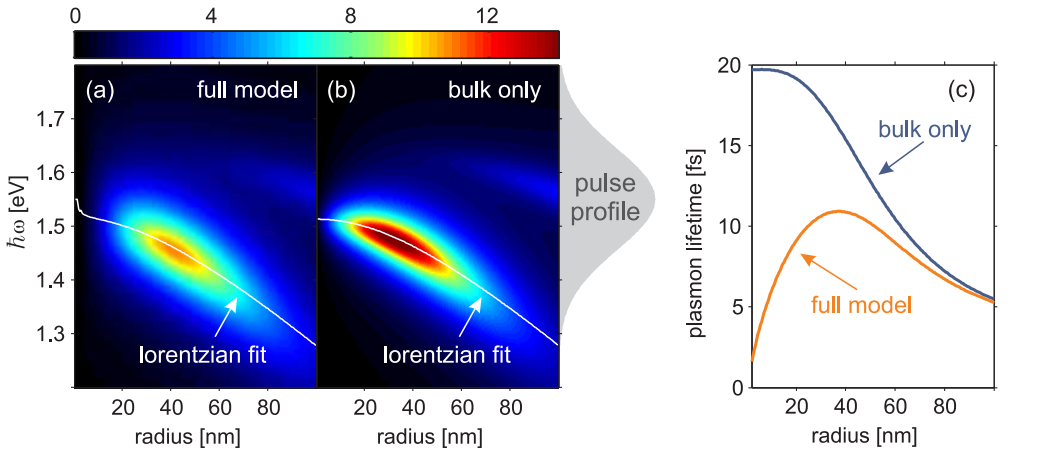

Figure 3.4.: Spectral profiles of absorption efficiencies from Mie theory with full (a) and bulk-only (b) collision frequency as a function of the particle radius . White lines indicate the size-dependent peak of the absorption efficiency. Panel (c) shows the corresponding size-dependent plasmon lifetimes extracted from a Lorentzian fit of the absorption profiles. Published in [75].

surface to volume ratio increases. For larger particles the full result converges to the bulk behavior as expected. Thus, the pronounced maximum lifetime found in the full model is a result of the competition between the surface and bulk collisions with radiation damping.

Maximal Mie plasmon lifetimes in this size range have also been observed experimentally for spherical noble-metal nanoparticles [83–85]. The fact that both, measured optimal particle size and peak lifetime are of the same order of magnitude as the theoretical results indicates that MicPIC has the potential to provide predictions on a quantitative level. However, so far only classical surface effects have been taken into account. It is therefore desirable to include quantum effects, at least in an effective way. This, however, is beyond the scope of the current work.

4. Laser driven plasma wave dynamics

When clusters are subject to high intensity optical laser fields, they are quickly turned into localized, highly ionized finite plasmas, that expand on a femtosecond to picosecond time scale. Under appropriate conditions (see introduction) the generated electron plasma can be collectively excited to oscillate against the ionic background, which is also known as the Mie plasmon. This chapter concentrates on a feature that is directly connected to the collective electron motion, namely the creation of electronic plasma waves, i.e. propagating electron density fluctuations. In the following MicPIC results are presented where these plasma waves are studied for large clusters in resonant and non-resonant excitation scenarios.

The first section provides a detailed analysis of the generation and evolution of such electronic plasma waves. In order to keep this initial analysis as simple and clean as possible, the pre-ionized and pre-expanded nanoplasmas that were already utilized for the resonant excitation studies (at 800 nm) in the last chapter, are applied as model systems. They are well suited targets for this analysis as they (i) exhibit an initially homogeneous density profile with no spatial dependencies apart from the spherical geometry of the cluster, which significantly simplifies the analysis. (ii) The resonant density ensures strong excitation of the Mie plasmon, which facilitates the generation of plasma waves with high oscillation amplitudes. (iii) The absence of additional atomic ionization as a possible damping mechanism further simplifies the analysis and ensures maximum possible clarity and density contrast. The MicPIC simulations reveal a pronounced plasma wave dynamics that shows a transition from regular to turbulent wave behavior and results in strong density fluctuations and electric field hot spots on the nanometer space and attosecond time scales.

In the second part of this chapter (Sec. 4.2) the intertwining of plasma wave generation/propagation and atomic ionization via electron impact and tunnel ionization is investigated. To this end, charge neutral Xenon clusters with a homogeneous ion inner charge state of Xe^{4+} are considered. Again, the cluster density has been chosen such, that the plasmon can be excited resonantly by 800 nm laser light. The MicPIC calculations show that electron impact ionization provides an additional damping mechanism for the plasma waves that reduces the magnitude of the resulting field and density fluctuations. Nevertheless, in the considered scenario the excited plasma waves are still strong enough to drive strongly nonuniform enhanced ionization.

Finally, in Sec. 4.3 the generation and propagation of such plasma waves is analyzed for initially neutral clusters at solid density. This scenario serves as a test case to evaluate the influence of plasma waves in single-shot experiments or the pump stage of dual pulse experiments. Here, the analysis has been performed for a $R = 25$ nm Xenon cluster, starting from the neutral cluster ground state. The calculations show, that despite the nonresonant excitation and the additional damping due to electron impact

ionization, the creation of plasma waves is a quite robust feature in the excitation of clusters with NIR laser pulses. Surprisingly, the plasma wave dynamics results in a nonuniform ionization enhancement that is even more pronounced than for the resonant excitation scenario. These results show that it is very likely that plasma waves do play a role in most cluster experiments with excitation in the optical regime (e.g at the Ti:Sa wavelength of 800 nm).

Please note that the results discussed in section 4.1 and 4.2 have been published already and are included here for convenience. The discussion is geared close to that in the original publications [62, 75] with additional information given where appropriate. Section 4.3 provides extending studies that have become possible only in late stages of this Phd project via the availability of more potent hardware.

4.1. Generation and evolution of plasma waves

This first section concentrates on the generation process and time evolution of electronic plasma waves in clusters. Apart from the higher laser intensity ($1\times10^{13}\,\mathrm{Wcm^{-2}}$), the scenario used for this study is the same as the one described in Sec. 3.2[1]. Selected snapshots of the laser-cluster interaction are shown in figure 4.1. The top panels (a-f) show total charge density distributions in the x-y plane (the laser is polarized in x-direction) for different points in time. The corresponding time instants are also put into relation to the laser field and dipole moment, see vertical lines in the inset. Figures 4.1a and 4.1b show that the plasma waves are produced at the cluster poles (where the x-axis intersects the cluster surface) and propagate to the cluster center. As the dipole amplitude grows, the plasma waves get stronger and penetrate deeper into the cluster (4.1c). Once the plasma waves are strong enough to reach the cluster center, they collide and wave breaking occurs, see panels 4.1e and 4.1f. As the plasma waves are generated in the mixed geometry of a sphere and the linear cluster polarization field, they show properties of both, spherical and plane waves.

To identify the origin of the plasma wave dynamics, it is helpful to take a look at the corresponding electron phase space distributions $f(x, v_x)$, which are shown in the lower panels of figure 4.1 (panels g-l)[2]. The dominant feature in the first snapshot is a rectangular occupied region in the phase space, which is centered in space and shifted upwards in the velocity coordinate. The elongations of this region along the space and velocity coordinates are determined by the cluster diameter and the width of the electron velocity distribution, respectively. When the electron cloud oscillates collectively against the ionic background, this region oscillates in both directions. During this trivial oscillation, part of the electrons is driven out of the cluster when the electron cloud is pushed over the cluster boundary leaving unscreened ions behind on the opposite side (see yellow region on the left cluster boundary in figure 4.1a). The resulting polarization creates a strong attractive force that accelerates part of the escaping electrons back into the cluster. When these electrons hit the cluster surface, a plasma wave is created that propagates towards the cluster center together with the

[1] A metal-like cluster of radius $R = 30\,\mathrm{nm}$ is resonantly excited with a 7 fs laser pulse at 800 nm.
[2] The phase space snapshots correspond to the same times as the density plots above.

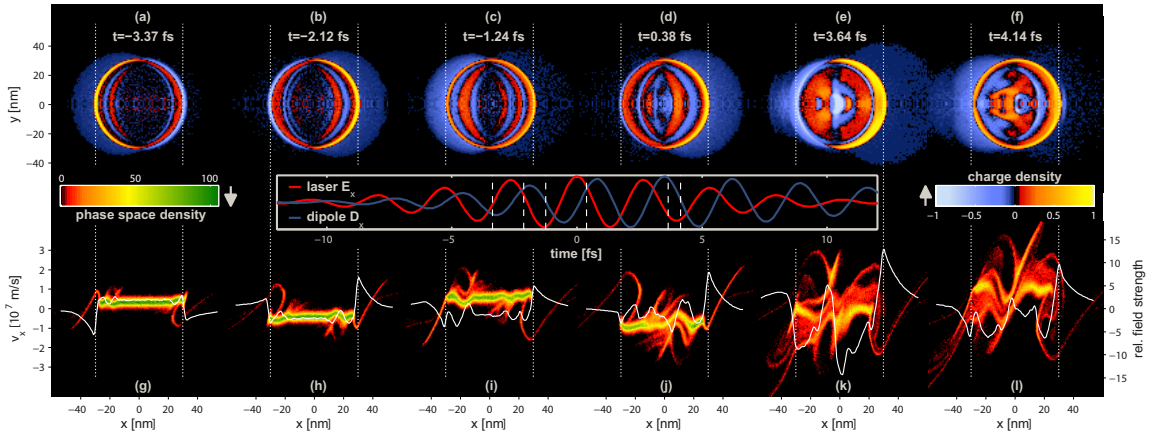

Figure 4.1.: Time evolution of an $R = 30\,\text{nm}$ cluster excited at resonance (800 nm) by a 7 fs laser pulse with a peak intensity of $6 \times 10^{13}\text{Wcm}^{-2}$. The top panel shows the charge density (normalized to the ion density) in the xy plane at different times indicated below the tags (a)(f) and as vertical lines in the plot of the laser field and dipole moment (see the inset). The lower panels (g)(l) show the corresponding electron density in the phase-space $f(x, v_x)$ evaluated on the x-axis. The x component of the electric field (normalized to the peak laser field) is shown as a white curve on top of the phase-space graphs. Published in [75].

recolliding electron bunch. In the phase space snapshots, the excited plasma wave appears as a dip, c.f. 4.1h. Near the pulse peak, the plasma waves become strong enough to reach the cluster center where they collide with waves traveling in the opposite direction and wave breaking occurs. The resulting turbulent wave dynamics leads to a strong fragmentation of the electron phase space and very high local electric fields that significantly exceed the peak laser electric field, c.f white curve in figures 4.1j-l.

A more detailed view on the dynamics induced inside the cluster is given in figure 4.2 in terms of the charge density (panel a) and local electric field (panel b) traced on the polarization axis as a function of time. For orientation, the time evolution of the exciting external laser field is shown in the panel to the right. Figure 4.2a shows that plasma waves are created at the left and right boundaries of the cluster. In the beginning ($t < -2\,\text{fs}$), when the laser pulse is still rising, the plasma waves are too weak to propagate far into the cluster. During this phase, the corresponding fields evolves close to that of a polarized metallic sphere with a nearly homogeneous profile inside the cluster, c.f. 4.2b. This behavior changes dramatically once the plasma waves get strong enough to reach the cluster center, shortly after the pulse peak. The colliding waves produce very strong spatial and temporal density and field fluctuations on the nanometer length and attosecond time scale, compare figures 4.2a and b at $t \approx 5\,\text{fs}$. Note that in a perfect metallic sphere, the charges in the interior of the sphere would be very efficiently screened, strong electric field gradients would be expected only at the cluster poles due to charge separation induced by the electron cloud oscillation. However, in this scenario the turbulent plasma wave dynamics induces strong field enhancements inside the cluster, such that the electric field intensity ($\propto E^2$) locally exceeds the laser peak intensity by more than two orders of magnitude.

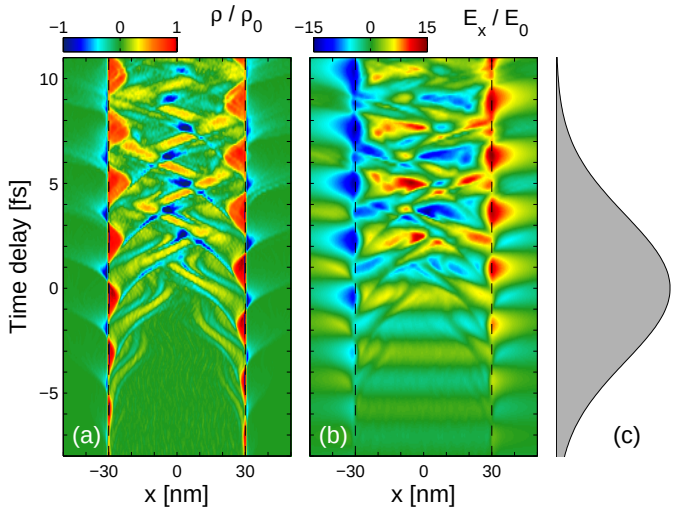

Figure 4.2: Time evolution of (a) the charge density (in units of the ion charge density) and (b) the electric field (E_x in units of the peak laser electric field) on the x-axis of a 30 nm cluster excited by a 7 fs pulse (800 nm) at an intensity of $6 \times 10^{13}\,\mathrm{Wcm}^{-2}$. (c) Time zero corresponds to the peak of the laser pulse. Published in [75].

4.2. Ionization in the vicinity of plasma waves

Sufficiently strong plasma waves can lead to turbulent wave dynamics that results in very strong local electric fields inside the nanoparticle. Applying such high electric fields to heavier element clusters, where a nanoplasma can exist while part of the electrons is still bound to their mother ions, is expected to strongly influence the ionization dynamics, e.g. by enhanced tunnel ionization. However, efficient electron impact ionization may also act as an effective electron cooling mechanism. Energetic electrons that are trapped in the space charge potential of the cluster can keep ionizing the ionic background as long as their kinetic energy is sufficiently high, loosing the respective binding energy for every released electron. Thus, electron impact ionization is expected to provide an additional damping mechanism for the plasma waves.

In order to study the effect of the plasma waves on the ionization dynamics and vice versa in detail, the resonant excitation of a charge neutral Xenon cluster is investigated. The laser parameters used here are the same as in the last section. The cluster has been initialized with a homogeneous ion charge state Xe^{4+} and ion Wigner-Seitz-radius $r_s = 5.6\,\text{Å}$ such that the system is in resonance with laser light of 800 nm wavelength. The electrons are relaxed to a steady state with a temperature of 4 eV to mimic the system state prior to the probe pulse in a pump-probe experiment.

Figure 4.3 shows selected snapshots of the laser-cluster interaction. In analogy to section 4.1 the top panels (a-f) show the total charge density distributions in the x-y plane and the lower panels (g-l) the electron phase space distributions $f(x, v_x)$. Though the plasma wave signatures are not as pronounced as in the hydrogen-like system in the last section, they are still very clear. The physics observed here is qualitatively the same as in the scenario without ionization above. The major differences are: (i) A reduced contrast in the charge density distribution (limits of the corresponding colorbars in figures 4.1 and 4.3 differ by a factor of 2), which can be mainly attributed to more efficient electron-ion collision due to the higher charges

of the ions. (ii) The lower maximum electron kinetic energies during the turbulent wave dynamics (c.f. figures 4.1l and 4.3l) which can be attributed to energy loss by additional electron impact ionization.

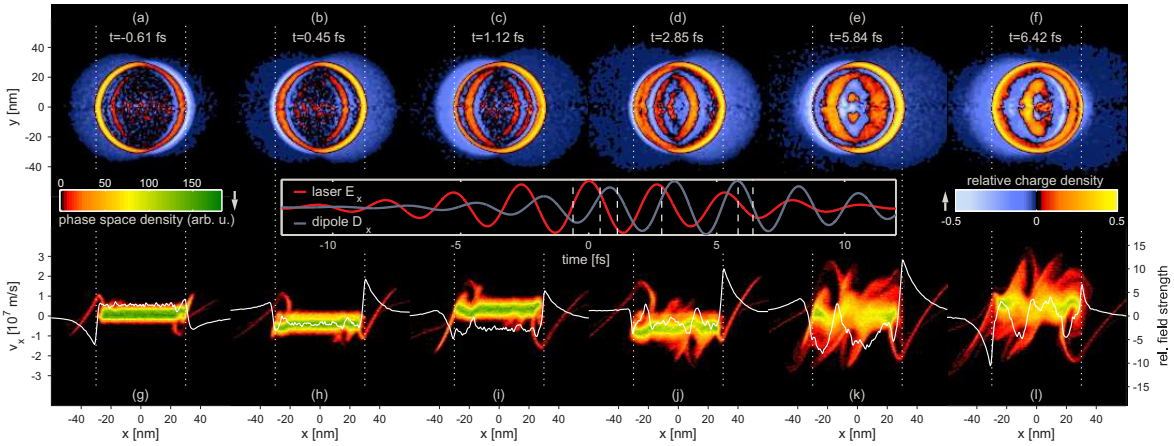

Figure 4.3.: Time evolution of a $R = 30\,\mathrm{nm}$ Xe^{4+} cluster excited at resonance (800 nm) by a 7 fs laser pulse with peak intensity $6 \times 10^{13}\,\mathrm{Wcm}^{-2}$. The top panels (a)(f) show the charge density (relative to the ion density) in the x-y plane at various times; times are also indicated as vertical lines in the plot of the laser field and dipole moment (see inset in the middle). The lower panels (g)(l) show the corresponding electron density in phase space $f(x, v_x)$ evaluated on the x axis. The x component of the electric field (normalized to the peak laser field) is shown as a white curve on top of the phase-space graphs. Published in [62].

Next, the effect of the plasma-wave dynamics on the cluster ionization is studied in more detail. Figures 4.4a-c show the spatial distributions of the total-, tunnel- and impact ionization rates for a time close to the end of the laser pulse. A pronounced spatial modulation of the ionization rates is the key signature of the plasma wave dynamics. The specific shape of the ionization rates can be understood by analyzing the driving forces in detail. Tunnel ionization is a field driven process, a comparison of the tunnel ionization rate to the distribution of the local field intensity (c.f. Figs. 4.4b and 4.4e) reveals that the regions with enhanced tunnel ionization can be clearly assigned to hot spots in the local field intensity. Similar to the scenario without ionization, the hot spots inside the cluster are created by the plasma wave propagation and collision. The generated hot spots can exceed the laser peak intensity by more than two orders of magnitude, leading to a strongly nonuniform distribution of tunnel ionization probability.

Efficient electron impact ionization on the other hand requires a high density of electrons with sufficiently high kinetic energy to further ionize the Xenon ions. The comparison of the impact ionization rate to the density of energetic electrons with $E_{\mathrm{kin}} \geq 200\,\mathrm{eV}$ (figures 4.4c and 4.4f) highlights this correspondence. The fast electrons are a result of the combined action of the collective plasmon motion and the plasma-wave dynamics. Regions with a high density of fast electrons are created where these two contributions are strong and act in the same direction. However, the correspondence between fast electrons and high impact ionization rate is slightly distorted by the effect of ionization barrier suppression due to the high local fields.

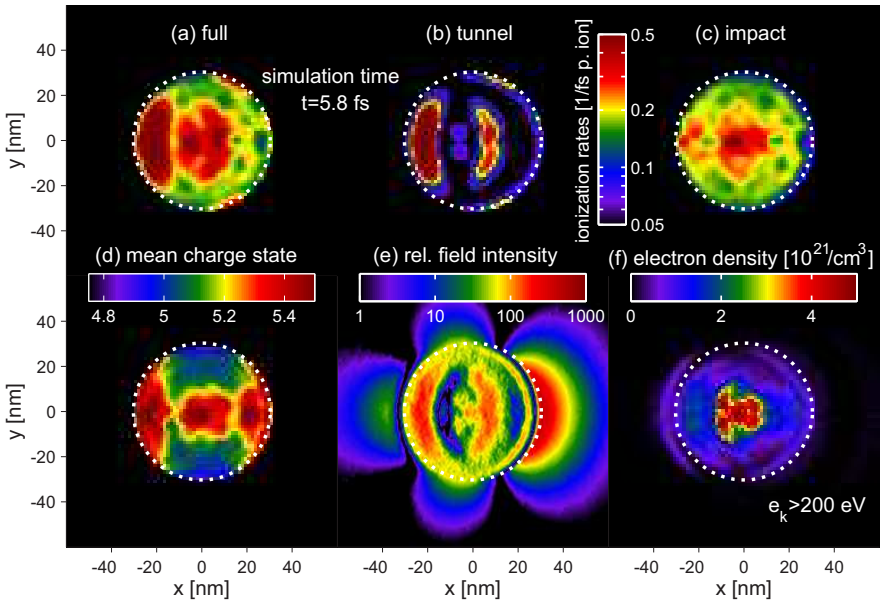

Figure 4.4.: Detailed snapshot of the run in Fig. 2 at $t = 5.8\,\mathrm{fs}$. Shown are spatial distributions of total, tunnel, and impact ionization rates (a)-(c), mean Xe charge states (d), electric field intensity normalized to peak laser field intensity E^2/E_0^2 (e), and fast electrons (f) with kinetic energy $e_k > 200\,\mathrm{eV}$. Published in [62].

Eventually, both enhanced tunnel- and impact ionization leave their characteristic footprints in the spatial charge state distribution, shown in Figure 4.4d. The increased charge states at the cluster poles can be attributed to enhanced tunnel ionization in the vicinity of the strong polarization fields that are created when the electron cloud is pushed over the cluster boundary. The increased average charge state in the center of the cluster is a clear signature of the plasma wave dynamics, as it enhances both tunnel- and impact ionization in this region. Note again, that charges at the cluster center are typically well screened and the observation of enhanced ionization in this region is not to be expected.

4.3. Plasma waves in solid density matter

As a logical next step, the effect of laser driven plasma waves on the ionization dynamics is studied in solid density matter. To this end the excitation of a $R = 25\,\mathrm{nm}$ Xenon cluster, initialized with a Wigner-Seitz radius of $r_s = 2.6\,\mathrm{Å}$, with a 10 fs laser pulse of 800 nm wavelength and $10^{15}\,\mathrm{W/cm^2}$ peak intensity is analyzed. This scenario completes the investigations of the plasma wave dynamics as it describes a possible pump-pulse excitation stage for the probe-only scenario discussed in the section above. As the excitation starts here from the neutral cluster ground state, the plasma creation dynamics is briefly discussed first. Figure 4.5 shows the time evolution of selected observables during and after the laser excitation.

Plasma formation starts with tunnel ionization in the leading edge of the pulse, c.f. 4.5d. Laser heating of these electrons subsequently drives an impact ionization

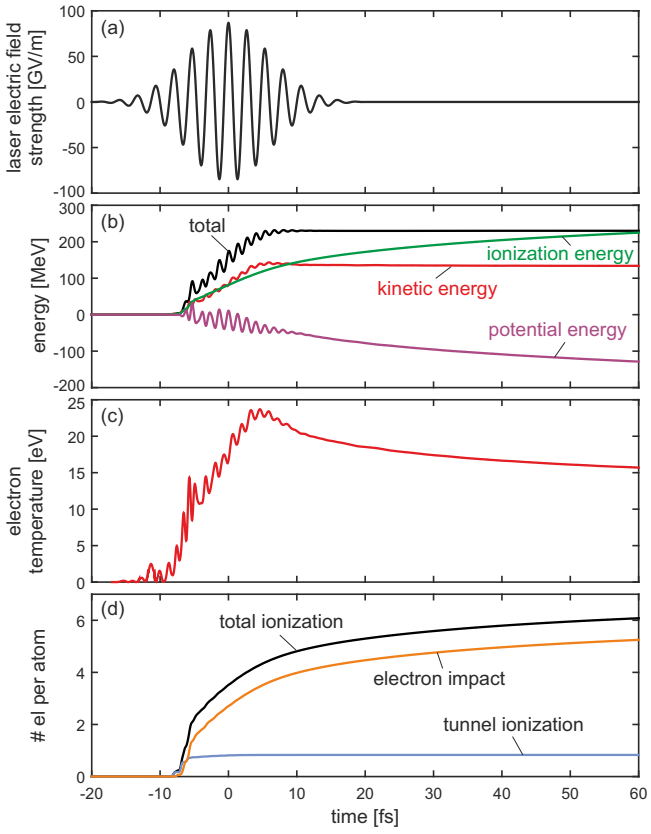

Figure 4.5: Time evolution of selected observables during and after the excitation of a $R = 25\,\mathrm{nm}$ Xe Cluster at solid density by a 10 fs laser pulse with peak intensity $1 \times 10^{15}\,\mathrm{W/cm^2}$; (a) electric field strength of the incident laser pulse, (b) kinetic, potential, total absorbed and ionization energy, (c) electron temperature and (d) inner ionization with contributions from tunnel and electron impact ionization.

avalanche that eventually contributes roughly 80% of the inner ionization events. As a result the average inner charge state increases very fast and tunnel ionization becomes ineffective within a few femtoseconds due to low ionization rates (see blue curve in 4.5d). However, impact ionization continues even after the laser pulse has ended and energy absorption has stopped, compare figures 4.5b and 4.5d. This after-pulse-ionization is driven by the thermal energy of the already liberated plasma electrons and acts as an electron cooling mechanism. Note that in contrast to electron cooling by adiabatic expansion this cooling mechanism is decoupled from the ionic motion, which is negligible in this scenario for the shown time scales.

Figure 4.6a visualizes the excited plasma wave dynamics in terms of the electric field on the polarization axis. In the early stages ($t < -8\,\mathrm{fs}$), before ionization takes place, the cluster is transparent for the incident NIR-light. Later, when a nanoplasma has been built up, the field evolves first close to that of a polarized metallic sphere with a homogeneous profile inside the cluster. Once the polarization fields get strong enough to support plasma wave generation, strong spatial and temporal field fluctuations are created. Qualitatively, this behavior is very similar to the one described in section 4.1 for resonantly driven nanoplasmas, however, the magnitude of the field fluctuations is much smaller, with peak field enhancements of only about 3 inside the cluster and no pronounced turbulent wave dynamics. This can be attributed to the fact that in addition to the damping by electron impact ionization the collective electron motion responsible for plasma wave creation is not driven resonantly in this scenario.

Though the excited plasma waves are weaker than for the idealized resonant case,

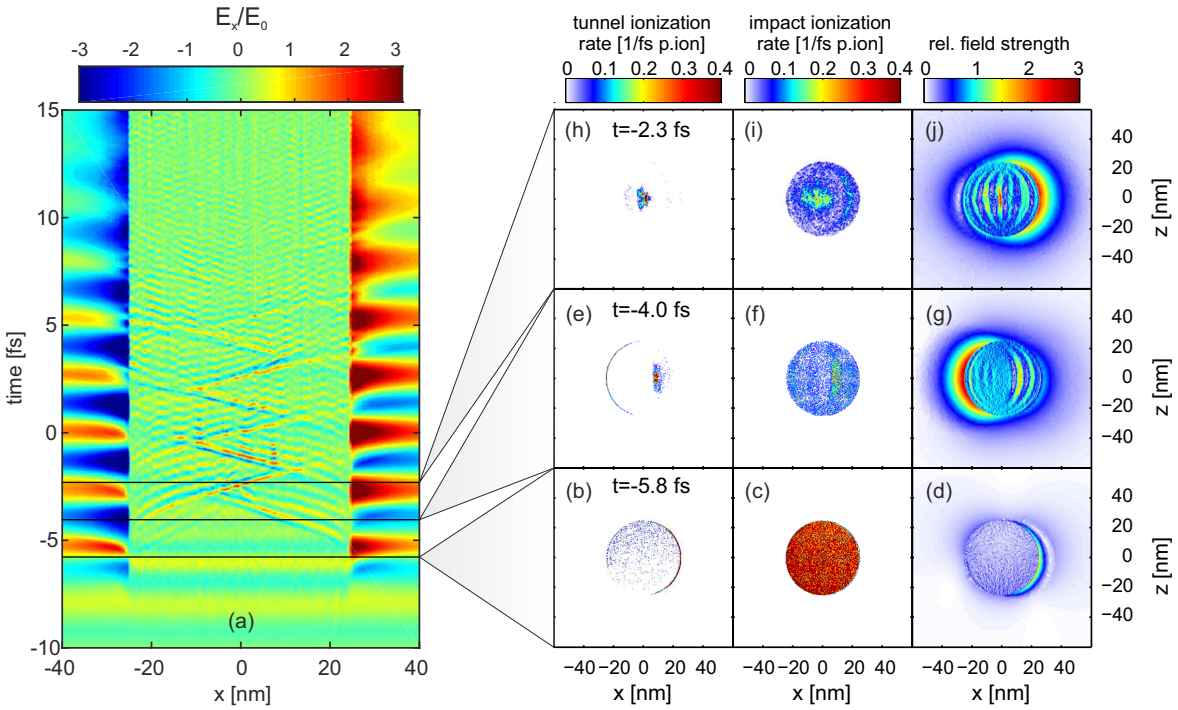

Figure 4.6.: Left side: (a) Time evolution of the electric field (E_x normalized to the peak laser electric field) on the polarization axis. Right side: Snapshots of the spatially resolved ionization rates and field strength . All panels in a column correspond to the same point in time, which is given in each top panel with respect to the pulse peak. The top two rows show the spatial distribution of tunnel ionization (b-d) and electron impact ionization (e-g) rates, respectively. The third row (h-j) shows the absolute value of the local electric fields, normalized to the maximum of the incoming laser field.

they still strongly effect the cluster ionization dynamics. The right part of figure 4.6 shows the spatially resolved ionization rates for tunnel- and impact ionization as well as the electric field distribution for three different time steps (indicated in the first panel of each row). All data correspond to the plane defined by the polarization and propagation axis. Starting with the earliest time step (panels b-d) reveals that in early stages the electric field inside the cluster is well screened by the plasma electrons, such that tunnel ionization is essentially confined to the cluster poles where the laser driven collective electron motion creates strong polarization fields, c.f. panels b and d. At this stage electron impact ionization events are distributed homogeneously throughout the cluster. However, when plasma wave generation sets in, this picture starts to change (panels e-g). The resulting field fluctuations generate field hot spots that are strong enough to drive additional tunnel ionization inside the cluster, compare panels e and g. Furthermore, the field hot spots also enhance electron impact ionization via effective ionization potential lowering. Close to the pulse peak (panels h-j), where the plasma waves are strongest, plasma wave enhanced tunnel- and impact ionization dominate the distributions as regular ionization becomes increasingly inefficient due to the already high average charge state throughout the cluster.

Figure 4.7 shows the final charge state distribution and its contributions from tunnel- and impact ionization. Tunnel ionization is most effective at the cluster poles, due to

the strong polarization fields created by the collective electron motion and in the cluster center where the plasma wave driven field fluctuations are strongest. The contribution from electron impact ionization shows a tunnel like signature similar to the resonantly driven Xenon cluster discussed in section 4.2. As a result, the combined charge state distribution exhibits a strongly nonuniform shape, with average charge states of almost Xe^{10+} close to the polarization axis and only about Xe^{6+} in the regions farthest away from it, see figure 4.7c. In conclusion, the presented calculations show that laser driven plasma waves can significantly affect the ionization dynamics of clusters even when not driven resonantly. As a result, it is likely that they effect most cluster experiments in the optical excitation regime and should be considered at their interpretation.

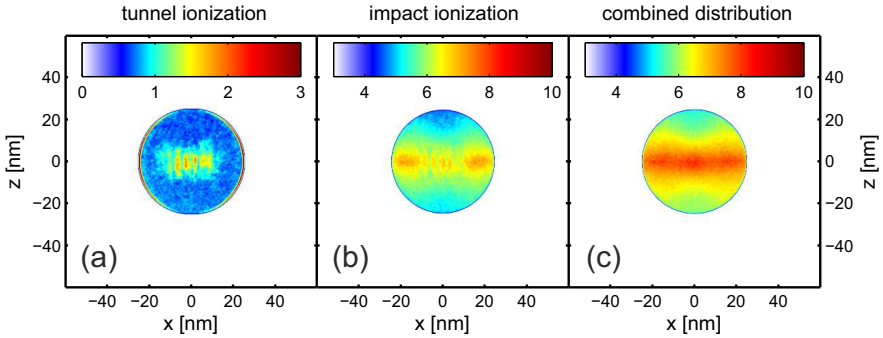

Figure 4.7.: Contributions to the final charge state distributions from (a) tunnel ionization and (b) electron impact ionization for the same scenario as shown in figure 4.6. The combined distribution of final charge states shown in panel (c) exhibits a strongly nonuniform character, with average charge states ranging from almost Xe^{10+} close to the polarization axis down to only Xe^{6+} in the regions farthest away from it.

5. Clusters exposed to intense short-wavelength radiation

The fact that MicPIC can simultaneously and self-consistently describe the microscopic plasma dynamics and the evolution of the electromagnetic fields with high spatial resolution opens up another so far not accessible application area, the direct simulation of the interaction of intense x-ray light with nanoparticles. This chapter discusses the evaluation and interpretation of elastic and inelastic x-ray scattering within the MicPIC approach as well as first examples of corresponding complete numerical experiments.

In section 5.1 the utilized simulation setup is introduced with special emphasis on the additional requirements to extract and analyze elastic and inelastic scattering contributions from the simulation. Section 5.2 presents first results on the dynamical x-ray imaging of nanoplasma expansion. In this scenario a solid density hydrogen cluster is initially excited by an intense NIR-pump pulse that fully ionizes the cluster. The expansion of the generated nanoplasma is then imaged by a soft x-ray probe pulse for different pulse delays. It will be shown that the time evolution of the anisotropic nanoplasma expansion can be represented by an analytical profile that can be reconstructed from the delay dependent scattering images with nanometer resolution.

In order to describe the interaction of initially neutral clusters with x-ray light the effect of bound electrons has to be taken into account. Section 5.3 discusses an approach to include bound electrons in terms of a classical dissipative oscillator model. It will be shown that this treatment provides a convenient way to include single photon ionization into the MicPIC approach. The last section (5.4) concentrates on the evaluation of inelastic contributions to the x-ray scattering and the additional information it can provide about the imaged system.

The results for the dynamical x-ray imaging have been already published. The corresponding discussion is therefore close to that of the original publication [86] with additional information where appropriate.

5.1. The x-ray scattering simulation setup

All results presented in this chapter are based on simulations with the same model system, namely a $R = 25\,\mathrm{nm}$ hydrogen cluster at solid density with atoms/ions initialized in fcc-structure with Wigner-Seitz radius of $r_\mathrm{s} = 1.79\text{Å}$. This is an ideal test system as hydrogen has only one electron contributing to the x-ray scattering, which significantly simplifies the analysis. For laser excitation a 10 fs soft x-ray pulse at 10 nm wavelength is considered. Depending on the specific scenario this x-ray pulse is preceded by an NIR-pump pulse to turn the cluster into a nanoplasma prior to the actual scattering.

The corresponding time dependent scattered fields are then recorded on a virtual detector located on a virtual sphere within the simulation box. The general simulation setup is shown in figure 5.1.

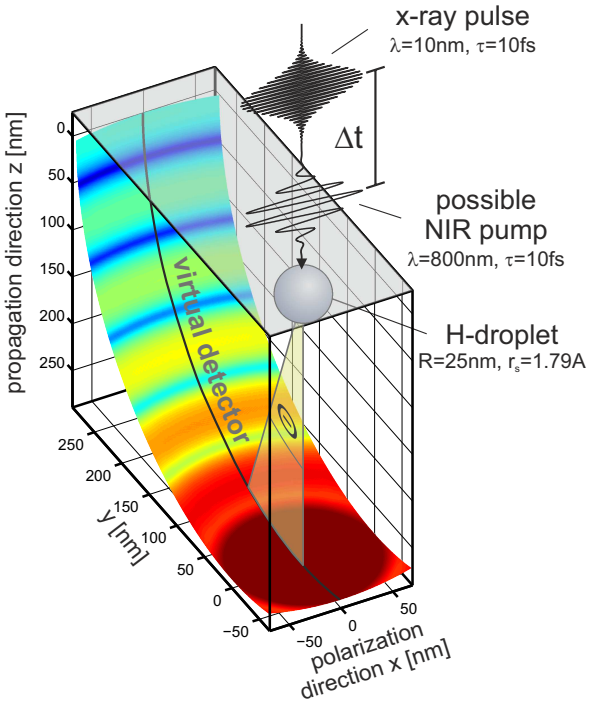

Figure 5.1.: Sketch of the x-ray simulation setup with the $R = 25\,\mathrm{nm}$ hydrogen cluster, the virtual detector (defined by a sphere with radius $R_\mathrm{d} = 290\,\mathrm{nm}$ around the cluster center), and the incident laser fields. Depending on the specific scenario discussed in this chapter, the soft x-ray pulse is applied alone or in conjunction with an NIR pump pulse.

Ideally, the radius of the detection sphere is large enough to enter the far field region, where the fields include only propagating radiation and non-radiating near field contributions have already died out. The corresponding required detector distance is not exactly defined, but as a rule of thumb, the far field region for an antenna with a dimension of the order of the emitted wavelength starts at the Fraunhofer distance $d_\mathrm{f} = \frac{2D^2}{\lambda}$ where D is the spatial dimension of the emitter. For the scenarios discussed here, this would result in a detector distance of about $R_\mathrm{d} \approx 500\,\mathrm{nm}$. A corresponding MicPIC simulation run, however, would require a very large computational box which is inconvenient from a technical point of view. Instead a slightly smaller value of $R_\mathrm{d} = 290\,\mathrm{nm}$ is utilized that allows the use of a smaller numerical box.

To analyze the effect of the finite detector distance, scattering pattern have been calculated for a non-absorbing plasma sphere of radius $R = 25\,\mathrm{nm}$ with Mie theory for detectors located in the near ($R_\mathrm{d} = 290\,\mathrm{nm}$) and far field ($R_\mathrm{d} \to \infty$) regions, compare blue and red lines in figure 5.2. It turns out that the finite detector distance has only a minor impact on the shape of the scattering signal, essentially only affecting the sharpness of the minima. Note that the scattering signal is evaluated here in terms of

the scattered fraction

$$S(\Theta) = \frac{\varepsilon_0 c R_\mathrm{d}^2}{\pi R^2 F_0} \int [\mathbf{E}(\Theta, t)]^2 \, \mathrm{d}t, \tag{5.1}$$

with ε_0 the vacuum permittivity, c the vacuum speed of light and $F_0 \approx I_0 \tau$ the fluence of the incident x-ray field. In the limit $R_\mathrm{d} \to \infty$, $S(\Theta)$ specifies the number of x-ray photons scattered into an element of solid angle per incident photon impinging on the initial geometric cluster cross section. In this representation, the envelope of the elastically scattered signal is essentially[1] size-independent as can be seen from the comparison to the scattering signal for a ten times larger cluster (light gray curve).

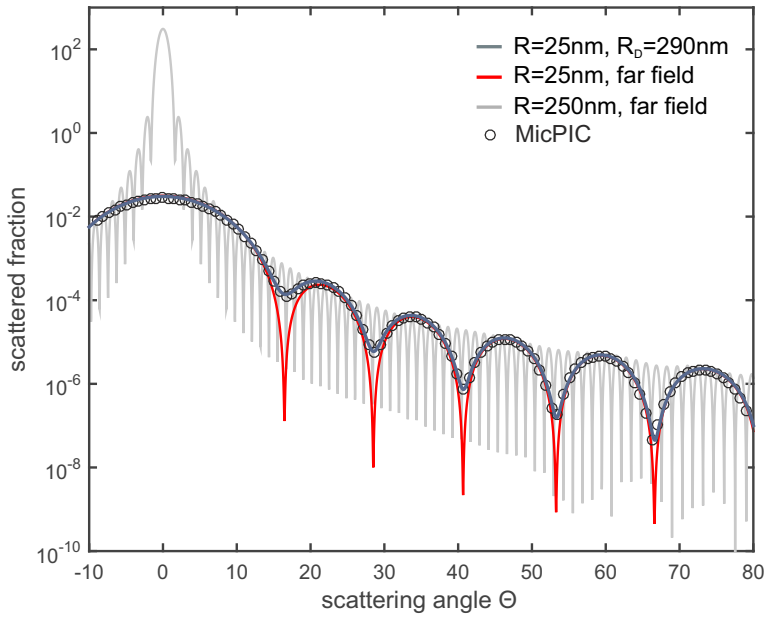

Figure 5.2.: (Lines) Scattered fraction calculated with Mie theory for medium (red and blue) and large (light gray) clusters. The red and blue curves show the scattered fraction for the medium cluster with the detector placed in the far and near field region, respectively. (circles) Corresponding MicPIC results for elastic scattering from a $R = 25\,\mathrm{nm}$ hydrogen cluster with electrons placed at rest on top of the ions.

To extract the corresponding scattered fraction from MicPIC calculations, the time dependent, angular-resolved scattered electric fields recorded on the virtual detector have to be further processed. Only transverse electric fields, i.e. with electric field vector perpendicular to the propagation direction, can contribute to the final scattering pattern. All parallel components that are only recorded because of the finite detector distance have to projected out according to

$$\mathbf{E}_\perp = \mathbf{E} - (\mathbf{E} \cdot \mathbf{r}_\mathrm{d}) \cdot \frac{\mathbf{r}_\mathrm{d}}{r_\mathrm{d}^2}. \tag{5.2}$$

The resulting transverse electric fields may still contain contributions from different spectral regions, e.g. from inelastic Thomson scattering or high harmonic generation.

[1] as long as attenuation and refraction effects are small (Born approximation limit)

Subsequent frequency filtering allows to separate elastic and inelastic contributions. Using the respective fields $\mathbf{E}^{\mathrm{el}}$ and $\mathbf{E}^{\mathrm{inel}}$ yields the MicPIC scattered fraction

$$S^{\mathrm{el/inel}}_{\mathrm{MicPIC}}(\Theta) = \frac{\varepsilon_0 c R_{\mathrm{d}}^2}{\pi R^2 F_0} \int \left[\mathbf{E}_{\perp}^{\mathrm{el/inel}}(\Theta, t)\right]^2 \mathrm{d}t. \tag{5.3}$$

To validate the description of x-ray scattering within MicPIC and its above described evaluation, the elastic scattered fraction has been calculated for an x-ray only excitation of the $R = 25\,\mathrm{nm}$ hydrogen cluster with electrons placed at rest on top of the ions. The results depicted in figure 5.2 as circles show an almost perfect agreement with the Mie results for the same detector distance (blue curve).

5.2. Time-resolved x-ray imaging of anisotropic nanoplasma expansion

This section discusses a first idea on how to retrieve the cluster dynamics induced by an intense NIR-laser pulse from dynamic x-ray imaging scattering pattern. To this end a neutral $R = 25\,\mathrm{nm}$ hydrogen cluster is excited with a 10 fs laser pulse at 800 nm wavelength. The time evolution of selected observables during and after this initial excitation is shown in the left part of figure 5.3.

Concentrating on the dynamics induced by the NIR pump pulse first, reveals the following picture: Plasma formation is triggered by tunnel ionization in the rising edge of the pulse. Subsequently, laser heating of the first liberated electrons drives additional electron impact ionization. The combined action of both contributions creates a fully inner ionized cluster near the pulse peak, see figure 5.3c. Due to the low proton mass the cluster starts to expand almost immediately (c.f. 5.3c). The expansion is driven by a mixture of hydrodynamic expansion and Coulomb explosion. Signatures of both can be found in the time evolution of the energy contributions in figure 5.3a. The observed conversion of electron kinetic energy into ion kinetic energy clearly indicates hydrodynamic expansion while the fact that the ion kinetic energy gain is stronger than the electron energy loss shows that Coulomb explosion is also contributing.

The initiated cluster dynamics is then imaged by soft x-ray probe pulses for various pulse delays. Note that the NIR induced dynamics shown in figure 5.3(a-c) is not affected by the x-ray pulse due to the negligible inverse bremsstrahlung in the x-ray regime. The resulting delay dependent elastic scattering signals shown in figure 5.3d exhibit two major pump-probe effects. First, the slope of the scattering signal increases with pulse delay, such that the signal drops by more than one order of magnitude for the largest scattering angles. And second, the separation of the fringes increases continuously with the pulse delay. Assuming the cluster keeps the shape of a homogeneous sphere during expansion, this trend would correspond to a reduction of cluster size. This behavior, however, seems to be in total contradiction with the observed increasing cluster radius shown in figure 5.3b. To shed light on this apparent contradiction, a more detailed analysis of the expansion dynamics itself is needed.

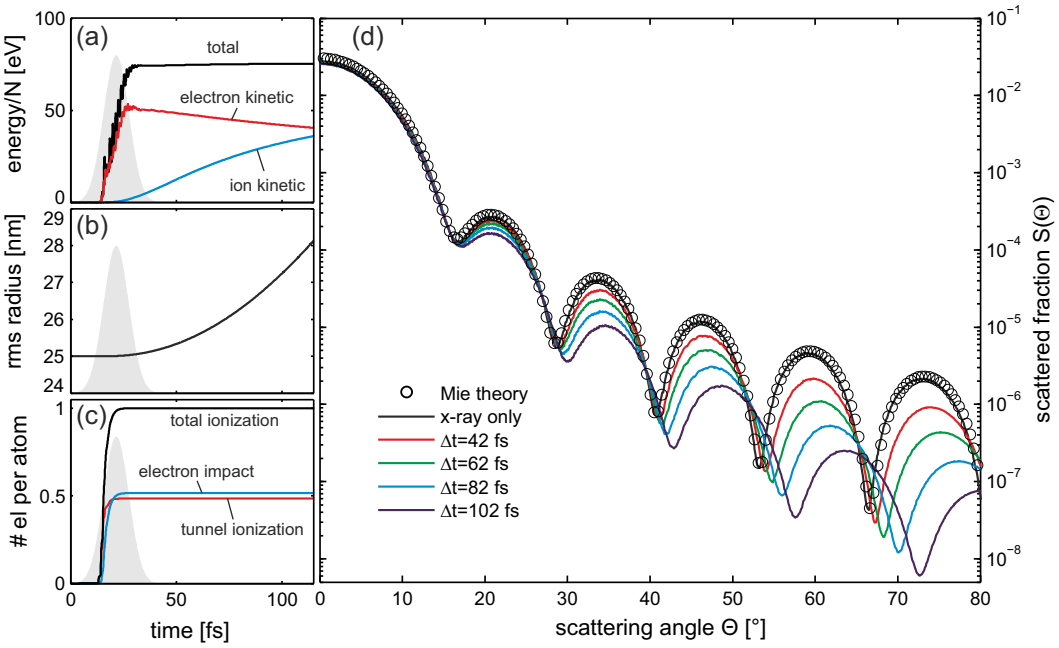

Figure 5.3.: (a)-(c) Time evolution of selected observables during and after the NIR pump excitation. (d) Resulting elastic scattered fraction (detected in the y-z plane) for different x-ray probe delays and the Mie-theory result for an unexpanded cluster for comparison. Published in [86].

Direction-resolved radial density profiles[2] of electrons and ions for directions parallel (green) and perpendicular (blue) to the laser polarization are shown in figure 5.4 for different times. In early stages, surface ions are unscreened due to partial outer ionization and consequently undergo rapid Coulomb explosion, c.f. lines and colored areas in 5.4a. The fact that the ion spectra are anisotropic can be attributed to the collective electron motion during the NIR excitation. During the oscillation of the electron cloud, ions at the cluster poles are periodically exposed, which results in an effectively reduced charge screening and stronger ion acceleration along the polarization axis [87–89]. Once the surface ions have been ejected, the remaining ion and electron densities overlap and screen each other. The cluster continues to expand hydrodynamically.

During the hydrodynamic expansion phase, the density profiles exhibit a self-similar shape with a core region of constant density and an exponential decay of the surface layer. A similar behavior has been predicted for the expansion of semi-infinite plasmas [90, 91]. The radial density profiles observed here can be accurately described in all expansion stages by a sharpened Fermi distribution

$$n_{\mathrm{e}}(r) = \frac{n_{\mathrm{c}}}{[\exp(\frac{r-r_{\mathrm{c}}}{ds})+1]^{s}}, \tag{5.4}$$

where n_{c} is the core density, r_{c} the core radius and d the decay length as a measure

[2]The density profiles have been averaged over cones with $\pi/4$ full opening angle and cone apex at the cluster center.

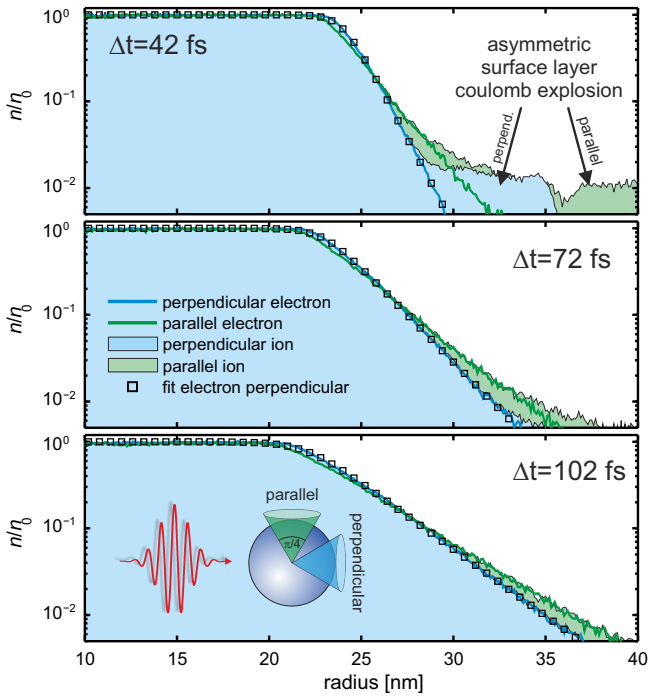

Figure 5.4.: Radial electron and ion density profiles for different pulse delays (as indicated). Solid lines (electrons) and shaded areas (ions) show density profiles extracted directly from the MicPIC simulation for directions parallel to (green) and perpendicular to (blue) the polarization direction. Open squares correspond to electron density fits perpendicular to the NIR polarization using the profile given in Eq. (5.4). Published in [86].

of the surface width. The sharpness factor s ensures the correct transition behavior between the two asymptotic limits. Examples of corresponding fits of the electron density perpendicular to the polarization direction are depicted as squares in figure 5.4.

Application of the fit procedure to all available density snapshots yields the time evolution of the density profile parameters shown in figure 5.5a-c as solid lines. Again, the blue and green curves correspond to directions perpendicular and parallel to the polarization direction, respectively. Though the actual values for both directions differ due to the anisotropic expansion, they show the same general behavior. The core radius r_c is linear decreasing with time while the surface width d is linear increasing. The sharpness factor s, on the other hand, is converging rapidly and is therefore only of minor importance for the expansion dynamics. To substantiate this statement, fits for $s \to 0$ have been performed (dashed lines in figure 5.5a and b), which corresponds to the limit of a sharp edge between core and surface region. The fact that only minor changes in core radius and surface width are observed shows that the complex plasma expansion dynamics can be sufficiently described by these two parameters.

To connect the evolution of the density profile parameters with the features observed in the delay dependent scattering images shown in figure 5.3, it is helpful to study the effect of the profile parameters on the scattering pattern separately. Unfortunately, Mie-theory is no longer applicable because of the anisotropic and inhomogeneous den-

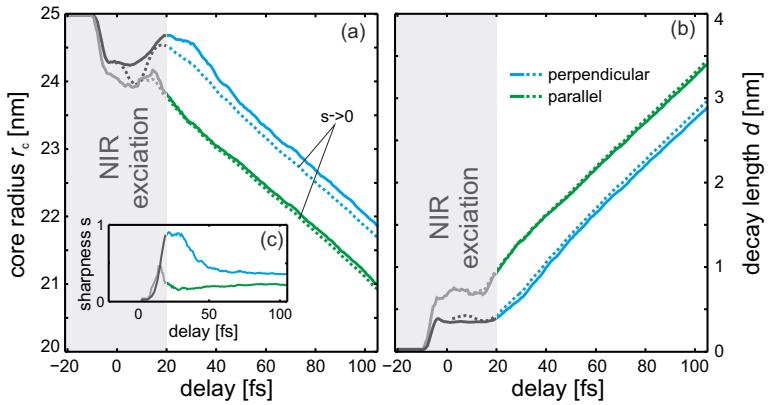

Figure 5.5.: Time evolution of density profile parameters; solid and dashed lines correspond to direct fits of the MicPIC density for directions parallel to (green) and perpendicular to (blue) the polarization direction using all parameters or the sharp edge limit $s \to 0$, respectively. Published in [86].

sity profile. An alternative is to calculate the scattered fields in first order Born approximation, where higher order scattering by neighboring scatterers is not taken into account. This is justified in the considered scenario as light absorption can be neglected at the given wavelength for hydrogen. The scattered field in first order Born approximation including polarization effects is determined by

$$\mathbf{E}(\mathbf{r}_\mathrm{d}) = \int_V \frac{\tilde{\mathbf{r}} \times (\mathbf{E}_0 \times \tilde{\mathbf{r}})\, r_\mathrm{e} e^{i(\mathbf{kr}+k\tilde{r})}}{\tilde{r}^3}\, n_\mathrm{e}(\mathbf{r})\, \mathrm{d}^3 r, \tag{5.5}$$

with $\mathbf{k}$ the incident wave vector, r_e the classical electron radius, $n_\mathrm{e}(\mathbf{r})$ an arbitrarily shaped electron density and $\mathbf{E}_0$ and $\mathbf{E}$ the complex field amplitudes of the incident field and the scattered field at detector position $\mathbf{r}_\mathrm{d}$. The detector position in the frame of each scattering subvolume is denoted by $\tilde{\mathbf{r}} = \mathbf{r}_\mathrm{d} - \mathbf{r}$. The corresponding scattered fraction in Born approximation is then given by

$$S_\mathrm{B}(\Theta) = \frac{R_\mathrm{d}^2 E_\perp^2}{\pi R^2 E_0^2}. \tag{5.6}$$

Inserting the parametric density profile from equation (5.4) into the Born expression above allows a selective analysis of the influence of the core radius and surface width on the scattering pattern by fixing the respective other parameter. The results shown in figure 5.6 reveal that the core radius r_c affects only the fringe spacing without changing the envelope of the scattering signal. The decay length d on the other hand mainly modifies the slope of the envelope and hardly changes the fringe positions. As a result, the growing fringe separation and increasing envelope slope observed in the delay dependent scattering pattern in figure 5.3 can be attributed to the shrinking core radius and the cluster surface expansion.

The above parameter analysis already allows one to qualitatively explain the observed scattering features. However, the ultimate goal is to quantitatively reconstruct the anisotropic plasma expansion dynamics from experimentally measured angular-resolved scattering images. In the following it will be discussed how this can be achieved

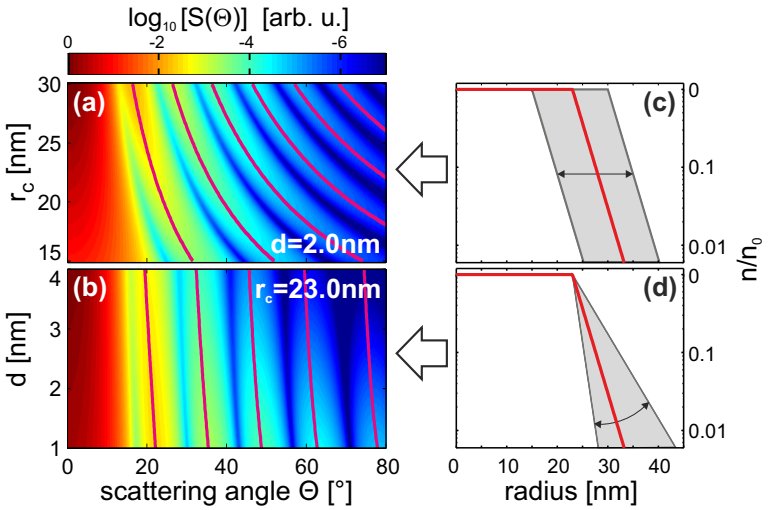

Figure 5.6.: Selective density profile parameter analysis with the Born method in the sharp edge limit (for $s \to 0$). Panels (a) and (b) show color-coded scattering spectra when only varying the core radius r_c or the surface width d, respectively. The corresponding one dimensional density profiles are shown in panel (c) and (d). Grey areas illustrate the range of variation of the profiles. Published in [86].

with the above introduced tools. First, the anisotropic character of the expansion needs to be taken into account. This can be done by using anisotropic values for the density profile parameters $r_c(\theta)$ and $d(\theta)$ in equation (5.4). The sharpness factor can be neglected as it is irrelevant for the dynamics ($s \to 0$). To model an ellipsoidal density, an angular dependence according to

$$\alpha(\theta) = \alpha_{\text{perp}} + (\alpha_{\text{par}} - \alpha_{\text{perp}}) \cos^2(\theta) \tag{5.7}$$

has been chosen for both parameters, where θ is the angle with respect to the polarization axis. Using this parametric form yields an angle dependent density profile $n(r, \theta)$ with a total of four free parameters. To mimic the full two-dimensional scattering images available in typical x-ray scattering experiments, additional MicPIC runs have been performed with a rotated virtual detector (perpendicular to the polarization direction y=0). The corresponding Born scattering patterns calculated from the angular dependent density profile $n(r, \theta)$ can now be compared to the actual MicPIC scattering pattern. Optimal values of the four free parameters are then determined by simultaneously fitting the Born images in the x=0 ($S_\perp$) and y=0 ($S_\parallel$) planes to the corresponding MicPIC results via simplex optimization. Figure 5.7c shows that the resulting Born fits accurately describe the actual direction-resolved MicPIC scattering data.

The resulting optimal parameter values retrieved from the delay dependent MicPIC scattering images are compared to the parameters directly extracted from the MicPIC electron density profiles in figure 5.7a and b. The evolution of both, the anisotropic core radius and surface width can be reconstructed quantitatively with only small deviations that are attributed to the simplified four-parameter geometry model. During the hydrodynamic expansion, electron and ion density profiles evolve together, therefore the reconstructed profiles also describe the evolution of the ion density. In summary,

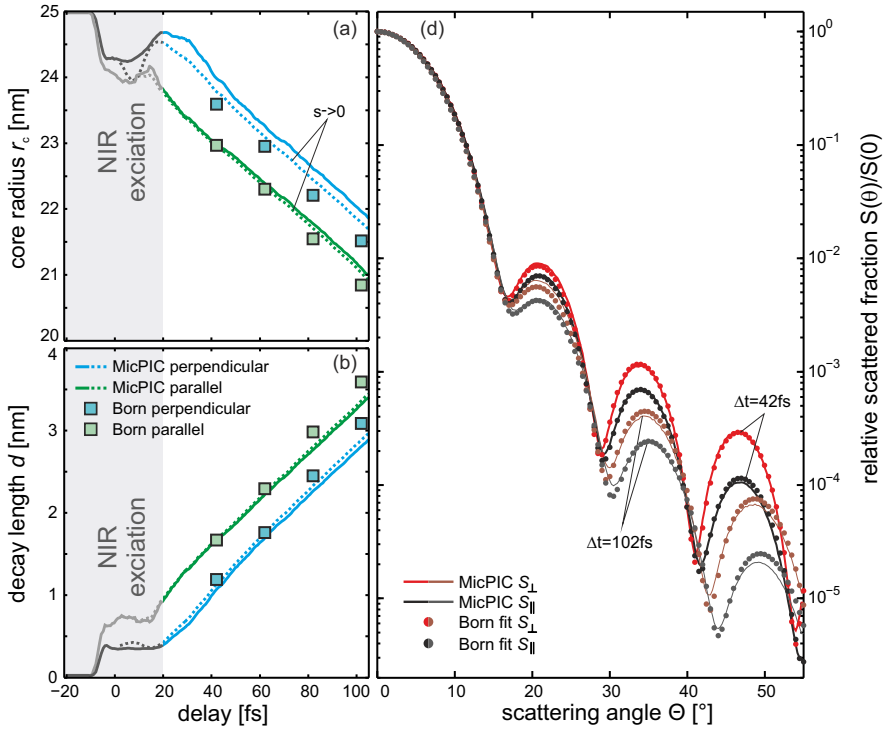

Figure 5.7.: (a)(c) Time evolution of density profile parameters; lines correspond to direct fits of the MicPIC density for directions parallel to (green) and perpendicular to (blue) the polarization direction using all parameters (solid) or the sharp edge limit $s \to 0$ (dashed); squares denote parameters reconstructed from the scattering pattern in the sharp edge limit (see text). (d) Full NIR-polarization dependent MicPIC scattering pattern (solid lines) and corresponding Born fits (circles) for two delays (as indicated). Published in [86].

these results prove that the proposed reconstruction method enables direct dynamic imaging of the plasma expansion dynamics from experimental data. Note that the only remaining free parameter, the actual core density n_c, can, at least in principle, be extracted from the inelastic scattering spectrum. A detailed discussion regarding the description and evaluation of the inelastic scattering will be given in section 5.4.

5.3. A dissipative oscillator model to describe atomic polarization and photoionization

In the pump-probe scenario discussed above, the cluster was completely inner ionized prior to the x-ray probe pulse. Consequently, it was not needed to include scattering from bound electrons. So far, according to the description given in chapter 2, neutral atoms do not carry any charges, cannot be polarized, and are therefore not visible to the FDTD part of MicPIC. However, to enable MicPIC to model medium polarization and the interaction of initially neutral clusters with short wavelength radiation, the scattering from the bound electrons has to be taken into account. Furthermore, for such a scenario, a convenient way has to be found to include single photon ionization

and the corresponding attenuation of the incident laser field. To this end, the action of bound electrons is emulated by a classical damped harmonic oscillator model, whose parameters are tuned to reproduce the atomic scattering and absorption properties. This section discusses the basic idea and its implementation.

5.3.1. The harmonic oscillator model

A convenient way to express the scattering and absorption properties of atoms or electrons are corresponding cross sections, which are defined as the ratio of the average power radiated/absorbed and the incident power per unit area (the laser intensity)

$$\sigma_{sca/abs} \equiv \frac{P_{sca/abs}}{I}. \tag{5.8}$$

For the case of free electrons, these quantities can be calculated analytically[3] [92] and yield

$$\sigma_{\mathrm{abs}}^{\mathrm{free\,el.}} = 0 \tag{5.9}$$

for the absorption cross section and

$$\underbrace{\sigma_{\mathrm{sca}}^{\mathrm{free\,el.}}}_{\sigma_{\mathrm{T}}} = \frac{8\pi}{3} r_{\mathrm{e}}^2. \tag{5.10}$$

for the scattering cross section, where $r_{\mathrm{e}} = e^2/4\pi\varepsilon_0 m_e c^2$ is the classical electron radius. The expression for the scattering cross section is also referred to as the Thomson cross section, first obtained by J.J. Thomson in 1906 [93]. The vanishing absorption cross section for free electrons reflects their inability to absorb light from spatially homogeneous light fields[4].

To derive corresponding expressions for an atom with multiple bound electrons, a semi-classical model can be applied where each electron contained in the atom is described by an independent damped harmonic oscillator

$$m\frac{\partial^2 \mathbf{r}}{\partial t^2} + \gamma m \frac{\partial \mathbf{r}}{\partial t} + m\omega_s^2 \mathbf{r} = -e(\mathbf{E}_{\mathrm{inc}} + \underbrace{\mathbf{v} \times \mathbf{B}_{\mathrm{inc}}}_{\simeq 0}), \tag{5.11}$$

where ω_s is the respective resonance frequency, γ a damping factor that accounts for energy loss and $\mathbf{E}_{\mathrm{inc}}$ and $\mathbf{B}_{\mathrm{inc}}$ are the incident electric and magnetic fields. The magnetic field term is negligible for small oscillation velocities. The resulting scattering and absorption cross sections[5] are then given by

$$\sigma_{\mathrm{abs}}^{\mathrm{atom}} = \frac{e^2}{\varepsilon_0 m\, c} \frac{\Im(f(\omega))}{\omega} \tag{5.12}$$

[3] in the non-relativistic limit and without intensity gradients of the field

[4] This conclusion is the essence of the well known Lawson-Woodward criterion, which holds even in the relativistic regime.

[5] A detailed derivation of the cross sections can be found in [92].

and

$$\sigma_{\mathrm{sca}}^{\mathrm{atom}} = \sigma_{\mathrm{T}} \left| f(\omega) \right|^2 . \tag{5.13}$$

Here, $f(\omega)$ denotes the atomic scattering factor, which describes the electric field amplitude of the wave scattered by the atom relative to that scattered by a free electron[6]. For a multi-electron atom of atomic number Z and in the limit of a wavelength much larger than the Bohr radius, the scattering factor is given by

$$f(\omega) = \sum_{s=1}^{Z} \frac{\omega^2}{(\omega^2 - \omega_{\mathrm{s}}^2) + i\gamma\omega}. \tag{5.14}$$

This atomic scattering factor has been determined experimentally for and is tabulated over a wide range of elements and photon energies [94]. This circumstance can be utilized to reproduce the measured x-ray properties by an appropriate choice of the harmonic oscillator parameters.

5.3.2. Adapting the harmonic oscillator model to hydrogen

To start with a system as simple as possible, the harmonic oscillator model is first applied to the hydrogen atom. As hydrogen has only one electron, the sum over all electrons drops and equation (5.14) reduces to

$$f(\omega) = \frac{\omega^2}{(\omega^2 - \omega_{\mathrm{s}}^2) + i\gamma\omega}. \tag{5.15}$$

As a result, a total of three free parameters is available to tune the scattering and absorption cross section obtained from the semi-classical model to the experimentally determined ones. The free parameters are, the resonance frequency ω_{s}, the damping factor γ and the effective mass of the electron m. The charge of the electron cannot be modified, as the remaining proton should still be perfectly screened when the electron is not displaced.

Tabulated scattering and absorption cross sections for hydrogen are shown in figure 5.8 as orange curves [94]. Unfortunately, it is not possible to fit the semi-classical model to the experimental data over the whole photon energy range, instead the parameters are chosen such that the values around the considered excitation photon energy (in this case 124 eV) fit best. Further, it has to be taken into account that the individual harmonic oscillators are driven by the electromagnetic fields on the FDTD grid. To prevent unphysical absorption of electromagnetic fields created by the regular plasma dynamics, it has to be ensured that the absorption cross section in the low frequency regime is as small as possible. The resonance frequency ω_{s} has been chosen to fit both requirements best. The final parameters and the resulting absorption and scattering cross sections for the oscillator model are also shown in figure 5.8.

[6]For the derivation of $f(\omega)$ a complex incident field of the form $\mathbf{E} = \mathbf{E}_0 e^{-i\omega t}$ is considered, see [92].

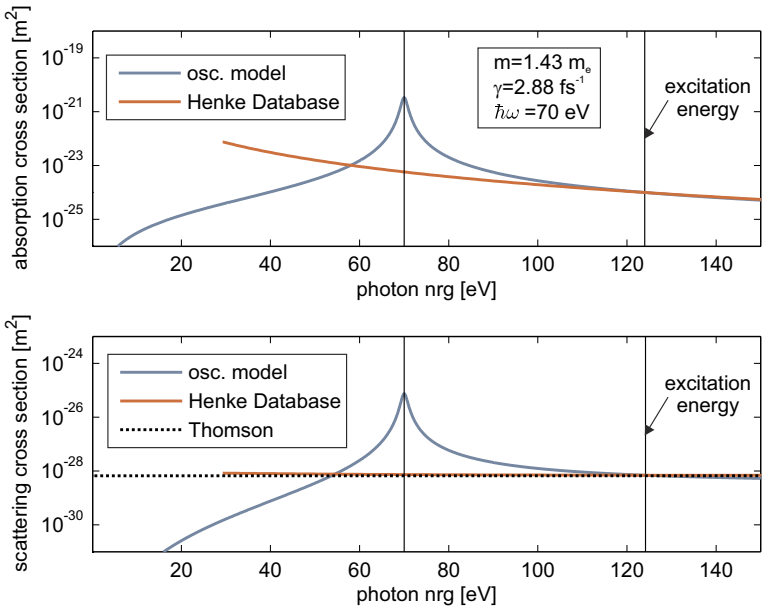

Figure 5.8.: Absorption and scattering cross sections for hydrogen as determined experimentally (orange) and theoretically for the semi-classical harmonic oscillator model.

5.3.3. Photoionization

Finally, the discussed harmonic oscillator model can be utilized to implement single photon ionization into MicPIC. A convenient way to implement photoionization in particle based semi-classical models is to evaluate corresponding ionization rates in terms of a Monte-Carlo scheme. The ionization rate at a given point in time is then determined by the photoionization cross section σ_{abs}, the instantaneous field intensity I and the respective photon energy $\hbar\omega_{\mathrm{pho}}$ according to

$$\Gamma = \frac{\sigma_{\mathrm{abs}} I}{\hbar\omega_{\mathrm{pho}}}. \tag{5.16}$$

However, in MicPIC all electromagnetic fields including the fields generated by the plasma particles, possibly generated harmonics or even two-color pulses are propagated on the same numerical grid. Since FDTD is a time-domain method, the spectral composition of these fields is not known at run time. Therefore, the relevant field intensity at the considered photon frequency in equation (5.16) can not be directly determined. At this point the definition of the absorption cross section in equation (5.8) becomes useful. Inserting it into equation (5.16) yields an expression for the ionization rate that only depends on the instantaneous absorbed power

$$\Gamma = \frac{P_{\mathrm{abs}}}{\hbar\omega_{\mathrm{pho}}}. \tag{5.17}$$

The power absorption of the i-th particle follows directly from the dissipative term in equation (5.11) and reads

$$P_{\mathrm{abs,i}} = \gamma m \dot{\mathbf{r}}_{\mathrm{i}}^2. \tag{5.18}$$

The resulting instantaneous photoionization rate can then be evaluated for each individual atom via Monte Carlo methods. If the photoionization event is successful, the oscillator force (5.11) for the corresponding electron is switched off and the electron is treated as a regular plasma electron with an initial kinetic energy determined by the photoionization excess energy $E_{\mathrm{exc}} = \hbar\omega - E_{\mathrm{B}}$.

To test the corresponding MicPIC photoionization routine, the excitation of an initially neutral $R = 25\,\mathrm{nm}$ hydrogen cluster at solid density by a single 10 fs soft x-ray pulse ($\hbar\omega = 124\,\mathrm{eV}$) at intensity $5 \times 10^{16}\,\mathrm{W/cm^2}$ is considered. Figure 5.9 shows the time evolution of selected system energies and the average inner ionization state with contributions from electron impact- and photoionization.

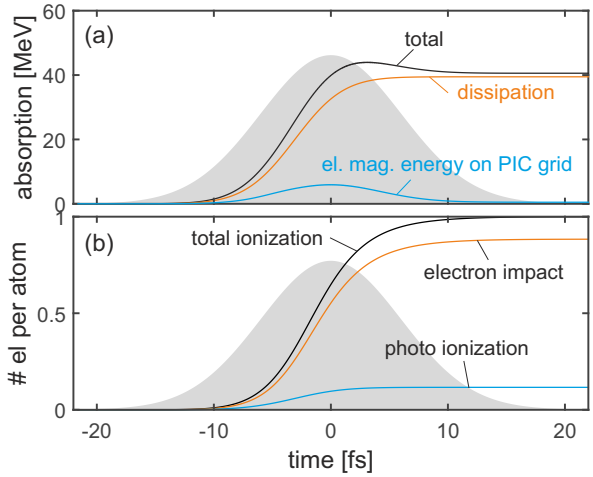

Figure 5.9.: (a) Time evolution of the selected system energies – as indicated– and (b) the contributions of electron impact- and photoionization to the average inner ionization state during and after the excitation of an $R = 25\,\mathrm{nm}$ hydrogen cluster at solid density excited by a single 10 fs soft x-ray pulse at intensity $5 \times 10^{16}\,\mathrm{W/cm^2}$.

Plasma generation is triggered by photoionization events in the leading edge of the pulse. In contrast to the NIR excitations discussed so far, these electrons cannot be efficiently heated by the laser pulse as inverse bremsstrahlung heating is negligible in this wavelength regime. Instead the energy input is determined by the excess energy of the photoionized electrons, which is also referred to as ionization heating [95]. Though the excess energy is relatively high ($E_{\mathrm{exc}} \simeq 110\,\mathrm{eV}$), only a few hundred plasma electrons can leave the cluster before the space charge potential of the remaining cluster gets deep enough to trap them, an effect called frustrated photoionization [95, 96]. As a result, the trapped electrons collide continuously with the cluster atoms which drives electron impact ionization that eventually contributes about 90% of the ionization events, c.f. figure 5.9b. The fact that the total energy absorption of the system is dominated by the dissipative force term in equation (5.11) (compare black and orange curves in figure 5.9a) confirms that inverse bremsstrahlung does not play a role here[7]. The deviations of dissipative and total energy around the pulse maximum can

[7]The energy absorption due to the dissipative force term is evaluated by integration of the corresponding power absorption given in equation (5.18) and summation over all particle contributions.

be attributed to the scattered and radiated electromagnetic fields on the PIC level in the simulation box.

5.4. Inelastic x-ray scattering

So far, the discussion was focused on the description of elastic x-ray scattering and how it can be utilized to derive structural information on the system in pump-probe and x-ray only excitation scenarios. The last part of this chapter concentrates on the evaluation of the corresponding inelastic contributions to the x-ray scattering and the additional information it can provide.

Figure 5.10 shows the angular resolved (b) and averaged (a) spectral intensity of the scattered electric fields for the pump-probe study discussed in section 5.2. In this scenario the cluster is already fully inner ionized by the NIR pump pulse. The data shown here corresponds to the run with a pulse delay of $\Delta t = 42\,\mathrm{fs}$. Two main features can be observed from the angular-resolved data: (i) A strong signal with pronounced interference fringes at the excitation energy of the x-ray pulse $\hbar\omega = 124\,\mathrm{eV}$ which corresponds to the elastically scattered signal that was already discussed. And (ii), two symmetric satellites of much lower intensity that do not exhibit interference fringes. These satellites result from the coupling of the incident x-ray light with longitudinal volume plasmon excitations that exist as part of the thermal electron density fluctuations. Raman-type scattering at this collective electron motion imprints an additional modulation on the scattered field that creates the satellites. The spectral plasmon satellites are an important diagnostic tool in plasma x-ray Thomson scattering [50, 51] as they provide a sensitive method to measure the plasma electron density. In a simplified picture – neglecting temperature effects in the Bohm-Gross dispersion relation – the position of the satellites is determined by the plasma frequency

$$\omega_{\mathrm{pl}} = \sqrt{\frac{e^2 n_{\mathrm{e}}}{m_{\mathrm{e}} \varepsilon_0}}, \tag{5.19}$$

and only depends on the density of plasma electrons. For the shown data, the spectral shift of the peaks matches the volume plasmon ernergy $\hbar\omega_{\mathrm{pl}} = 7.6\,\mathrm{eV}$ that corresponds to fully ionized hydrogen at the initial cluster density. Together with the scheme given in section 5.2, the determination of the position of the plasmon peaks allows the complete reconstruction of the plasma density evolution. However, the inelastic signal is orders of magnitude smaller when compared to the elastic signal. Therefore, averaging over multiple laser shots might be necessary to determine the peak position in an experiment.

Figure 5.11 shows a corresponding spectral analysis of the x-ray scattering for the x-ray only excitation including photoionization discussed in the last chapter. The major difference to the pump-probe spectra is the absence of pronounced satellites. Instead a plateau like structure is observed in the averaged spectrum that extends from the lower to the upper expected peak position. This can be attributed to the fact that for the x-ray only scenario the excitation starts with a neutral cluster where the plasma

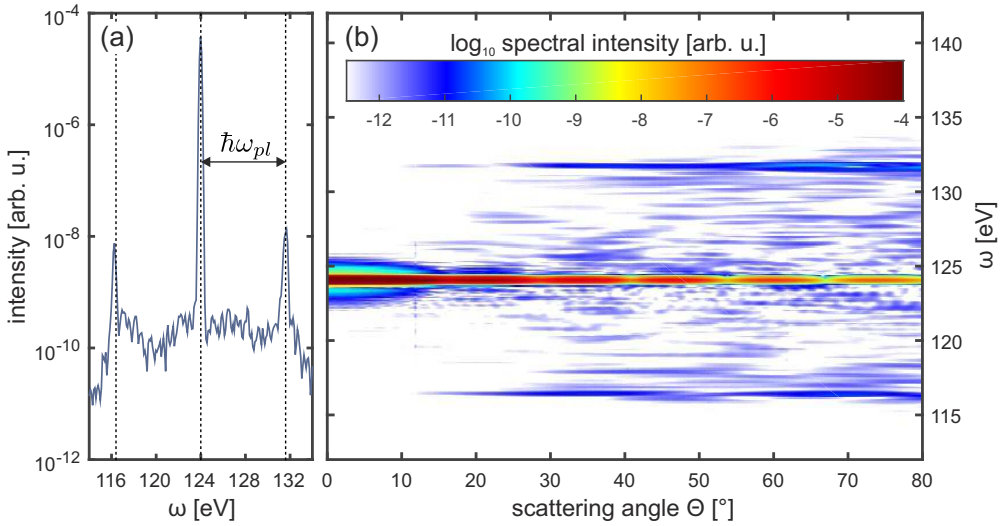

Figure 5.10.: Scattered x-ray intensity spectra resulting from the NIR pump / x-ray probe excitation of an $R = 25\,\mathrm{nm}$ hydrogen cluster described in section 5.2 for a pump probe delay of $\Delta t = 42\,\mathrm{fs}$. Panel (b) shows the angular resolved intensity spectrum and panel (a) the corresponding signal averaged over the large angle region with $60° < \Theta < 90°$.

is building up during the pulse. Therefore the plasmon frequency changes during the pulse, shifting the peak position gradually to the value of $\hbar\omega_{\mathrm{pl}} = 7.6\,\mathrm{eV}$ for complete inner ionization once full ionization is achieved close to the end of the pulse (compare with figure 5.9).

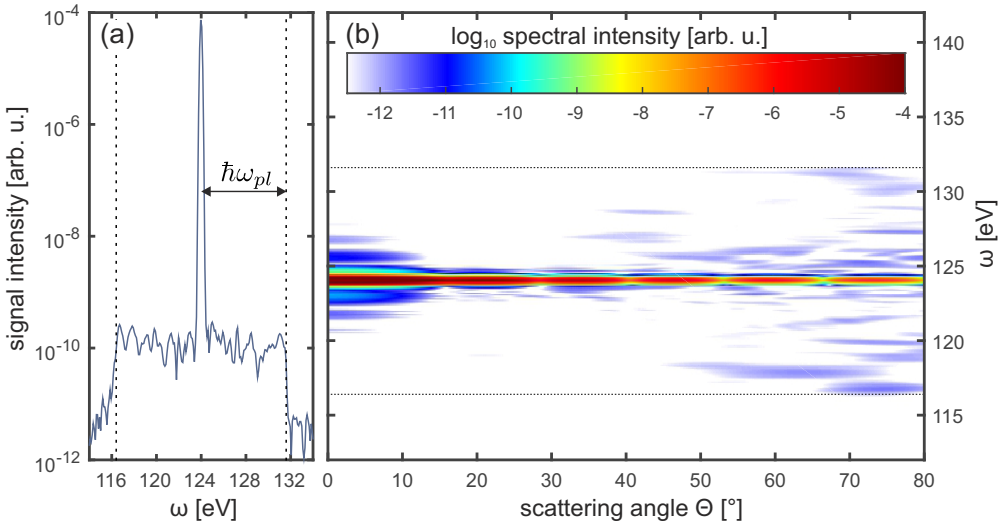

Figure 5.11.: Scattered x-ray intensity spectra resulting from the excitation of an $R = 25\,\mathrm{nm}$ hydrogen cluster at solid density with a single 10 fs soft x-ray pulse at intensity $5 \times 10^{16}\,\mathrm{W/cm^2}$. Panel (b) shows the angular resolved intensity spectrum and panel (a) the corresponding signal averaged over the large angle region with $60° < \Theta < 90°$.

6. The origin of highly charged atomic ions from x-ray laser-cluster interactions

One of the main open questions that has been debated intensely in the cluster community during the last years is the origin of the observed extremely high charged atomic ions from clusters after excitation with intense laser fields [24, 26, 97]. While it is well accepted, that such highly charged ions can exist as part of the generated cluster nanoplasma, it is still not fully understood how exactly these high inner charge states are transformed into outer ionization charge states that can be recorded in an experiment [96, 98]. The main difficulty arises from the fact that independent of the excitation regime, only a relatively small number of electrons can leave the cluster during the laser excitation due to the space charge potential of the remaining positively charged cluster.

In this chapter the formation of the final charge spectra is studied for cluster excitation in the hard x-ray regime where sequential emission of photo- and Auger electrons are the dominant laser driven ionization processes. In this regime heating through inverse bremsstrahlung is negligible and the energetics of plasma electrons is governed by ionization heating [95], i.e. by the excess energy of photo- and Auger electrons. A schematic illustration of the typical laser cluster interaction dynamics in this regime is given in figure 6.1. Direct photoemission of the first electrons into the continuum creates a positively charged cluster, due to the resulting space charge potential subsequently emitted electrons experience a continuous Coulomb shift to lower energies with increasing cluster charge. At a certain ionization stage, the space charge potential is deep enough to frustrate further direct ionization and additionally liberated electrons are trapped in the cluster, building up a localized nanoplasma. The excess energy of the trapped photo- and Auger electrons is then redistributed by collisions, inducing electron emission via thermal evaporation and possibly additional electron impact ionization. Finally, the cluster expands due to Coulomb repulsion of the ions and hydrodynamic forces.

To measure the resulting charge state distributions in cluster experiments, typically time-of-flight (TOF) setups are applied, where the different ionic charge states are separated in flight time by an external electric DC-extraction field. To achieve a sufficient signal to noise ratio, cluster jets of relatively high density are used in most experiments (especially for smaller clusters with only a few hundred or thousand constituents), such that multiple clusters are hit by every laser pulse. Since both, the laser pulse as well as the cluster jet, have a nonzero transverse elongation and the cluster sizes itself follow a

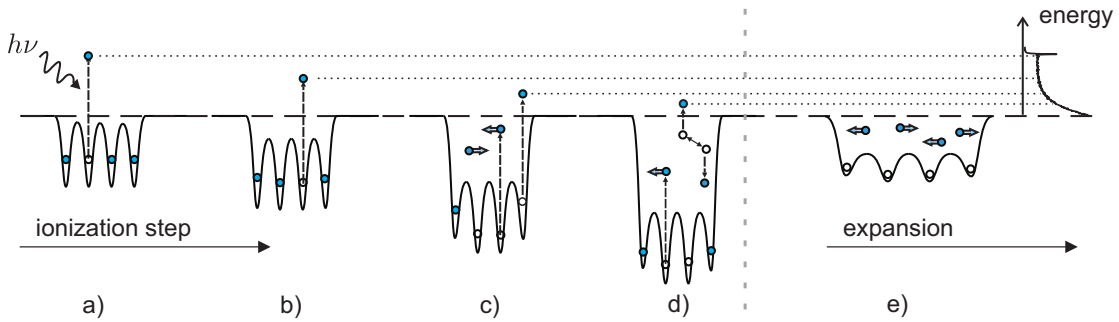

Figure 6.1.: Schematics of the cluster ionization dynamics in intense shortwavelength laser pulses based on the effective cluster potential. After direct photoemission of the first electron (a), subsequently emitted photoelectrons experience a continuous Coulomb downshift with increasing cluster charge (b). This multistep ionization becomes frustrated at a certain ionization stage and nanoplasma formation sets in (c). Collisions between trapped electrons induce evaporation electron emission (d). Finally, the cluster expands due to charging and hydrodynamic forces (e). From reference [99].

size distribution, the measured spectra always reflect an accumulated signal averaged over different laser intensities and cluster sizes. This complicates a theoretical description and more importantly, it obscures possible size- and intensity dependent features in the spectra. However, the growing availability of free-electron laser facilities like Flash in Hamburg or LCLS in Stanford opened up the opportunity for a new type of combined experiment that circumvents the above problems. Using low intensity cluster beams, such that only a single cluster is hit by the laser pulse and simultaneously recording x-ray scattering images together with the TOF spectra allows to determine the corresponding cluster size and laser intensity on a shot to shot basis.

A first experiment of this kind has been performed by Gorkhover *et al.* [47] at the LCLS free-electron-laser in Stanford, where relatively large Xenon clusters ($R \simeq 30\,\mathrm{nm}$) have been irradiated by intense 130 fs x-ray pulses at 800 eV photon energy. The experimental setup and selected results for clusters of radius $R \simeq 30\,\mathrm{nm}$ hit by different laser intensities are shown in figure 6.2. For the highest laser intensity (case a: $10^{16}\,\mathrm{W/cm^2}$) the measured ion yield is maximal for charge states around $q = 26^+$ and no charge states below $q = 4^+$ are observed. For clusters hit by a 10 times lower intensity (b), the charge state distribution is shifted to significantly lower charge states, but still shows no prominent peak for singly charged ions. Only if the intensity is lowered by more than two orders of magnitude, singly charged ions show up and dominate the spectrum (c). The fact that the focal volume averaged results shown in the bottom panel of figure 6.2 are heavily dominated by singly-charged ions illustrates the inability of conventional cluster TOF experiments to disentangle the respective intensity contributions and the connected loss of information.

The observed average charge state of $q_{avg} \simeq 26^+$ for the highest intensity seems to be extremely high considering the fact that direct outer ionization should be frustrated at a very low average outer ionization stage. To estimate the critical average charge state for complete frustration, the cluster can be approximated as a homogeneously charged sphere. Full frustration is assumed as soon as the potential at the cluster surface is

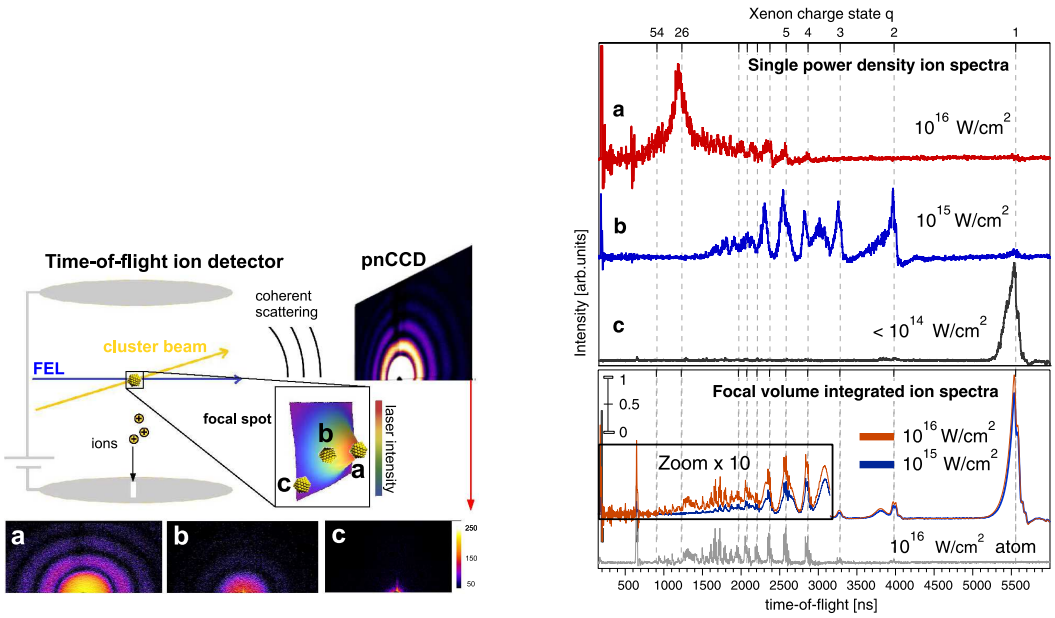

Figure 6.2.: Left: Experimental x-ray scattering setup for measurements at the LCLS free electron laser performed by Gorkhover *et al.*, single large Xenon clusters have been irradiated by intense single x-ray pulses at 800 eV photon energy. The scattering signal is recorded on a shot to shot basis and used afterwards to estimate the laser intensity at the cluster position in the FEL focus. Right top panels: Single shot ion spectra recorded in coincidence with the scattering images at the left side (as indicated). Bottom panel: Focal volume integrated ion yield spectra for cluster (top) and atomic (bottom) targets. From reference [47].

deeper than the photon energy. The resulting condition reads

$$\frac{e^2}{4\pi\varepsilon_0}\frac{N\, q_{frust}^{avg}}{R} = \hbar\omega, \tag{6.1}$$

with N the number of Xenon ions and R the cluster radius. Inserting the corresponding values from the experiment results in a critical average charge state of $q_{frust}^{avg} = 0.01$, which is more than a factor of 1000 lower than the observed charge states. Approaching the problem from a different angle, one can also estimate the electrostatic energy that is stored in such a configuration and thus has to be absorbed from the x-ray pulse. The self-energy of a homogeneously charged sphere can be calculated from

$$E_{self} = \frac{q_{\text{avg}}^2}{4\pi\varepsilon_0}\frac{3}{5}\frac{N^{5/3}}{r_s}, \tag{6.2}$$

with r_s being the Wigner-Seitz radius. Again inserting the values corresponding to the experimental conditions ($r_s = 2.6\,\text{Å}$ for solid density Xenon) yields an energy of 33 MeV per atom. The upper limit for the expected energy absorption per atom can be estimated from

$$E_{\text{abs}} = I_0 \tau \sigma, \tag{6.3}$$

where I_0 the peak laser intensity, τ the pulse length and σ the photoionization cross section[1] and yields an absorption of $E_{\text{abs}} = 22\,\text{keV}$ per atom which is again more

[1]The photoionization cross section for neutral Xenon at 800 eV photon energy is $\sigma = 2.7\,\text{Mb}$ [94]

than a factor of 1000 too small. Together, these considerations clearly show that the extremely high average charge states observed in the experiment can by no means be explained by outer ionization on the time scale of the x-ray pulse where the cluster is still at or near solid density.

In the remainder of this chapter, it will be shown that the expansion stage after the laser excitation is key to understand the experimentally observed behavior. The cluster expansion transforms the initially highly excited nanoplasma into an ultracold Rydberg plasma on the time scale of a few hundred picoseconds, with corresponding electron binding energies in the range of only a few meV. At this stage, the DC extraction fields used in TOF measurements to separate different ionic charge states are sufficient to reionize the Rydberg-like electrons. Taking these extraction fields into account in the simulation yields final charge spectra that show the same features and characteristic intensity dependence as the experimental data and therefore strongly suggest that the detection method itself has a major influence on the measured charge spectra.

6.1. Modeling the interaction of hard x-ray radiation with clusters via Molecular Dynamics simulations

Modeling the x-ray excitation process as well as the subsequent cluster expansion on the picosecond to nanosecond time scale requires to track electron and ion positions over a spatial range that is far outside of what can be handled with a grid based method like MicPIC. Consequently, a gridless Molecular dynamics approach is applied for that task here[2]. In the MD model, plasma particles (ions and electrons) are propagated classically under the influence of mutual Coulomb interactions while particle motion due to the electric field of the x-ray pulse can be neglected due to the small quiver amplitude at this frequency. The coupled equations of motion read

$$m_i \ddot{\mathbf{r}}_i = \nabla_{\mathbf{r}_i} \sum_{i \neq j} V_{ij}, \tag{6.4}$$

where m_i and $\mathbf{r}_i$ are the mass and position of the ith plasma particle and V_{ij} is the pseudopotential for gaussian particles that is also applied in MicPIC. The numerical workload connected with the evaluation of the binary coulomb forces scales quadratically with the total particle number, which restricts the numerically feasible cluster size for the desired time scales to a few thousand atoms. For the calculations presented in this chapter, Xenon clusters with 1415 atoms in relaxed icosahedral geometry are considered. Plasma generation via tunnel- and electron impact ionization is implemented in terms of rate equations similar to the treatment in MicPIC. However, the dominant laser field driven ionization mechanisms in the hard x-ray regime are single photon ionization and possible subsequent Auger ionization. Both have to be described reasonably.

[2]The discussion given here addresses only methodical key aspects of the MD model. Further details on methodical details of the code can be found in the publications [24, 100].

The basic approach to implement the photoionization process into the MD model is much simpler than the implementation into MicPIC. Since the intensity of the x-ray pulse is known at all times, the corresponding photoionization rate can be directly calculated from

$$\Gamma = \frac{\sigma(\omega) I(t)}{\hbar\omega} \tag{6.5}$$

and evaluated within a Monte Carlo scheme for each individual atom/ion. The main challenge in implementing photoionization into the MD model arises from the fact that photoionization of already highly charged atomic ions has to be considered at the given laser parameters. As a result, the photoionization cross section also becomes a function of the current ion charge state since already liberated electrons can no longer contribute to the cross section. As experimental data for charge state resolved ionization cross sections could not be found, a simple model is developed on the basis of quantummechanical calculations from Verner *et al.* [101]. Calculated photon energy dependent total photoionization cross sections and the respective contributions from individual electronic shells are shown in figure 6.3a for Argon. Note that calculations for Xenon have not been available and Argon has been chosen as the closest rare gas representative to test the simplified scheme described below. Due to the similar electronic structure, the model developed here for Argon is assumed to be also applicable to Xenon later on.

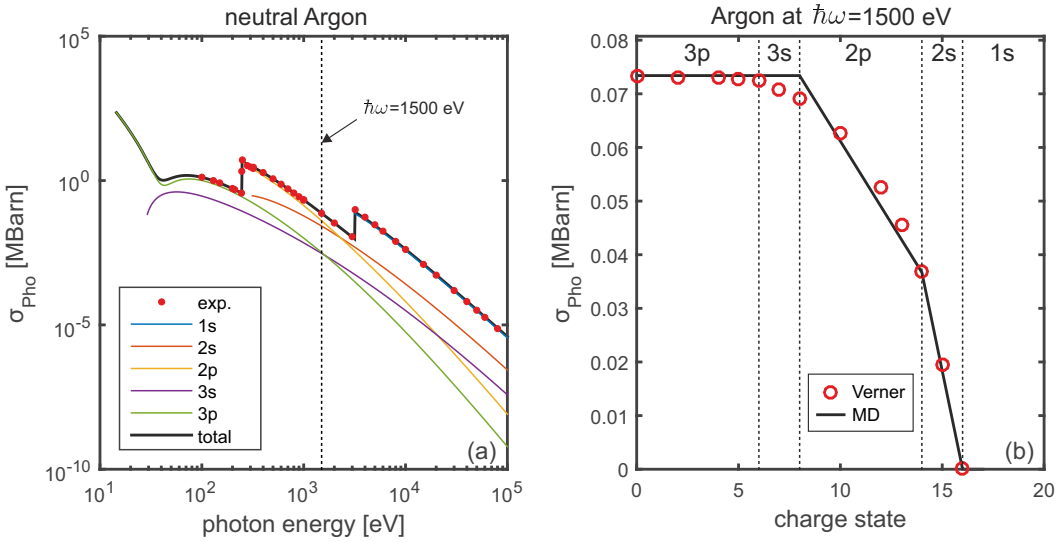

Figure 6.3.: (a) Total photoionization cross sections and contributions from individual electronic shells for Argon according to calculations from Verner *et al.* [101] (lines) and measured total cross sections from Veigele *et al.* [102] (symbols). (b) Total photoionization cross sections for Argon atoms as a function of the charge state calculated from the simplified model used in the MD simulation (lines) compared to the calculations from Verner *et al.* [101] (symbols). Vertical lines indicate the corresponding highest occupied electronic shell before the ionization process.

Analyzing the cross sections in figure 6.3a in more detail reveals that the largest contribution to the total cross section is always provided by the deepest reachable electronic shell. For a photon energy of 1500 eV, which is used later for the actual

calculations, the main contribution stems from the L shell, almost equally distributed between the 2s and 2p subshells. Translating this observation into a simple scaling law yields the following expression for the charge state dependent photoionization cross section

$$\sigma_{\mathrm{MD}}(\omega, q) = \sigma_0(\omega)\frac{1}{s}\sum_{i=1}^{s}\frac{N_{s,q}^{deep}}{N_{s,0}^{deep}}, \tag{6.6}$$

where $\sigma_0(\omega)$ is the respective total photoionization cross section for the neutral atom (which is tabulated over a wide range of elements and photon energies [94]), s is the number of contributing subshells and $N_{s,q}^{deep}$ and $N_{s,0}^{deep}$ denote the number of electrons occupying the corresponding subshell in the ground state of the charged ion and the neutral atom, respectively. The scaling law assumes that the total cross section $\sigma_0(\omega)$ is equally distributed between all s subshells of the deepest reachable electronic shell. The contribution of each individual subshell to the charge dependent cross section is then determined by its relative occupation with respect to the neutral atom. The resulting charge dependent total cross sections for Argon are compared to quantum mechanical calculations from Verner *et al.* [101] in figure 6.3b. Though the scaling law (eq. 6.6) is exceptionally simple, it reproduces the full calculations very well over the whole range of charge states.

Applying the same methodology to Xenon yields the desired charge state dependent ionization cross sections and thus provides an efficient way to calculate and evaluate the corresponding ionization rates for each individual atom/ion. In the MD model, a successful photoionization event leads to the creation of an additional plasma electron that is positioned on top of its mother ion with the proper excess energy and a randomized momentum direction. Since the deepest reachable electronic shell contributes most to the cross section, the released electron is always taken from the deepest subshell, which typically leaves an excited ion with a core hole behind. The proper treatment of possible relaxation pathways back to the ionic ground state is a highly non-trivial task. For simplicity, it is assumed that the lifetime of the excited state is short compared to all other relevant time scales and the hole is instantly filled with the weakest bound electron. If the corresponding energy gain is sufficiently high, the second weakest bound electron is released as an Auger electron under the constraint of energy conservation, otherwise instantaneous radiative relaxation is assumed.

6.2. Cluster excitation and expansion dynamics induced by intense x-ray excitation

As a first application of the adapted MD model, the excitation of a Xe_{1415} cluster by an intense 200 fs x-ray pulse at $\hbar\omega = 1500\,\mathrm{eV}$ photon energy and $10^{16}\,\mathrm{W/cm^2}$ peak intensity is considered. These excitation parameters have been chosen to be close to the ones applied in the experiment by Gorkhover *et al.* [47]. The higher photon energy is not expected to change the nature of the interaction, as for both energies single photon absorption dominates the laser-cluster interaction while inverse Bremsstrahlung is negligible.

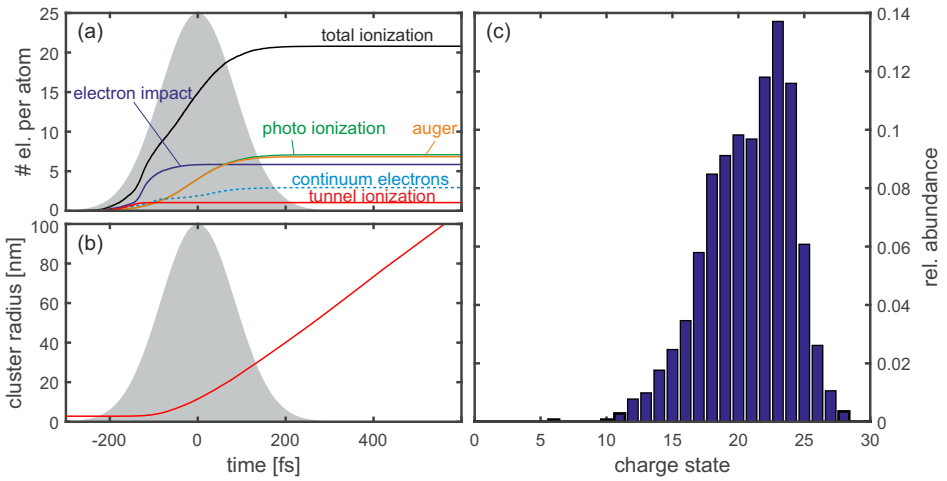

Figure 6.4.: Excitation of an Xe_{1415} cluster with a 200 fs x-ray pulse at $\hbar\omega = 1500\,\mathrm{eV}$ photon energy and $10^{16}\,\mathrm{W/cm^2}$. Panel (a) shows the time evolution of the average inner ionization state and the respective contributions from photo-, auger-, tunnel- and electron impact ionization. The time evolution of the cluster radius is shown in panel (b), and the resulting distribution of inner ionization charge states after the pulse is shown in panel (c).

The calculated time evolution of inner ionization and cluster expansion during and shortly after the excitation pulse is shown in figure 6.4a and 6.4b, respectively. The following conclusions can be drawn from the simulation results: Plasma formation starts in the leading edge of the pulse with first photo- and Auger- ionization events. At this stage, the excess energy of both, photo- and Auger- electrons is sufficiently large to directly leave the cluster. However, the quickly increasing net charge of the remaining cluster generates a space charge potential that prevents further direct ionization. The resulting increasing number of trapped plasma electrons induces an electron impact ionization avalanche, see dark blue curve in figure 6.4a around $-100\,\mathrm{fs}$. The efficiency of electron impact ionization quickly decreases again with increasing average inner charge state due to the increasing binding energies of the remaining bound electrons. The same applies to tunnel ionization that occurs in the early stages due to the strong electric fields induced by the space charge potential at the cluster surface. Eventually, even the energy gain by hole relaxation is not sufficiently high and only photoionization remains as active ionization channel. The beginning of this stage is indicated by the fact that a slightly higher contribution from photoionization is observed when compared to Auger ionization. At the end of the pulse, an average inner charge state of $q = 21^+$ is reached, but only about 3 electrons per atom exhibit a positive single-particle-energy and can actually leave the cluster, c.f. black and dotted blue curve in figure 6.4a. Note that the frustration limit for direct outer ionization is much higher here when compared to the considerations in the beginning of the chapter due to the much smaller cluster size. The resulting Coulomb repulsion drives a very fast expansion, such that the cluster radius is increased by more than a factor of 10 by the end of the pulse, c.f. panel (b).

The distribution of the final inner charge states is displayed in figure 6.4c. It already shows features very similar to the experimental observations, with an average charge

state above $q = 20^+$ and no charge states below $q = 5^+$. However, taking into account that 400 fs after the pulse 85% of the liberated electrons remain trapped in the cluster potential shows that the inner ionization state is not necessarily representative for the final charge states.

Figure 6.5 shows the evolution of inner and outer ionization on a much longer time scale. During the first few hundred picoseconds, autoionization increases the number of continuum electrons significantly from 3 to about 5 electrons per atom. Nevertheless, at the end of the simulation 75% of the generated plasma electrons are still bound to the decaying cluster, which indicates that a more in depth analysis is needed to understand the origin of the experimental observations.

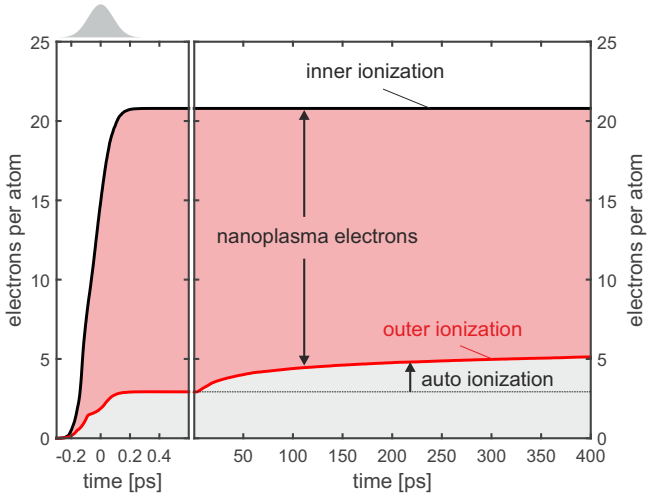

Figure 6.5: Time evolution of average inner and outer ionization during and after the hard x-ray excitation. The colored area highlights the difference between inner and outer ionization, i.e. the fraction of electrons that forms the nanoplasma. The increase of outer ionization after the x-ray pulse can be attributed to autoionization. Parameters as in figure 6.4.

So far, liberated electrons have been distinguished only in terms of the sign of their single-particle-energy (E_{sp}). Electrons with $E_{\mathrm{sp}} > 0$ can overcome the space charge potential and eventually leave the cluster, electrons with $E_{\mathrm{sp}} < 0$ are trapped in the cluster potential. In the following, the effect of the cluster expansion on the actual energy distribution of the plasma electrons is analyzed in more detail. Calculated single-particle-energy spectra (with respect to the global continuum) are shown in figure 6.6 (a-c) for different time and energy scales. Panel (a) shows the early stages of the expansion phase. During the first picoseconds of expansion the energy distribution of electrons with $E_{\mathrm{sp}} < 0$ is rapidly shifted towards lower binding energies, reflecting the lowering of the cluster potential due to the expansion. After about 1 ps the distribution splits into two contributions. A broad distribution around $E_{\mathrm{sp}} \simeq -150\,\mathrm{eV}$ and a narrow distribution close to the continuum ($E_{\mathrm{sp}} \leq 0$) that keeps shifting to lower binding energies, leading to an average binding energy of only a few meV at the end of the simulation, see panels b and c in figure 6.6. To allow for an unambiguous classification of these cluster electron contributions, the trivial effect of the cluster potential evolution needs to be removed from the single-particle-energy spectra. To this end, corresponding local single-particle-energy spectra have been calculated, where the energy is not measured with respect to the global continuum but the local quasi-continuum threshold, i.e. the potential barrier between neighboring ions. To estimate the quasi-continuum threshold, each electron bound to the cluster is assigned to its

closest ion. The local barrier V_{loc} is then approximated by the potential halfway in between this ion and its nearest neighbor ion. The local single-particle energy is then given by

$$E_{sp}^{\mathrm{loc}} = E_{sp} - V_{\mathrm{loc}}. \tag{6.7}$$

The resulting local single-particle energy spectra shown in figure 6.6(d-f) are now effectively free from the trivial effect of the cluster potential. In the early stages (panel (d)), again the rapid formation of a broad distribution around $E_{\mathrm{sp}} \simeq -150\,\mathrm{eV}$ is observed. This feature can now be assigned to localized electrons, i.e. electrons that have been captured by an ion after the collision with one or more other electrons. Due to the high local binding energies, these electrons are likely to be permanently bound. The second feature is a strong but narrow distribution slightly above the local continuum threshold which can be attributed to delocalized cluster electrons. As these electrons remain mobile within the decaying cluster, the contribution narrows continuously due to further expansion cooling.

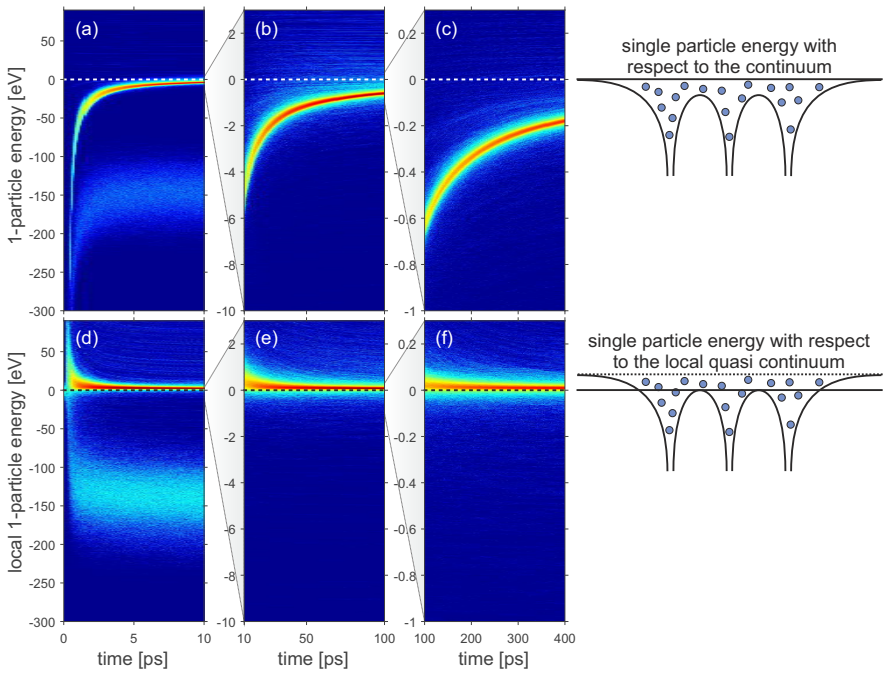

Figure 6.6.: Nanoplasma dynamics in terms of single-particle energy spectra of the electrons with respect to the continuum threshold (a-c) or the local quasi-continuum (d-f). The schematics in the right part of the figure illustrate the respective continuum threshold. Note that the panels show smaller energy ranges over longer time scales from left to right. Parameters as in figure 6.4.

To further characterize the expansion cooling, average kinetic energies of the delocalized electrons have been calculated in the lab frame and the frame of the respective closest ion. The results plotted in figure 6.7 show that the cooling dynamics can be divided into two stages. In the early stage (up to about 2 ps), the temperature decreases as t^{-2} before the behavior changes and the cooling slows down to a $\propto t^{-1}$ scaling. It turns out that the changing cooling dynamics can be attributed to the transition from a weakly coupled to a strongly coupled plasma. Shortly after the excitation, the av-

erage kinetic energy of the electrons is much higher than the average potential energy associated with electron-electron interactions. It is important to note, that only the correlation part is of interest here as the mean-field term is effectively screened by the ionic background. In this regime the electrons are weakly coupled and the ionic background mainly acts as a container[3]. As a result, the cluster expansion driven cooling proceeds similar to that of an ideal gas with no internal degrees of freedom under adiabatic expansion conditions, which yields an electron temperature proportional to $\propto t^{-2}$. At this stage the kinetic energy decreases faster than the potential energy ($\propto t^{-1}$) such that both will eventually be of the same order of magnitude. This characterizes the beginning of the strong coupling regime where particle-particle interactions become important. Taking particle-particle interactions into account classically by means of the virial theorem yields an electron temperature scaling proportional to $\propto t^{-1}$ [103] [4]. The fact that the actual temperature decrease for the later stages is slightly stronger ($\propto t^{-1.13}$) indicates that not all phase space areas are strongly coupled. A more detailed derivation of the temperature scaling for weakly and strongly coupled plasmas is given in the appendix A.

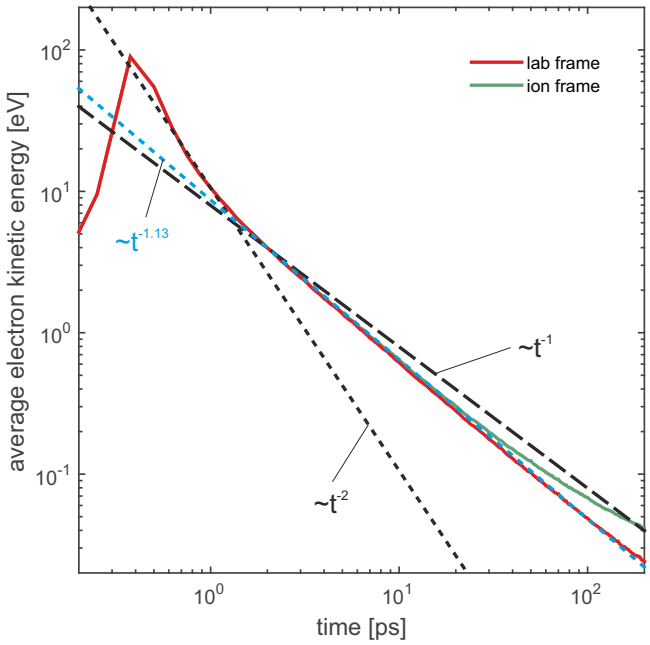

Figure 6.7: Time evolution of the average kinetic energy of delocalized electrons, i.e. electrons with a global single-particle-energy < 0 and a local single-particle-energy > 0. The temperature decay shows two stages with a different decay behavior. For comparison curves that correspond to a linear or quadratic temperature decrease are also shown. A fit of the long term evolution yields a decay behavior that scales as $t^{-1.13}$, c.f. blue dashed curve. The departure of the curves calculated in the lab and ion frame for longer times indicates the region where electrons are cooled down to temperatures where the relative velocities are on the order of the ion velocities, c.f. red and green curve. Parameters as in figure 6.4.

Concentrating on the single-particle-energies again: A quantitative analysis of the single-particle-energy electron distributions (E_{sp} and E_{sp}^{loc}) after 400 ps of cluster expansion is provided in figure 6.8. Panel (a) shows the distributions over the whole relevant energy range with pronounced peaks for the localized and delocalized electrons. The corresponding integrated signal plotted in panel (b) shows that only about 25% of the electrons are permanently relocalized while the major fraction (about 60%)

[3]For the following estimates the cluster is assumed to expand homogeneously. The cluster radius evolution $R(t)$ is determined by a constant radial velocity of the outermost ions ($v_{\mathrm{i}} = const.$) according to $R(t) = R_0 + v_{\mathrm{i}}t$.

[4]Note that the virial theorem assumes that the system is bounded, i.e. the particle momenta and positions are finite.

of the electrons is energetically located close to the continuum threshold. Zooming in to the continuum threshold region (see panels (c) and (d)) reveals that the distribution of the delocalized electrons has narrowed down to a width of only a few meV with binding energies of also only a few meV. These weakly bound electrons are likely to be affected by relatively weak electric fields, as the ones used for charge state separation in experimental TOF measurements. At this point it should be mentioned that the idea of a significant influence of these fields on the dynamics of highly excited cluster electrons has been first proposed and investigated for NIR-excitations [24]. However, the single-shot single-cluster experiments from Gorkhover *et al.* [47] provide an important reference measurement for a detailed theoretical analysis that was not available so far.

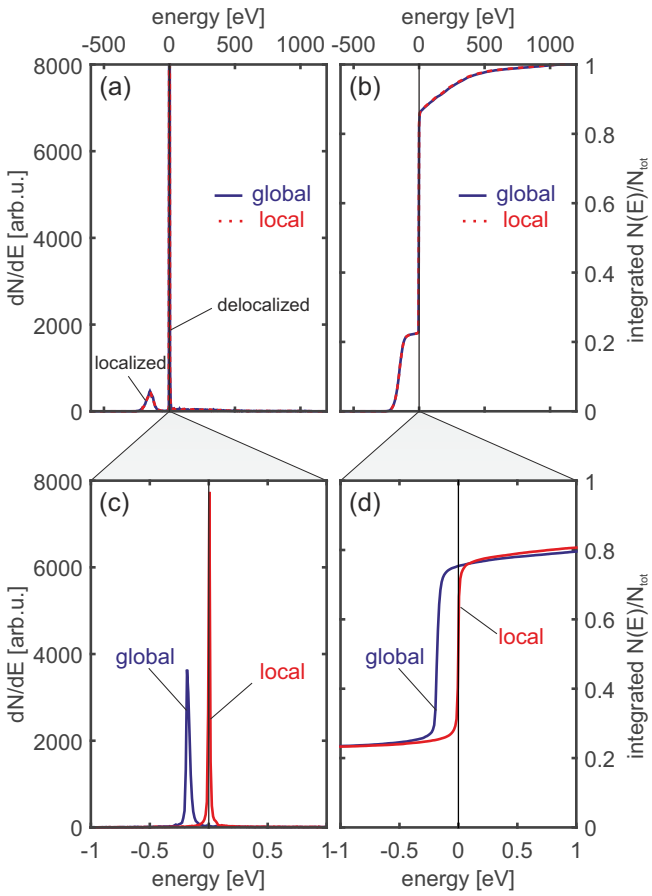

Figure 6.8: Single-particle-energy distributions (left) and the corresponding cumulatively integrated distributions (right) after a simulation time of 400 ps over the full energy range (a-b) and zoomed in to the continuum threshold region (c-d). The blue curves correspond to distributions with respect to the global continuum threshold and the red curves to the local quasicontinuum threshold. Parameters as in figure 6.4.

6.3. Effect of a DC-extraction fields for ion detection on the re-localization dynamics

To evaluate the effect of a DC-extraction field on the dynamics of the delocalized electrons, additional calculations have been performed with identical system and laser parameters but an additional DC-field switched on. Typically, such extraction fields are on the order of a few kV/cm in experiments, consequently a field strength of

2 kV/cm has been chosen for the calculations. A comparison of the time evolution of inner (black) and outer ionization with (magenta) and without (red) DC-field is shown in figure 6.9a. The inner ionization is not effected by the extraction field as it is very weak compared to the intrinsic fields in the cluster in the early phase. During the excitation and the first picoseconds after also no effect on the outer ionization is observed. However, this behavior changes dramatically after about 50 ps when the cluster potential gets shallow enough for the extraction field to promote part of the weakly bound delocalized electrons into the continuum. Eventually this leads to an average outer ionization of about 15 electrons per atom, which is 3 times higher than without DC field. A more detailed view on the effect of the extraction field is provided by the integrated single-particle-energy spectra presented in figure 6.9b. It shows that almost all delocalized electrons (electrons close to the continuum threshold) are shifted to positive energies by the extraction field while the relocalized electrons are not effected.

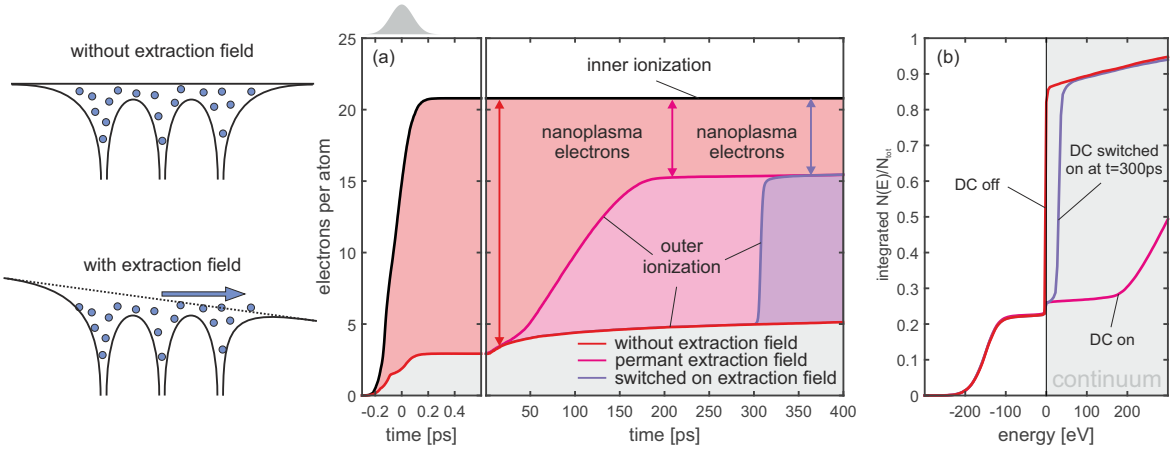

Figure 6.9.: Time evolution of average inner and outer ionization during and after the hard x-ray excitation with and without DC extraction field (2 kV/cm). The exact time evolution of the outer ionization depends on whether the extraction field is present permanently or switched on after the excitation (at $t = 300$ ps), however, the final outer ionization does not. The schematics in the left part of the figure illustrate the effect of an DC-extraction field, similar to barrier suppression ionization. Parameters as in figure 6.4.

As already mentioned above, the possible influence of the experimental extraction fields on the measured observables has been intensely debated in the cluster community during the last years. A first attempt to prove or disprove this idea included measurements where the extraction field has been switched on with a variable time delay with respect to the excitation [104]. In these experiments no significant influence of the time delay on the resulting charge state distributions could be observed. To also address these experiments, a third simulation run has been performed where the extraction field is switched on 300 ps after the excitation. The results are shown in figure 6.9a and b as purple lines and reveal that the switched on DC-field eventually yields the same final average outer ionization as the permanent extraction field (compare magenta and purple curves in figure 6.9a). The reason for this behavior can be understood from the time evolution of the distribution of delocalized electrons.

Since recombination is only efficient in early stages of the expansion, the number of delocalized electrons does not change significantly in the later stages, only its energetic position continuously shifts to lower binding energies. For a possible reionization of these electrons it is only important that the DC-field is still applied after sufficiently low binding energies have been reached and not when exactly it is switched on.

To evaluate the effect on the experimentally observable charge spectra, final charge state distributions have to be calculated from the simulations. To this end, every electron that is still bound to the cluster ($E_{sp} < 0$) at the end of the simulation (after 400 ps) is assigned to its closest ion and assumed to permanently recombine, reducing the effective charge state of the respective ion by one. The resulting final charge state distributions for all three calculation scenarios are shown in figure 6.10 together with the distribution of inner ionization charge states.

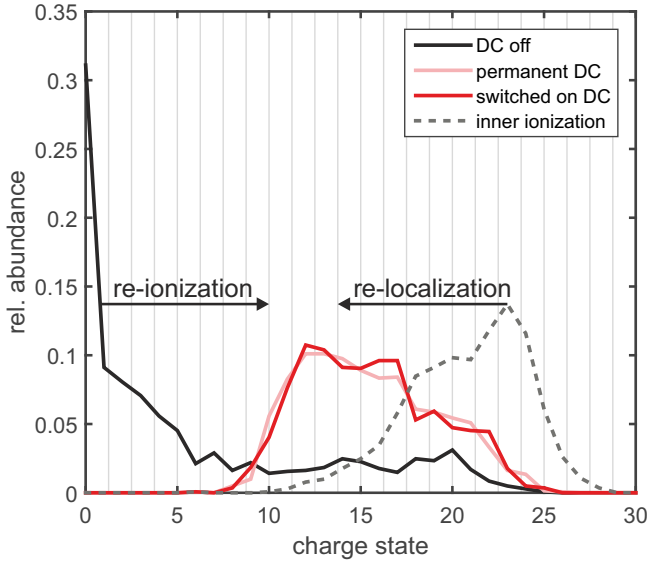

Figure 6.10.: Final ion charge spectra for the scenarios with DC extraction field switched off (black), permanently switched on (light red) and switched on 300 ps after the excitation (red). In the presence of an extraction field the charge state distribution is altered and shifted to higher charge states, no ion charges below Xe^{7+} can be observed. For comparison the inner charge state distribution is shown as grey dashed line. Parameters as in figure 6.4.

Comparing the results for calculations with (red and light red) and without extraction field (black) shows that the consideration of the detection field is essential to explain the observed extremely high average charge states and especially the absence of low charge states ($q \leq 5$) in the experiment. The relatively weak detector field can efficiently prevent the recombination of the extremely weakly bound Rydberg electrons, which would otherwise lead to significant signal at low charge states. Apparently, the exact timing for switching on the detection field has no significant influence on the final charge state distribution (c.f. red and light red curve in figure 6.10) and therefore does not provide a suitable tuning knob to analyze a possible manipulation of the system by the detection field.

However, just recently the influence of such extraction fields on the measured observables has been successfully demonstrated. Schütte *et.al* [105] followed an alternative

approach, where the main observable is not the charge state distribution but the transverse momentum (transverse with respect to the direction of the extraction field) of the expelled electrons. The basic idea is the following: If a large fraction of bound electrons occupies high-lying Rydberg-like states close to the continuum with binding energies of only a few meV (like it is observed in the calculations above), they should be easily reionized by the DC extraction field, and show up as a dominant contribution at low kinetic energies that heavily dominates the spectrum. In the experiments such a dominant contribution has been observed for the excitation of moderately sized Argon clusters ($N \approx 3500$) with intense XUV- and NIR-pulses. The fact that the slow electrons have been observed for clusters in two very different excitation regimes, but not for an atomic gas strongly supports the picture of a cluster expansion driven formation of Rydberg states.

Corresponding transverse electron energy spectra calculated from the simulations are displayed in figure 6.11 for all three scenarios. Panel (a) shows the low energy part of the spectrum up to 1 eV, with a dominating contribution of very slow electrons for the calculations with extraction field (red and light red curves) and a flat spectrum in the case without DC-field (black). In contrast to that, the spectra at larger energies shown in panel (b) are not affected by the extraction field. Both observations are in full agreement with the experimental observations and their interpretation by Schütte *et.al* [105].

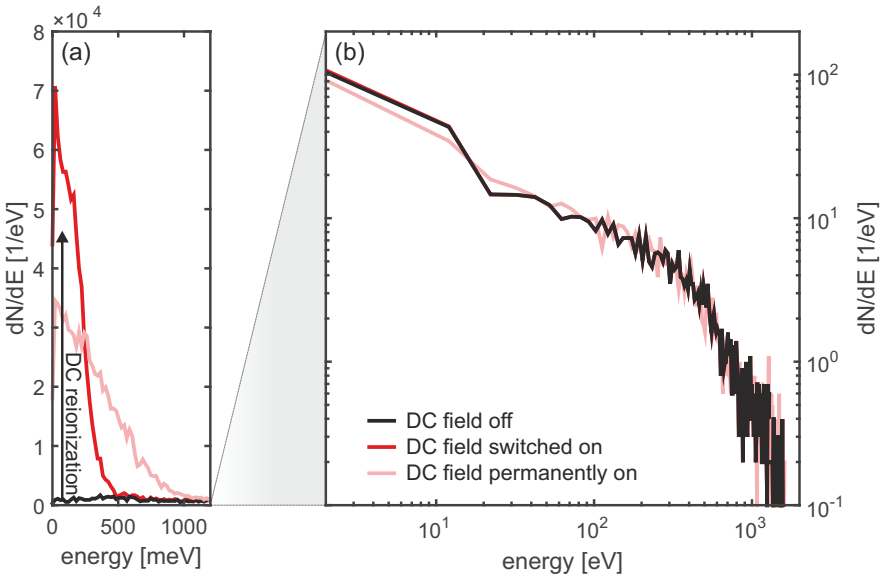

Figure 6.11.: Spectrum of the transverse kinetic electron energy with DC extraction field switched off (black), permanently switched on (light red) and switched on 300 ps after the excitation (red). Panel (a) shows the low energy part of the spectrum with a strongly enhanced contribution of slow electrons in the presence of an extraction field that dominates the spectrum. Panel (b) shows the high energy part of the electron spectrum with a cutoff near the photon energy of 1500 eV. Parameters as in figure 6.4.

6.4. X-ray intensity dependence of the final charge state distribution

Finally, to complete this theoretical study, the intensity dependence of the observed ionization dynamics is analyzed and discussed with reference to the experimental observations from Gorkhover *et.al* (see figure 6.2). To this end, additional sets of simulations have been performed for intensities higher ($5 \times 10^{16}\,\mathrm{W/cm^2}$) and lower ($2.5 \times 10^{15}\,\mathrm{W/cm^2}$) than the one discussed so far, including separate runs for the different extraction field setups. Figure 6.12 shows the results for all 3 considered intensities (as indicated) in terms of the time evolution of average inner and outer ionization (top panels) and final ion charge spectra (bottom panels).

Concentrating on the average ionization first, the inspection of figures 6.12a - 6.12c reveals that the extraction-field-driven reionization dynamics evolves qualitatively similar for all three intensities. The main quantitative differences are: (i) An increasing average final charge state for higher intensities that can be mainly attributed to the increasing number of plasma electrons generated during the x-ray pulse (inner ionization) and (ii) a larger contribution from autoionization due to the higher electron density for higher intensities. The fact that the average inner ionization does not scale linearly with the x-ray intensity, as one might expect for single photon ionization of atomic gas targets in the low intensity regime, can be mainly attributed to the beginning saturation of inner ionization due to the very high binding energies for charge states close to 30+. This is also indicated by the narrow distribution of inner ionization charge states in figure 6.12f.

The resulting final charge spectra displayed in the bottom panels of figure 6.12 show an intensity dependence that is consistent with the experimental observations when taking the extraction field into account. For both scenarios with extraction field (red and blue curves) recombination is efficiently frustrated such that final charge states with $q < 5$ can only be observed for the lowest considered intensity. In contrast to that, these low charge states dominate the spectrum when the extraction field is neglected (black curves). The missing singly charged ions in the calculated spectra with extraction field that dominate the focal averaged spectra in the experiment (see figure 6.2) are expected to arise from even lower x-ray intensities that are present in the outer regions of the laser focus.

In summary, the good qualitative and almost quantitative agreement of the presented calculations with the experimental observations strongly suggests that the experimental detection method itself significantly influenced the recorded charge state distributions. Furthermore, since the reionization mechanism does not depend qualitatively on the specific excitation conditions (such as wavelength or intensity), the effect of such extraction fields should be always considered when interpreting corresponding cluster experiments. However, the presented simulations have been performed for clusters much smaller than the ones used in the experiment. For large clusters the suppression of direct outer ionization is expected to be even stronger. Since a direct simulation of such large clusters is not feasible for the given time scales, the effect of the cluster size has to be studied by other means, e.g. by extrapolation of size-dependent

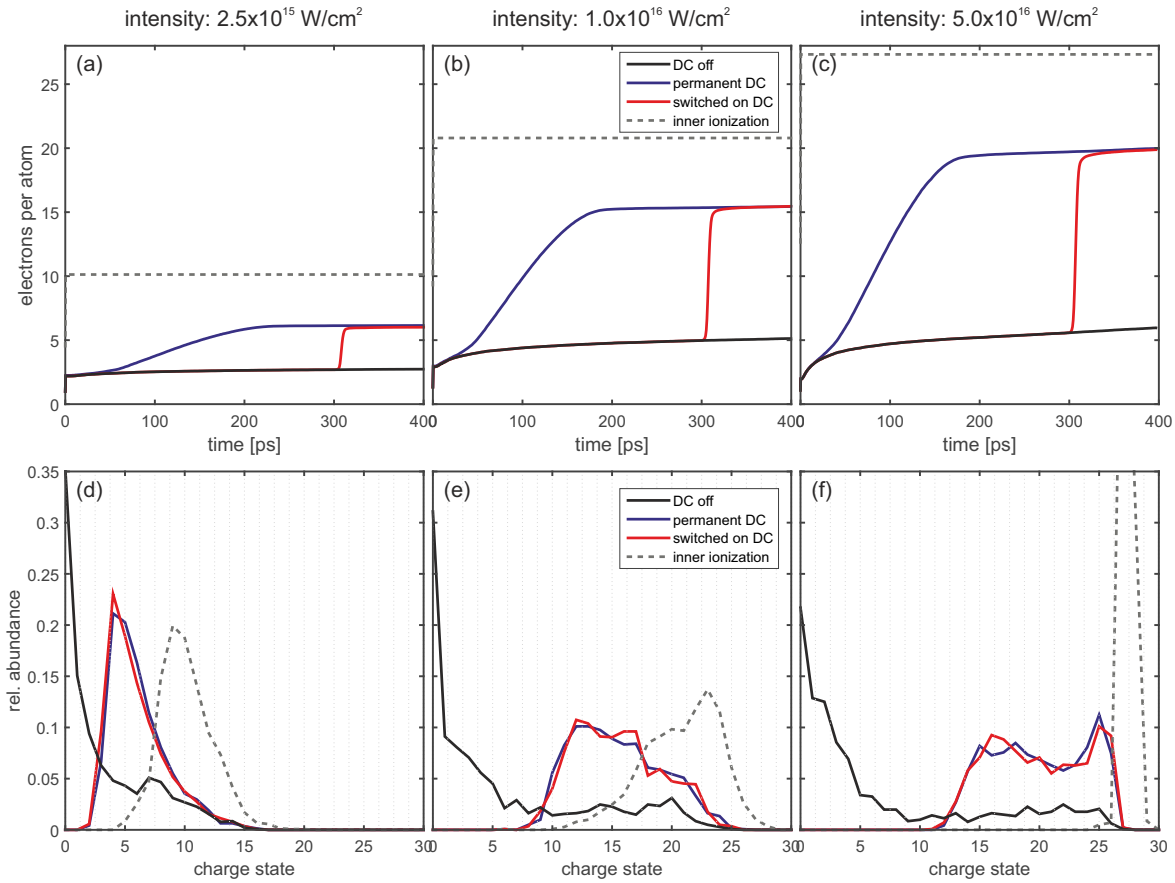

Figure 6.12.: Comparison of simulation runs for three different intensities (as indicated) for the scenarios with DC-extraction field switched off (black), permanently switched on (light red) and switched on 300 ps after the excitation (red). The top panels (a-c) show the time evolution of the corresponding inner and outer ionization. The bottom panels (d-f) show the resulting final ion charge state distribution. For comparison the inner charge state distributions are shown as grey dashed lines.

calculations in the regime of small to medium sized clusters.

7. Conclusions and outlook

Summary

The main goal of this work was the numerical implementation of the Microscopic Particle-In-Cell approach and its application to so far not accessible physical scenarios. The concept of MicPIC is based on a particle-particle/particle-mesh force decomposition that allows to reintroduce microscopic particle-particle interactions into a particle-in-cell treatment via local electrostatic MD. It has been shown that the representation of charged plasma particles with a gaussian shape function is key to a successful implementation as it ensures the required isotropic and low noise particle-particle forces on the PIC level. The resulting numerical code is able to simultaneously and self-consistently model the microscopic plasma dynamics and the evolution of the electromagnetic fields with high spatial resolution.

To validate the approach and its implementation, MicPIC calculations have been compared to results obtained from well established models. First, MicPIC's capability to describe the dynamics of strongly-coupled plasmas including ionization has been demonstrated using the example of NIR excitation of small Argon clusters ($R = 5\,\mathrm{nm}$), validating the correct treatment of atomic scale collisions. Subsequently, the description of field propagation in MicPIC has been tested. To this end, the linear absorption and scattering of pre-ionized spherical nanoplasmas exposed to few-cycle NIR laser fields has been studied as a function of cluster size. The comparison of the radius dependent absorption and scattering predicted by microscopic and continuum models validates MicPIC and reveals the breakdown of the electrostatic description for a system size of about $R \gtrsim 20\,\mathrm{nm}$ for 800 nm excitation wavelength. The material parameters resulting from this comparison are an important result in itself and revealed the competition of bulk and surface collisions with radiation damping as the origin of the maximum plasmon life time of resonant clusters for a characteristic size.

At higher laser intensities (nonlinear regime) the generation and evolution of electronic plasma waves has been studied for different initial cluster conditions, ranging from pre-ionized hydrogen and xenon clusters at resonant density[1] to initially neutral xenon clusters at solid density. In all scenarios the generation of strong plasma waves has been observed, leading to pronounced density and field fluctuations on the nanometer length and attosecond time scale. The calculations show that these fluctuations are most pronounced for resonant clusters, making them the ideal system for a first experimental demonstration of plasma waves in clusters. Though the fluctuations are much weaker for the solid density target, the plasma wave dynamics imprints characteristic features into the spatial charge state distribution with average inner ionization charge states differing by almost a factor of 2 throughout the cluster. The fact that the laser

[1] This refers to a density that corresponds to resonant plasmon excitation at 800 nm laser wavelength.

driven plasma waves significantly influence the ionization dynamics even when not driven resonantly suggests that they play an active role in most cluster experiments and have to be considered at their interpretation.

The next part of this work concentrated on a completely different excitation regime, i.e. the interaction of large clusters with soft x-ray radiation. Key to these investigations is MicPICs capability to simultaneously and self-consistently model the microscopic plasma dynamics and the evolution of the electromagnetic fields with high spatial resolution. As a first application in this regime, a numerical experiment has been performed where a large hydrogen cluster is excited by an intense NIR pulse and the induced expansion is imaged with intense x-ray pulses for different pulse delays. The calculations show an anisotropic self-similar expansion of the cluster after pump excitation that can be accurately described by a simple analytic few parameter density profile. The evolution of the main parameters (core-radius, decay length) could be linked to features in the recorded elastic scattering data with the help of a simple Born scattering model. This correspondence could be exploited to develop a retrieval method for dynamic x-ray imaging that will enable experiments at XFELs to make movies of laser induced expansion dynamics of finite nanoplasmas. In these first calculations bound electrons did not have to be considered since the NIR pump pulse fully ionizes the hydrogen droplet prior to the arrival of the x-ray imaging pulse. However, to enable MicPIC to also describe the interaction of initially neutral particles with x-ray radiation, the effect of bound electrons has to be taken into account. A first idea has been presented how bound electrons can be effectively described in terms of a classical dissipative oscillator model that can be tuned to reproduce the experimentally observed atomic absorption and scattering properties in the respective frequency region. Furthermore, it has been shown that the oscillator model provides a convenient way to implement the photoionization mechanism into MicPIC. In a first application of the extended MicPIC code, the inelastic contribution to the x-ray scattering has been studied for the excitation of initially neutral hydrogen clusters. In contrast to corresponding calculations for a pre-ionized hydrogen droplet, no pronounced plasmon satellites can be observed in the scattering spectra. Instead, the continuously changing electron density, which determines the spectral position of the inelastic scattering signal, results in a plateau-like structure in the spectrum.

The last part of this work is dedicated to the origin for the observation of highly charged atomic ions from clusters irradiated with intense laser pulses. Though such ions have been mainly observed for excitation wavelengths in the NIR regime, this study is mainly driven by recent experiments at the LCLS free-electron-laser in Stanford, where Gorkhover *et al.* [47] used intense hard x-ray pulses to excite single Xenon clusters. They observed average ion charge states higher than 20^+ while low charge states below 4^+ are absent. Such high average charge states can by no means explained with direct outer ionization on the time scale of the exciting x-ray pulse as direct ionization is quickly frustrated due to the generated space charge potential of the residual positively charged cluster. Based on an idea originally proposed in reference [24], this work studies the effect of an electric DC-extraction field, which is typically used in cluster experiments for charge state separation, on the evolution of the remaining bound electrons. The performed molecular dynamics calculations show that the

trapped plasma electrons quickly separate into two contributions, relocalized electrons that have been captured by individual ions through three-body-recombination and delocalized electrons that are still mobile in the decaying cluster. Due to the cluster expansion these delocalized electrons cool down to the bottom of the local quasi continuum. In early stages, when the average electron kinetic energy is much higher than the corresponding potential energy associated with electron-electron interactions, the electron system is weakly coupled and consequently the cooling behavior of an ideal gas is observed. In later stages of the expansion the strongly coupled regime is entered, where electron-electron interactions become important, resulting in a slower cooling that can be understood by considering the onset of strong coupling of electrons. At the same time the cluster potential becomes shallower during expansion and eventually the delocalized electrons are bound to the cluster with energies in the meV range. At this stage even small DC-fields are sufficient to remove these electrons from the cluster. The resulting calculated final ion charge spectra show the same characteristic features as the spectra measured in the experiment, which strongly suggests that the extraction field itself influences the measured data.

Critical discussion and Outlook

The numerical model developed in this work represents a first successful attempt to self-consistently model the interaction of large many particle systems with intense electromagnetic radiation microscopically. However, especially the treatment of partially or completely neutral systems needs to be improved. First steps in this direction have been already taken with the implementation of the oscillator model for bound electrons. An expansion of this idea to multi-electron atoms will be one of the next logical steps in the ongoing development. Another problem arises from the fact that within MicPIC only charged particles can interact. As a result the interaction of neutral atoms with ions or other neutral atoms is neglected completely in the current state of the model. Even the repulsion of two ions, mediated by the applied pseudo-potential of two Gaussian particles, is significantly underestimated for very small particle distances. Consequently, large angle binary collisions between ions can only occur for small relative ion velocities. One possibility to address this problem arises from the fact that in MicPIC binary interactions are already evaluated within a finite cut-off sphere. This allows the implementation of arbitrary binary short range potentials, e.g. Lennard-Jones type potentials for the interaction of neutral atoms. The most important challenge, however, is the inclusion of quantum effects. So far only limited quantum effects have been taken into account in terms of the utilized ionization rates. Other quantum effects regarding the scattering of particles, degeneracy effects (Pauli-blocking) or the coherent quantum dynamics of atoms (Rabi-flopping) are not included yet. Finding ways to take such processes into account effectively represents an exciting task for future work.

Appendix

A. Time dependence of expansion driven electron cooling in weakly and strongly coupled plasmas

In the following, the electron cooling behavior during the expansion of weakly and strongly coupled plasmas is briefly discussed. For that purpose, a spherical plasma is assumed where the ionic background expands homogeneously. The time evolution of the sphere radius is determined by a constant velocity of the outermost ions ($v_\mathrm{i} = const.$) according to

$$R(t) = R_0 + v_\mathrm{i} t. \tag{A.1}$$

During expansion, the offset R_0 becomes negligible and the sphere radius increases effectively linearly with $R(t) \propto t$. Furthermore, the analysis concentrates on the expansion phase after laser excitation, such that the expansion process is adiabatic.

A.1. Weakly coupled plasmas

In the regime of weak coupling, the interaction of charged particles is dominated by collective effects and microscopic interactions like binary collisions can be neglected. In a sense, the ion background forms an expanding spherical container that confines the electrons. As a result, the evolution of the expansion cooling of electrons can be approximated by that of an ideal gas. During the adiabatic expansion of an ideal gas, its temperature and volume are related as follows:

$$TV^{\gamma-1} = const. \tag{A.2}$$

Considering an ideal gas (of electrons) with no internal degrees of freedom ($\gamma = 5/3$) and an expansion by inertia ($R(t) \propto t$) immediately yields the following time-dependence of the temperature

$$T \propto t^{-2}. \tag{A.3}$$

A.2. Strongly coupled plasmas

In the regime of strong coupling, microscopic interactions (correlations) have to be taken into account. In order to find a relation similar to (A.3) under these conditions, the virial theorem can be utilized. It states that for a finite system[1] of interacting

[1] In this context this means that particle momenta and positions have to be finite.

particles the time average of the total kinetic energy $\bar{K}$ can be related to the time average of the total potential energy $\bar{U}$ in the following way:

$$\bar{K} = \frac{n}{2}\bar{U}. \tag{A.4}$$

This expression is valid for binary particle potentials of the form $V(r) = \alpha r^n$. For the Coulomb potential the potential parameter is $n = -1$, which yields

$$\bar{K} = -\frac{1}{2}\bar{U}. \tag{A.5}$$

Under the assumption that the system is ergodic, the average over time can be replaced by an average over an statistical ensemble (indicated here by brackets)

$$\langle K \rangle = -\frac{1}{2} \langle U \rangle . \tag{A.6}$$

Finally, the average kinetic and potential energies need to be connected to the temperature and plasma sphere radius, respectively. The average kinetic energy is related to the temperature via

$$\langle K \rangle = \frac{3}{2} K_\mathrm{B} T. \tag{A.7}$$

The average potential energy for particles interacting via Coulomb forces is determined by the average interparticle distance $\langle r \rangle$ according to

$$\langle U \rangle \propto \frac{e^2}{\langle r \rangle} \propto \frac{e^2}{n^{1/3}} \propto \frac{e^2}{R} \tag{A.8}$$

Inserting expression (A.7) and (A.8) into equation (A.6) yields

$$T \propto R^{-1}. \tag{A.9}$$

Again assuming an expansion by inertia ($R(t) \propto t$) yields the desired scaling relation

$$T \propto t^{-1}. \tag{A.10}$$

B. Interactionpotential for two gaussian charge distributions

B.1. Gaussian charge distribution

When describing a plasma particle by a Gaussian charge distribution $\rho(r) = \rho_0 e^{\frac{-r^2}{d^2}}$, the parameters ρ_0 and d defining its peak density and width have to be chosen to preserve the total particle charge Q_{tot}. The charge enclosed in a sphere around the center of the charge distribution is given by

$$Q(R) = \int \rho(r) \mathrm{d}^3\mathbf{r} = 4\pi \int_0^R r^2 \rho(r) \mathrm{d}r \ , \tag{B.1}$$

where R is the radius of the sphere. Utilizing the integral expressions

$$\int_0^r e^{-\tau^2} d\tau = \frac{\sqrt{\pi}}{2} \mathrm{erf}(r) \tag{B.2}$$

and

$$\int_0^r r' e^{-\frac{r'^2}{d^2}} \mathrm{d}r' = -\frac{d^2}{2} e^{-\frac{r^2}{d^2}} \tag{B.3}$$

and integrating equation (B.1) by parts

$$\begin{aligned} Q(R) &= 4\pi\rho_0 \left(-\frac{d^2}{2} r e^{-\frac{r^2}{d^2}} \Big|_0^R + \frac{d^2}{2} \int_0^R e^{-\frac{r^2}{d^2}} \right) && \text{(B.4)} \\ &= \pi d^3 \rho_0 \left(\pi^{\frac{1}{2}} \mathrm{erf}\left(\frac{R}{d}\right) - 2\left(\frac{R}{d}\right) e^{-\frac{R^2}{d^2}} \right) && \text{(B.5)} \end{aligned}$$

yields

$$Q(R) = Q_{\text{ges}} \left(\mathrm{erf}\left(\frac{R}{d}\right) - \frac{2}{\sqrt{\pi}} \left(\frac{R}{d}\right) e^{-\frac{R^2}{d^2}} \right) \ . \tag{B.6}$$

For $R \to \infty$ the total charge has to be contained in the sphere and the desired relation between total charge and distribution parameters ρ_0 and d can be established:

$$Q_{\text{ges}} = \pi^{\frac{3}{2}} \rho_0 d^3 \ . \tag{B.7}$$

The fact that the charge distribution parameters ρ_0 and d are connected through the total particle charge Q_{tot} implicates that one degree of freedom is left. In the following it will be demonstrated how this freedom can be utilized to tune the depth of the interaction potential of two Gaussian particles.

B.2. Interaction energy of Gaussian charge distribution and a point charge

In a first step the interaction potential between a point charge located at the origin of coordinates and a Gaussian charge distribution

$$\rho(\mathbf{r}) = \rho_0 \exp\left(-\frac{|\mathbf{r}-\mathbf{r}_0|^2}{d^2}\right) \tag{B.8}$$

centered at $\mathbf{r}_0 = (0,0,a)$ will be calculated. For that purpose the following integral has to be evaluated

$$V(a) = \frac{q_1}{4\pi\epsilon_0}\int_{-\infty}^{\infty}\int_{-\infty}^{\infty}\int_{-\infty}^{\infty}\rho_0 \exp\left(-\frac{x^2+y^2+(z-a)^2}{d^2}\right)\frac{1}{\sqrt{x^2+y^2+z^2}}\,\mathrm{d}x\,\mathrm{d}y\,\mathrm{d}z. \tag{B.9}$$

Changing to spherical coordinates

$$\begin{aligned} x &= r\,\sin\theta\,\cos\phi \\ y &= r\,\sin\theta\,\sin\phi \\ z &= r\,\cos\theta \\ \mathrm{d}x\,\mathrm{d}y\,\mathrm{d}z &= r^2\sin\theta\,\mathrm{d}r\,\mathrm{d}\phi\,\mathrm{d}\theta. \end{aligned}$$

allows to carry out the integral over ϕ, which leaves

$$V(a) = \frac{q_1\rho_0}{4\pi\epsilon_0}2\pi\int_0^{\infty}\int_0^{\pi}\exp\left(-\frac{r^2-2ar\cos\theta+a^2}{d^2}\right)r\sin\theta\,\mathrm{d}\theta\,\mathrm{d}r. \tag{B.10}$$

Substituting $k = \cos\theta$ with $\mathrm{d}k = -\sin\theta\,\mathrm{d}\theta$

$$V(a) = \frac{q_1\rho_0}{4\pi\epsilon_0}2\pi\int_0^{\infty}\exp\left(-\frac{r^2+a^2}{d^2}\right)r\int_{-1}^{1}\exp\left(\frac{2ark}{d^2}\right)\,\mathrm{d}k\,\mathrm{d}r \tag{B.11}$$

allows to also carry out the integral over k yielding

$$V(a) = \frac{q_1\rho_0}{4\pi\epsilon_0}2\pi\int_0^{\infty}\exp\left(-\frac{r^2+a^2}{d^2}\right)\frac{d^2}{2a}\left[\exp\left(\frac{2ar}{d^2}\right)-\exp\left(-\frac{2ar}{d^2}\right)\right]\mathrm{d}r\,. \tag{B.12}$$

This expression can be reduced to

$$V(a) = \frac{q_1\rho_0}{4\pi\epsilon_0}\frac{\pi d^2}{a}\left[\int_0^{\infty}\exp\left(-\frac{(r-a)^2}{d^2}\right)\mathrm{d}r - \int_0^{\infty}\exp\left(-\frac{(r+a)^2}{d^2}\right)\mathrm{d}r\right]. \tag{B.13}$$

Using the substitution $r' = r-2a$ with $\mathrm{d}r' = \mathrm{d}r$ the first can integral can be reshaped to

$$\begin{aligned} &\int_0^{\infty}\exp\left(-\frac{(r-a)^2}{d^2}\right)\mathrm{d}r = \int_{-2a}^{\infty}\exp\left(-\frac{(r'+a)^2}{d^2}\right)\mathrm{d}r' \\ &= \int_{-2a}^{0}\exp\left(-\frac{(r'+a)^2}{d^2}\right)\mathrm{d}r' + \int_0^{\infty}\exp\left(-\frac{(r'+a)^2}{d^2}\right)\mathrm{d}r'. \end{aligned} \tag{B.14}$$

Inserting that into equation (B.13) yields the following expression for the interaction potential

$$\begin{aligned} V(a) &= \frac{q_1\rho_0}{4\pi\epsilon_0}\frac{\pi d^2}{a}\int_{-2a}^{0}\exp\left(-\frac{(r'+a)^2}{d^2}\right)\mathrm{d}r' \\ &+ \frac{q_1\rho_0}{4\pi\epsilon_0}\frac{\pi d^2}{a}\left[\int_0^{\infty}\exp\left(-\frac{(r+a)^2}{d^2}\right)\mathrm{d}r - \int_0^{\infty}\exp\left(-\frac{(r+a)^2}{d^2}\right)\mathrm{d}r\right] , \end{aligned} \tag{B.15}$$

where the terms in square brackets cancel each other. Again substituting $r = r' + a$ and $\mathrm{d}r' = \mathrm{d}r$ yields:

$$\begin{aligned} V(a) &= \frac{q_1\rho_0}{4\pi\epsilon_0}\frac{\pi d^2}{a}\int_{-a}^{a}\exp\left(-\frac{(r)^2}{d^2}\right)\mathrm{d}r \\ &= \frac{q_1\rho_0}{4\pi\epsilon_0}\frac{\pi d^2}{a}\,2\int_0^{a}\exp\left(-\frac{(r)^2}{d^2}\right)\mathrm{d}r\,. \end{aligned} \tag{B.16}$$

Finally, substituting $s = \frac{r}{d}$ and $\mathrm{d}r = d\,\mathrm{d}s$ allows to express the interaction energy

$$V(a) = \frac{q_1\rho_0}{4\pi\epsilon_0}\frac{2\pi d^2}{a}\int_0^{a}\exp\left(-\frac{r^2}{d^2}\right)\mathrm{d}r = \frac{q_1\rho_0}{4\pi\epsilon_0}\frac{2\pi d^3}{a}\int_0^{a/d}\exp(-s^2)\mathrm{d}s \tag{B.17}$$

in terms of the error function $\mathrm{erf}(x) = \frac{2}{\sqrt{\pi}}\int_0^x \exp(-t^2)\mathrm{d}t$ and equation (B.7) can be reduced to

$$V(a) = \frac{q_1 q_2}{4\pi\epsilon_0 a}\mathrm{erf}\left(\frac{a}{d}\right). \tag{B.18}$$

The width parameter d scales the argument of the error function and determines the depth of the resulting potential.

B.3. Interaction energy of two Gaussian particles

The interaction energy of two Gaussian particles can be calculated analogous to section B.2:

$$V(|\mathbf{r}_1 - \mathbf{r}_2|) = \frac{\rho_{0,1}\rho_{0,2}}{4\pi\epsilon_0}\int\int d^3\mathbf{r}\,d^3\mathbf{r}'\exp\left(-\frac{|\mathbf{r}-\mathbf{r}_1|^2}{a^2}\right)\frac{1}{|\mathbf{r}-\mathbf{r}'|}\exp\left(-\frac{|\mathbf{r}'-\mathbf{r}_2|^2}{b^2}\right) . \tag{B.19}$$

Without loss of generality the above integral can be simplified by setting $\mathbf{r}_1 = 0$ and $\mathbf{z} = \mathbf{r} - \mathbf{r}'$:

$$V(|\mathbf{r}_1 - \mathbf{r}_2|) = \frac{\rho_{0,1}\rho_{0,2}}{4\pi\epsilon_0}\int\int d^3\mathbf{r}\,d^3\mathbf{z}\exp\left(-\frac{r^2}{a^2}\right)\frac{1}{|\mathbf{z}|}\exp\left(-\frac{(\mathbf{r}-\mathbf{z}-\mathbf{r}_2)^2}{b^2}\right) . \tag{B.20}$$

Since the integration over $\mathbf{r}'$ has to be carry out over infinity, it can also be carried out with respect to $\mathbf{z}$. Substituting $\mathbf{\Delta} = \mathbf{z} + \mathbf{r}_2$ yields:

$$V(|\mathbf{r}_1 - \mathbf{r}_2|) = \frac{\rho_{0,1}\rho_{0,2}}{4\pi\epsilon_0}\int\int d^3\mathbf{r}\,d^3\mathbf{z}\exp\left(-\underbrace{\left(\frac{r^2}{a^2}+\frac{(\mathbf{r}-\mathbf{\Delta})^2}{b^2}\right)}_{K}\right)\frac{1}{|\mathbf{z}|} \tag{B.21}$$

with

$$K = \frac{r^2}{a^2} + \frac{r^2}{b^2} - 2\frac{\mathbf{r}\cdot\mathbf{\Delta}}{b^2} + \frac{\Delta^2}{b^2} = \left(\frac{a^2+b^2}{a^2b^2}\right) r^2 - 2\frac{\mathbf{r}\cdot\mathbf{\Delta}}{b^2} + \frac{\Delta^2}{b^2} \; . \tag{B.22}$$

By completing the square the mixed term can be eliminated

$$K = \left(\frac{\sqrt{a^2+b^2}}{ab}\,\mathbf{r} - \frac{1}{b^2}\frac{ab}{\sqrt{a^2+b^2}}\mathbf{\Delta}\right)^2 - \frac{a^2}{a^2b^2+b^4}\Delta^2 + \frac{\Delta^2}{b^2} \tag{B.23}$$

and further substituting

$$K = \left(\underbrace{\frac{\sqrt{a^2+b^2}}{ab}\,\mathbf{r} - \frac{a}{\sqrt{a^2b^2+b^4}}\mathbf{\Delta}}_{\mathbf{t}}\right)^2 + \frac{\Delta^2}{a^2+b^2} \tag{B.24}$$

with

$$d^3\mathbf{t} = \frac{(a^2+b^2)^{3/2}}{a^3b^3}\, d^3\mathbf{r} \tag{B.25}$$

yields

$$V(|\mathbf{r}_1-\mathbf{r}_2|) = \frac{\rho_{0,1}\rho_{0,2}}{4\pi\epsilon_0}\frac{a^3b^3}{(a^2+b^2)^{3/2}}\int\int d^3\mathbf{t}\, d^3\mathbf{z}\exp\left(-t^2\right)\exp\left(-\frac{\Delta^2}{a^2+b^2}\right)\frac{1}{|\mathbf{z}|} \; . \tag{B.26}$$

The integral over $\mathrm{d}^3\mathbf{t}$ can be carried out now and yields $\int d^3\mathbf{t}\exp(-t^2) = \pi^{3/2}$, which leaves one more integration. Inserting $\mathbf{\Delta}$ again, yields

$$V(|\mathbf{r}_1-\mathbf{r}_2|) = \frac{\rho_{0,1}\rho_{0,2}}{4\pi\epsilon_0}\pi^{3/2}\frac{a^3b^3}{(a^2+b^2)^{3/2}}\int d^3\mathbf{z}\exp\left(-\frac{(\mathbf{z}+\mathbf{r}_2)^2}{a^2+b^2}\right)\frac{1}{|\mathbf{z}|}. \tag{B.27}$$

This integral is already known from section B.2 and yields:

$$\int d^3z\exp\left(-\frac{(\mathbf{z}+\mathbf{r}_2)^2}{a^2+b^2}\right)\frac{1}{|\mathbf{z}|} = \pi^{3/2}(a^2+b^2)^{3/2}\frac{1}{r_2}\mathrm{erf}\left(\frac{r_2}{\sqrt{a^2+b^2}}\right) \; . \tag{B.28}$$

The interaction energy is then given by:

$$V(|\mathbf{r}_1-\mathbf{r}_2|) = \frac{1}{4\pi\epsilon_0}\underbrace{\rho_{0,1}\pi^{3/2}a^3}_{q_1}\underbrace{\rho_{0,2}\pi^{3/2}b^3}_{q_2}\frac{1}{r_2}\mathrm{erf}\left(\frac{r_2}{\sqrt{a^2+b^2}}\right) \; . \tag{B.29}$$

With equation (B.7) and $\mathbf{r} = \mathbf{r}_2$ a similar result to section B.2 can be observed

$$V(r) = \frac{q_1q_2}{4\pi\epsilon_0}\frac{1}{r}\mathrm{erf}\left(\frac{r}{\sqrt{a^2+b^2}}\right) \; , \tag{B.30}$$

with an effective width parameter $d \Leftrightarrow \sqrt{a^2+b^2}$ as the main difference.

Bibliography

[1] J. Clerk Maxwell. A dynamical theory of the electromagnetic field. *Philosophical Transactions of the Royal Society of London*, 155:459–512, 1865.

[2] J. M. DAWSON. Particle simulation of plasmas. *Rev. Mod. Phys.*, 55(2):403–447, 1983.

[3] C. K. Birdsall and A. B. Langdon. *Plasma physics via computer simulation*. McGraw-Hill, New York, 1985.

[4] J. P. Verboncoeur. Particle simulation of plasmas: review and advances. *Plasma Phys. Controlled Fusion*, 47(5A, SI):A231–A260, MAY 2005. 12th International Congress on Plasma Physics (ICPP2004), Nice, FRANCE, OCT 25-29, 2004.

[5] T. Esirkepov, M. Borghesi, S. V. Bulanov, G. Mourou, and T. Tajima. Highly efficient relativistic-ion generation in the laser-piston regime. *Phys. Rev. Lett.*, 92(17), APR 30 2004.

[6] J. Faure, Y. Glinec, A. Pukhov, S. Kiselev, S. Gordienko, E. Lefebvre, J. P. Rousseau, F. Burgy, and V. Malka. A laser-plasma accelerator producing monoenergetic electron beams. *Nature*, 431(7008):541–544, SEP 30 2004.

[7] G. A. Mourou, T. Tajima, and S. V. Bulanov. Optics in the relativistic regime. *Rev. Mod. Phys.*, 78(2):309–371, APR-JUN 2006.

[8] T. Takizuka and H. Abe. Binary collision model for plasma simulation with a particle code. *J. Comput. Phys.*, 25(3):205–219, 1977.

[9] K. Nanbu. Theory of cumulative small-angle collisions in plasmas. *Phys. Rev. E*, 55(4):4642–4652, APR 1997.

[10] T. Nakamura, Y. Fukuda, and Y. Kishimoto. Ionization dynamics of cluster targets irradiated by x-ray free-electron-laser light. *Phys. Rev. A*, 80(5), NOV 2009.

[11] F. Peano, J. L. Martins, R. A. Fonseca, L. O. Silva, G. Coppa, F. Peinetti, and R. Mulas. Dynamics and control of the expansion of finite-size plasmas produced in ultraintense laser-matter interactions. *Phys. Plasmas*, 14(5), MAY 2007. 48th Annual Meeting of the Division of Plasma Physics of the APS, Philadelphia, PA, OCT 30-NOV 03, 2006.

[12] M. Eloy, R. Azambuja, J. T. Mendonca, and R. Bingham. Interaction of ultrashort high-intensity laser pulses with atomic clusters. *Phys. Plasmas*, 8(3):1084–1086, MAR 2001.

[13] Y. Fukuda, Y. Kishimoto, T. Masaki, and K. Yamakawa. Structure and dynamics of cluster plasmas created by ultrashort intense laser fields. *Phys. Rev. A*, 73(3), MAR 2006.

[14] L. Englert, M. Wollenhaupt, L. Haag, C. Sarpe-Tudoran, B. Rethfeld, and T. Baumert. Material processing of dielectrics with temporally asymmetric shaped femtosecond laser pulses on the nanometer scale. *Appl. Phys. A* , 92(4):749–753, 2008.

[15] R. R. Thomson, T. A. Birks, S. G. Leon-Saval, A. K. Kar, and J. Bland-Hawthorn. Ultrafast laser inscription of an integrated photonic lantern. *Opt. Express*, 19(6):5698–5705, MAR 14 2011.

[16] B.-B. Xu, Y.-L. Zhang, H. Xia, W.-F. Dong, H. Ding, and H.-B. Sun. Fabrication and multifunction integration of microfluidic chips by femtosecond laser direct writing. *Lab Chip*, 13(9):1677–1690, 2013.

[17] S. Kim, J. Jin, Y.-J. Kim, I.-Y. Park, Y. Kim, and S.-W. Kim. High-harmonic generation by resonant plasmon field enhancement. *Nature*, 453(7196):757–760, JUN 5 2008.

[18] I.-Y. Park, S. Kim, J. Choi, D.-H. Lee, Y.-J. Kim, M. F. Kling, M. I. Stockman, and S.-W. Kim. Plasmonic generation of ultrashort extreme-ultraviolet light pulses. *Nature Photon.*, 5(11):678–682, NOV 2011.

[19] M. I. Stockman, M. F. Kling, U. Kleineberg, and F. Krausz. Attosecond nanoplasmonic-field microscope. *Nature Photon.*, 1(9):539–544, SEP 2007.

[20] S. Zherebtsov, T. Fennel, J. Plenge, E. Antonsson, I. Znakovskaya, A. Wirth, O. Herrwerth, F. Suessmann, C. Peltz, I. Ahmad, S. A. Trushin, V. Pervak, S. Karsch, M. J. J. Vrakking, B. Langer, C. Graf, M. I. Stockman, F. Krausz, E. Ruehl, and M. F. Kling. Controlled near-field enhanced electron acceleration from dielectric nanospheres with intense few-cycle laser fields. *Nature Phys.*, 7(8):656–662, AUG 2011.

[21] M. Nantel, G. Ma, S. Gu, C. Y. Cote, J. Itatani, and D. Umstadter. Pressure ionization and line merging in strongly coupled plasmas produced by 100-fs laser pulses. *Phys. Rev. Lett.*, 80(20):4442–4445, MAY 18 1998.

[22] L. Ramunno, C. Jungreuthmayer, H. Reinholz, and T. Brabec. Probing attosecond kinetic physics in strongly coupled plasmas. *J. Phys. B*, 39(23):4923–4931, DEC 14 2006.

[23] C. Siedschlag and J. M. Rost. Electron release of rare-gas atomic clusters under an intense laser pulse. *Phys. Rev. Lett.*, 89(17), OCT 21 2002.

[24] T. Fennel, L. Ramunno, and T. Brabec. Highly charged ions from laser-cluster interactions: Local-field-enhanced impact ionization and frustrated electron-ion recombination. *PHYSICAL REVIEW LETTERS*, 99(23), DEC 7 2007.

[25] U. Saalmann, C. Siedschlag, and J. M. Rost. Mechanisms of cluster ionization in strong laser pulses. *J. Phys. B*, 39(4):R39, 2006.

[26] T. Fennel, K.-H. Meiwes-Broer, J. Tiggesbaeumker, P.-G. Reinhard, P. M. Dinh, and E. Suraud. Laser-driven nonlinear cluster dynamics. *Rev. Mod. Phys.*, 82(2):1793–1842, JUN 8 2010.

[27] E. Springate, S. A. Aseyev, S. Zamith, and M. J. J. Vrakking. Electron kinetic energy measurements from laser irradiation of clusters. *Phys. Rev. A*, 68(5), NOV 2003.

[28] V. Kumarappan, M. Krishnamurthy, and D. Mathur. Asymmetric emission of high-energy electrons in the two-dimensional hydrodynamic expansion of large xenon clusters irradiated by intense laser fields. *Phys. Rev. A*, 67(4), APR 2003.

[29] Y. Fukuda, K. Yamakawa, Y. Akahane, M. Aoyama, N. Inoue, H. Ueda, and Y. Kishimoto. Optimized energetic particle emissions from Xe clusters in intense laser fields. *Phys. Rev. A*, 67(6), JUN 2003.

[30] T. Fennel, T. Döppner, J. Passig, C. Schaal, J. Tiggesbaumer, and K.-H. Meiwes-Broer. Plasmon-enhanced electron acceleration in intense laser metal-cluster interactions. *Phys. Rev. Lett.*, 98(14), APR 6 2007.

[31] E. M. Snyder, S. A. Buzza, and A. W. Castleman. Intense field-matter interactions: Multiple ionization of clusters. *Phys. Rev. Lett.*, 77(16):3347–3350, OCT 14 1996.

[32] L. Koller, M. Schumacher, J. Kohn, S. Teuber, J. Tiggesbaumker, and K.-H. Meiwes-Broer. Plasmon-enhanced multi-ionization of small metal clusters in strong femtosecond laser fields. *Phys. Rev. Lett.*, 82(19):3783–3786, MAY 10 1999.

[33] S. Zamith, T. Martchenko, Y. Ni, S. A. Aseyev, H. G. Muller, and M. J. J. Vrakking. Control of the production of highly charged ions in femtosecond-laser cluster fragmentation. *Phys. Rev. A*, 70(1), JUL 2004.

[34] A. McPherson, B. D. Thompson, A. B. Borisov, K. Boyer, and C. K. Rhodes. Multiphoton-induced x-ray emission at 4-5 kev from xe atoms with multiple core vacancies. *Nature*, 370(6491):631, August 1994.

[35] T. Ditmire, T. Donnelly, R. W. Falcone, and M. D. Perry. Strong x-ray emission from high-temperature plasmas produced by intense irradiation of clusters. *Phys. Rev. Lett.*, 75(17):3122, October 1995.

[36] E. Parra, I. Alexeev, J. Fan, K. Y. Kim, S. J. McNaught, and H. M. Milchberg. X-ray and extreme ultraviolet emission induced by variable pulse-width irradiation of ar and kr clusters and droplets. *Phys. Rev. E*, 62(5):R5931, November 2000.

[37] C. Prigent, C. Deiss, E. Lamour, J.-P. Rozet, D. Vernhet, and J. Burgdörfer. Effect of pulse duration on the x-ray emission from ar clusters in intense laser fields. *Phys. Rev. A*, 78(5):053201, November 2008.

[38] J. Zweiback, T. Ditmire, and M. D. Perry. Femtosecond time-resolved studies of the dynamics of noble-gas cluster explosions. *Phys. Rev. A*, 59(5):R3166–R3169, MAY 1999.

[39] T. Döppner, S. Teuber, M. Schumacher, J. Tiggesbaumker, and K.-H. Meiwes-Broer. Charging dynamics of metal clusters in intense laser fields. *Appl. Phys. B*, 71(3):357–360, SEP 2000.

[40] T. Döppner, T. Fennel, P. Radcliffe, J. Tiggesbaumker, and K.-H. Meiwes-Broer. Ion and electron emission from silver nanoparticles in intense laser fields. *Phys. Rev. A*, 73(3), MAR 2006.

[41] K. Tiedtke, A. Azima, N. von Bargen, L. Bittner, S. Bonfigt, S. Duesterer, B. Faatz, U. Fruehling, M. Gensch, C. Gerth *et al.* The soft x-ray free-electron laser FLASH at DESY: beamlines, diagnostics and end-stations. *New. J. Phys.*, 11:023029, 2009.

[42] P. Emma, R. Akre, J. Arthur, R. Bionta, C. Bostedt, J. Bozek, A. Brachmann, P. Bucksbaum, R. Coffee, F. -J. Decker *et al.* First lasing and operation of an angstrom-wavelength free-electron laser. *Nat. Photon.*, 4:641–647, 2010.

[43] N. D. Loh, C. Y. Hampton, A. V. Martin, D. Starodub, R. G. Sierra, A. Barty, A. Aquila, J. Schulz, L. Lomb, J. Steinbrener *et al.* Fractal morphology, imaging and mass spectrometry of single aerosol particles in flight. *Nature*, 486(7404):513, 2012.

[44] H. N. Chapman, P. Fromme, A. Barty, T. A. White, R. A. Kirian, A. Aquila, M. S. Hunter, J. Schulz, D. P. DePonte, U. Weierstall *et al.* Femtosecond X-ray protein nanocrystallography. *Nature*, 470(7332):73, 2011.

[45] R. Neutze, R. Wouts, D. van der Spoel, E. Weckert, and J. Hajdu. Potential for biomolecular imaging with femtosecond x-ray pulses. *Nature*, 406(6797):752, 2000.

[46] I. Barke, H. Hartmann, D. Rupp, L. Flueckiger, M. Sauppe, M. Adolph, S. Schorb, C. Bostedt, R. Treusch, C. Peltz, S. Bartling, T. Fennel, K.-H. Meiwes-Broer, and T. Moeller. The 3D-architecture of individual free silver nanoparticles captured by X-ray scattering. *Nat. Commun.*, 6, FEB 2015.

[47] T. Gorkhover, M. Adolph, D. Rupp, S. Schorb, S. W. Epp, B. Erk, L. Foucar, R. Hartmann, N. Kimmel, K.-U. Kuehnel *et al.* Nanoplasma Dynamics of Single Large Xenon Clusters Irradiated with Superintense X-Ray Pulses from the Linac Coherent Light Source Free-Electron Laser. *Phys. Rev. Lett.*, 108:245005 , 2012.

[48] D. Rupp, M. Adolph, T. Gorkhover, S. Schorb, D. Wolter, R. Hartmann, N. Kimmel, C. Reich, T. Feigl, A. R. B. de Castro *et al.* Identification of twinned gas phase clusters by single-shot scattering with intense soft x-ray pulses. *New. J. Phys.*, 14:055016, 2012.

[49] C. Bostedt, E. Eremina, D. Rupp, M. Adolph, H. Thomas, M. Hoener, A. R. B. de Castro, J. Tiggesbaeumker, K.-H. Meiwes-Broer, T. Laarmann *et al.* Ultrafast X-Ray Scattering of Xenon Nanoparticles: Imaging Transient States of Matter. *Phys. Rev. Lett.*, 108(9):093401, 2012.

[50] S. H. Glenzer, O. L. Landen, P. Neumayer, R. W. Lee, K. Widmann, S. W. Pollaine, R. J. Wallace, G. Gregori, A. Hoell, T. Bornath *et al.* Observations of Plasmons in Warm Dense Matter. *Phys. Rev. Lett.*, 98:065002, 2007.

[51] S. H. Glenzer and R. Redmer. X-ray thomson scattering in high energy density plasmas. *Rev. Mod. Phys.*, 81:1625, 2009.

[52] A. Pukhov and J. Meyerter Vehn. Relativistic magnetic self-channeling of light in near-critical plasma: Three-dimensional particle-in-cell simulation. *Phys. Rev. Lett.*, 76(21):3975–3978, MAY 20 1996.

[53] T. V. Liseykina, S. Pirner, and D. Bauer. Relativistic Attosecond Electron Bunches from Laser-Illuminated Droplets. *Phys. Rev. Lett.*, 104:095002, 2010.

[54] A. Pukhov. Strong field interaction of laser radiation. *Rep. Prog. Phys.*, 66(1):47–101, JAN 2003.

[55] K. S. Yee. Numerical solution of initial boundary value problems involving Maxwell's equations in isotropic media. *IEEE Trans. Antennas Propagat.*, 14:302, 1966.

[56] R. Holland and J. W. Williams. Total-field versus scattered-field finite-difference codes - a comparative-assessment. *IEEE Trans. Nucl. Sci.*, 30(6):4583–4588, 1983.

[57] J. Berenger. A perfectly matched layer for the absorption of electromagnetic waves. *J. Comput. Phys.*, 114:185, 1994.

[58] S. D. Gedney. An anisotropic perfectly matched layer absorbing media for the truncation of FDTD latices. *IEEE Trans. Antennas. Propag.*, 44:1630, 1996.

[59] S. D. Gedney. An anisotropic PML absorbing media for the FDTD simulation of fields in lossy and dispersive media. *ELECTROMAGNETICS*, 16(4):399–415, JUL-AUG 1996.

[60] A. Taflove and S. C. Hagness. *Computational Electrodynamics: The Finite-Difference Time-Domain Method*. Artech House, 2005.

[61] J. W. Eastwood and R. W. Hockney. Shaping force law in 2-dimensional particle-mesh models. *J. Comp. Physiol*, 16(4):342–359, 1974.

[62] C. Varin, C. Peltz, T. Brabec, and T. Fennel. Attosecond Plasma Wave Dynamics in Laser-Driven Cluster Nanoplasmas. *Phys. Rev. Lett.*, 108:175007, 2012.

[63] M. P. Allen and Tildesley D. J. *Computer Simulation of Liquids*. Oxford Universtity Press, New York, 1989.

[64] J. P. Boris and R. A. Shanny, editors. *Relativistic plasma simulations Optimization of a hybrid code*, Proceedings of the conference on the numerical simulation of plasmas (4th), 1970.

[65] T. Tajima. *Computational Plasma Physics*. Westview Press, 2004.

[66] M. V. Ammosov, N. B. Delone, and V. P. Krainov. Tunnel ionization of complex atoms and of atomic ions in an alternating electromagnetic field. *Soviet Physics - JETP*, 64:1191–4, Dec. 1986.

[67] A. L. Ankudinov, S. I. Zabinsky, and J. J. Rehr. Single configuration Dirac-Fock atom code. *Comput. Phys. Commun.*, 98(3):359–364, NOV 1996.

[68] W. Lotz. An empirical formula for electron-impact ionization cross-section. *Zeitschrift für Physik*, 206(2):205–211, 1967.

[69] C. Achenbach, A. Müller, E. Salzborn, and R. Becker. Single Ionization of multiply charged Xenon Ions by Electron-Impact. *J. Phys. B*, 17(7):1405–1425, 1984.

[70] D. C. Griffin, C. Bottcher, M. S. Pindzola, S. M. Younger, D. C. Gregory, and D. H. Crandall. Electron-Impact Ionization in the Xenon Isonuclear Sequence. *Phys. Rev. A*, 29(4):1729–1741, 1984.

[71] D. C. Gregory and D. H. Crandall. Measurement of the Cross-Section for Electron-Impact Ionization of Xe-6+ Ions. *Phys. Rev. A*, 27(5):2338–2341, 1983.

[72] M. E. Bannister, D. W. Mueller, L. J. Wang, M. S. Pindzola, D. C. Griffin, and D. C. Gregory. Cross-Sections for Electron-Impact Single Ionization of Kr-8+ and Xe-8+. *Phys. Rev. A*, 38(1):38–43, 1988.

[73] A. Heidenreich, I. Last, and J. Jortner. Electron impact ionization of atomic clusters in ultraintense laser fields. *Eur. Phys. J. D*, 35:567–577, 2005.

[74] W. Lotz. Electron-impact ionization cross-sections and ionization rate coefficients for atoms and ions from hydrogen to calcium. *Zeitschrift für Physik*, 216(3):241–247, 1968.

[75] C. Peltz, C. Varin, T. Brabec, and T. Fennel. Fully microscopic analysis of laser-driven finite plasmas using the example of clusters. *New. J. Phys.*, 14:065011, 2012.

[76] U. Kreibig and M. Vollmer. *Optical Properties of Metal Clusters*. Springer, Berlin, 1995.

[77] G. Mie. Beiträge zur Optik trüber Medien, speziell kolloidaler Metallösungen. *Ann. Phys.*, 330(3):377–445, 1908.

[78] J. A. Stratton. *Electromagnetic Theory*. Wiley-IEEE Press, 2007.

[79] C. Bohren and D. Huffman. *Absorption and scattering of light by small particles*. WILEY-VCH Verlag GmbH & Co. KGaA, Weinheim, 2007.

[80] T. Ditmire, T. Donnelly, A. M. Rubenchik, R. W. Falcone, and M. D. Perry. Interaction of intense laser pulses with atomic clusters. *Phys. Rev. A*, 53(5):3379, May 1996.

[81] J. Larmor. *On a dynamical theory of the electric and luminiferous medium*. Royal Society of London, London, 1897.

[82] L. Brillouin. The scattering cross section of spheres for electromagnetic waves. *J. Appl. Phys.*, 20(11):1110–1125, 1949.

[83] C. Sonnichsen, T Franzl, T. Wilk, G. von Plessen, and J. Feldmann. Plasmon resonances in large noble-metal clusters. *New J. Phys.*, 93, 2002.

[84] C. Soennichsen. *Plasmons in metal nanostructures*. Ph.D. thesis: Ludwig-Maximilians-Universität München, 2001.

[85] H. Baida, P. Billaud, S. Marhaba, D. Christofilos, E. Cottancin, A. Crut, J. Lermé, P. Maioli, M. Pellarin, M. Broyer, N. Del Fatti, F. Vallée, A. Sánchez-Iglesias, I. Pastoriza-Santos, and L. M. Liz-Marzá. Quantitative determination of the size dependence of surface plasmon resonance damping in single ag@ sio2 nanoparticles. *Nano Lett.*, 9, 2009.

[86] C. Peltz, C. Varin, T. Brabec, and T. Fennel. Time-Resolved X-Ray Imaging of Anisotropic Nanoplasma Expansion. *Phys. Rev. Lett.*, 113(13), SEP 23 2014.

[87] V. Kumarappan, M. Krishnamurthy, and D. Mathur. Two-dimensional effects in the hydrodynamic expansion of xenon clusters under intense laser irradiation. *Phys. Rev. A*, 66(3):033203, September 2002.

[88] T. Fennel, G.F. Bertsch, and K.-H. Meiwes-Broer. Ionization dynamics of simple metal clusters in intense fields by the thomas-fermi-vlasov method. *Eur. Phys. J. D*, 29(3):367, 2004.

[89] B. N. Breizman, A. V. Arefiev, and M. V. Fomyts'kyi. Nonlinear physics of laser-irradiated microclusters. *Phys. Plasmas*, 12(5):056706, May 2005.

[90] P. Mora. Plasma expansion into a vacuum. *Phys. Rev. Lett.*, 90(18):185002, 2003.

[91] A. V. Gurevich, L. V. Pariiska, and L. P. Pitaevskii. Self-similar motion of rarefied plasma. *Sov. Phys. JETP*, 22(2):449, 1966.

[92] D. Attwood. *Soft X-rays and Extreme Ultraviolet Radiation: Principles and Applications*. Cambridge University Press, 1999.

[93] J. J. Thomson. *Conduction of Electricity Through Gases*. Cambridge University Press, 1906.

[94] B. L. Henke, E. M. Gullikson, and J. C. Davis. X-ray interactions: photoabsorption, scattering, transmission, and reflection at E=50-30000 eV, Z=1-92. *At. Data. Nucl. Data Tables* , 54:181–342, 1993.

[95] M. Arbeiter and T. Fennel. Ionization heating in rare-gas clusters under intense XUV laser pulses. *Phys. Rev. A*, 82(1), JUL 30 2010.

[96] C. Bostedt, H. Thomas, M. Hoener, E. Eremina, T. Fennel, K.-H. Meiwes-Broer, H. Wabnitz, M. Kuhlmann, E. Ploenjes, K. Tiedtke, R. Treusch, J. Feldhaus, A. R. B. de Castro, and T. Moeller. Multistep ionization of argon clusters in intense femtosecond extreme ultraviolet pulses. *Phys. Rev. Lett.*, 100(13), APR 4 2008.

[97] C. Jungreuthmayer, L. Ramunno, J. Zanghellini, and T. Brabec. Intense VUV laser cluster interaction in the strong coupling regime. *J. Phys. B*, 38(16):3029–3036, AUG 28 2005.

[98] J. Passig, R. Irsig, N. X. Truong, Th Fennel, J. Tiggesbaeumker, and K.-H. Meiwes-Broer. Nanoplasmonic electron acceleration in silver clusters studied by angular-resolved electron spectroscopy. *New J. Phys.*, 14, AUG 22 2012.

[99] M. Arbeiter and T. Fennel. Rare-gas clusters in intense VUV, XUV and soft x-ray pulses: signatures of the transition from nanoplasma-driven cluster expansion to Coulomb explosion in ion and electron spectra. *New J. Phys.*, 13, MAY 13 2011.

[100] C. Peltz and T. Fennel. Resonant charging of Xe clusters in helium nanodroplets under intense laser fields. *EPJ D*, 63(2):281–288, JUL 2011.

[101] D. A. Verner, D. G. Yakovlev, I. M. Band, and M. B. Trzhaskovskaya. Subshell photoionization cross-sections and ionization energies of atoms and ions from he to zn. *At. Data. Nucl. Data Tables*, 55(2):233–280, NOV 1993.

[102] W. J. Veigele. Photon cross sections from 0.1 KeV to 1 MeV for elements Z=1 to Z=94. *At. Data. Nucl. Data Tables*, 5:51–111, 1973 1973.

[103] Yu. V. Dumin. Characteristic Features of Temperature Evolution in Ultracold Plasmas. *Plasma Phys. Rep.*, 37(10):858–865, OCT 2011.

[104] T. Möller. *(private communication).*

[105] B. Schuette, M. Arbeiter, T. Fennel, M. J. J. Vrakking, and A. Rouzee. Rare-Gas Clusters in Intense Extreme-Ultraviolet Pulses from a High-Order Harmonic Source. *Phys. Rev. Lett.*, 112(7), FEB 20 2014.

Erklärung

gemäß §4 der Promotionsordnung
der Mathematisch-Naturwissenschaftlichen Fakultät
der Universität Rostock

Ich gebe folgende Erklärung ab:

1. Die Gelegenheit zum vorliegenden Promotionsvorhaben ist mir nicht kommerziell vermittelt worden. Insbesondere habe ich keine Organisation eingeschaltet, die gegen Entgelt Betreuerinnen/Betreuer für die Anfertigung von Dissertationen sucht oder die mir obliegenden Pflichten hinsichtlich der Prüfungsleistungen für mich ganz oder teilweise erledigt.

2. Ich versichere hiermit an Eides statt, dass ich die vorliegende Arbeit selbstständig angefertigt und ohne fremde Hilfe verfasst habe. Dazu habe ich keine außer den von mir angegebenen Hilfsmitteln und Quellen verwendet und die den benutzten Werken inhaltlich und wörtlich entnommenen Stellen habe ich als solche kenntlich gemacht.

Rostock, den 24.04.2015

Christian Peltz